Strong Field Control of Multilevel Quantum Systems

A Dissertation Presented

by

Stephen Daniel Clow

to

The Graduate School

in Partial Fulfillment of the Requirements

for the Degree of

Doctor of Philosophy

in

Physics

Stony Brook University

August 2010

Stony Brook University

The Graduate School

Stephen Daniel Clow

We, the dissertation committee for the above candidate for the Doctor of Philosophy degree, hereby recommend acceptance of this dissertation.

Thomas Weinacht – Dissertation Advisor
Associate Professor, Department of Physics and Astronomy

Peter Stephens – Chairperson of Defense
Professor, Department of Physics and Astronomy

Thomas Bergemann
Research Professor, Department of Physics and Astronomy

Valery Milner
Assistant Professor
Department of Physics and Astronomy, University of British Columbia

This dissertation is accepted by the Graduate School.

Lawrence Martin
Dean of the Graduate School

Abstract of the Dissertation

Strong Field Control of Multilevel Quantum Systems

by

Stephen Daniel Clow

Doctor of Philosophy

in

Physics

Stony Brook University

2010

Thomas Weinacht

In this thesis, we present work on coherent control of multilevel quantum systems in the strong field limit using shaped ultrafast laser pulses. In recent years there have been numerous multiphoton absorption experiments in two,three, and four level atomics/molecular systems and many are performed in the limit of weak fields where perturbation theory is valid. Here, we describe a series of experiments aimed at exploring and understanding multiphoton transitions when the exciting field is strong and perturbation theory breaks down. Our approach to strong field control utilizes both parameterized scans of various pulse shapes and closed-loop learning control to identify a pulse shape that is optimal for populating a target quantum state. With this we will highlight the difference between sequential population transfer and adiabatic rapid passage in multilevel systems with multiphoton coupling between levels. Additionally, we examine strong field control of a four-level

atomic interferometer and show how interference in a target state changes from resonant pathways in the frequency domain to time-domain interference via a singe path.

Further, we use shaped femtosecond pulses to demonstrate a phenomenon in which a three-level atom becomes a modulator of an ultrafast pulse. The results are based on a pump-probe scheme that is very similar to Electromagnetically Induced Transparency (EIT). Important dynamics associated with a time-dependent coupling field are examined. Lastly, we extend previous work on two-photon driven superfluorescence from a shaped ultrafast drive laser and show how stimulated emission near threshold can turn modest coherent control yields into essentially perfect discrimination between systems where a control factor of about 10^4 is achieved between atomic and molecular species.

To my family

Contents

List of Figures

List of Tables

Acknowledgements

Still have to write .....

Jim, Kevin, Jet, Jason, Katy, Eli

Group: Brett, Carlos, Sarah, Coco, Dominik, Marija, Uvo, Peter,

AMO Dept: Hal and Linda

Office: Pat, Marija

I would like to thank Niels Damrauer for providing the molecular samples, the absorption and emission spectra, and helpful discussions.

Chapter 1

Introduction

A long standing goal of atomic, molecular, and optical physics has been to use coherent light for manipulating quantum systems. Because quantum phenomena are governed by a wavefunction that is subject to constructive and destructive interference, one needs to use the coherence property of the light to steer the system from an initial quantum state to a desired final state. The ability to modify spectral components of a coherent light field therefore yields rich possibilities for driving and controlling multiphoton absorption via interference of 'pathways' in quantum phase space. Here, a pathway represents a way for a system (Fig. 1.1) to get from an initial state $|g\rangle$ to to a final state $|e\rangle$ by groups of photons whose frequencies sum to equal the energy difference between $|g\rangle$ and $|e\rangle$, divided by $\hbar$. This is the essence of quantum coherent control - changing the relative phase and amplitude of frequency components driving an excitation to constructively or destructively interfere in a target quantum state.

The advent of broadband coherent light in the 1980s opened up a new paradigm in the coherent control of matter. Broadband lasers offered many frequency components at once, as well as high peak intensities, and became an attractive tool for driving nonlinear light-matter interaction. With the introduction of Titanium:Sapphire as a solid-state gain medium, ultrafast laser technology advanced rapidly and by the 1990s researchers had access to pulses on the order of several 10^{-15}s (femtosecond) [1, 2]. In parallel, the introduction of Chirped Pulse Amplification (CPA) [3] allowed for field strengths characteristic of the atomic unit of field (5.14×10^{11}V/m) to be readily achieved in the lab and eventually in commercially available systems. Femtosecond laser systems are now widely used in research laboratories around the world. Because multiple frequencies in a femtosecond pulse can contribute to a system's excitation, it became desirable to control the amplitude and phase of each frequency in an effort to control the excitation. In the early 1990s, researchers

developed technology to modify the spectral amplitude and phase of an ultrafast pulse (and therefore its temporal shape) [4, 5] and quickly researchers were able to produce pulses with arbitrary shape. Shaped ultrafast pulses have been used to probe and manipulate matter in thousands of experiments since the field of quantum coherent control began [6–9] and even shorter pulse durations 10^{-18}s (attosecond) have been achieved from the extreme ultraviolet (XUV) to X-ray region of the electromagnetic spectrum [10].

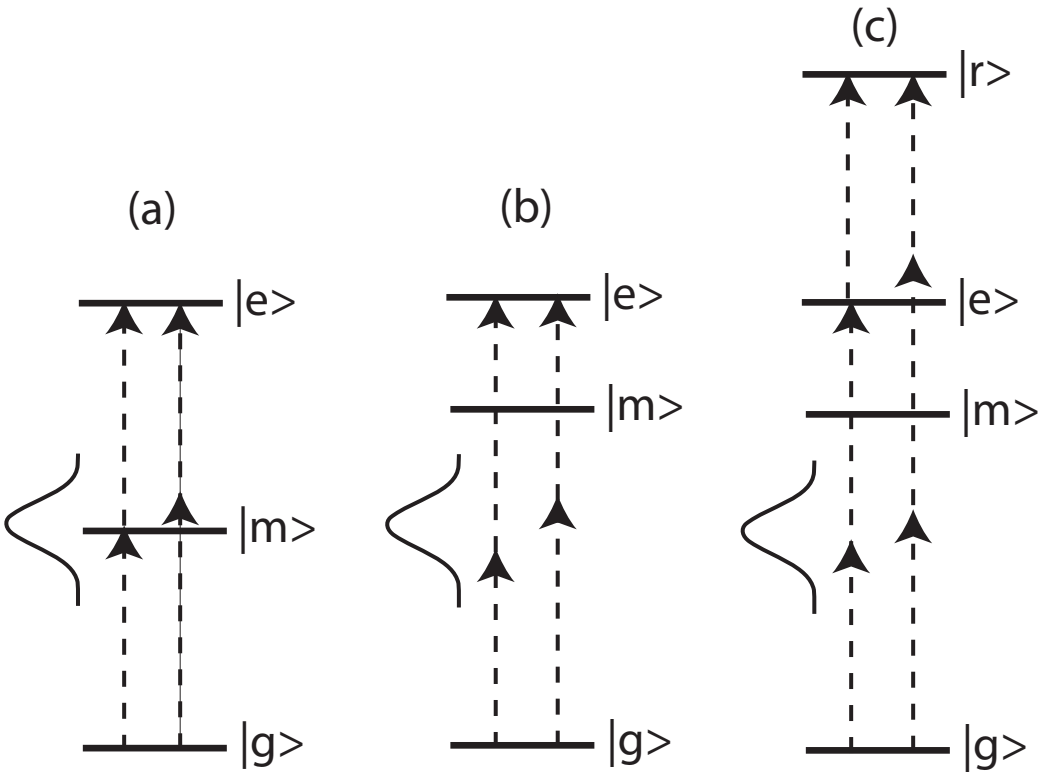

Figure 1.1: Two-photon and three-photon absorption. The laser bandwidth is illustrated at the left showing that multiple frequency pairs can add in a multiphoton transition . a) Two-photon absorption between a ground state $|g\rangle$ and excited state $|e\rangle$ through a resonant intermediate state $|m\rangle$. b) The same as (a), where the intermediate state $|m\rangle$ is far from resonance. c) (2+1) Three-photon absorption where there is a two-photon absorption through an off-resonant intermediate state followed by a single photon absorption.

In recent years there have been numerous efforts by researchers to control two, three, and four-level systems with shaped pulses in the weak field limit where a perturbation description of multiphoton absorption is valid. One of the early multiphoton experiments [11] used phase shaped laser pulses to coherently control the absorption of two photons in atomic Cesium. In this

case, the electronic structure is such that the intermediate state is far outside the laser bandwidth (i.e., far from resonance) shown in Fig. 1.1(b). Using a pulse shaper to shape the spectral phase of the laser, Meshulah and Silberberg were able to turn on and off the two-photon absorption (TPA) by the atom. Further, it was shown in the weak-field limit (when perturbation theory is valid) that any antisymmetric spectral phase about the two-photon resonance frequency maximized the TPA. Later, it was established by Dudovich et al. [12] that the presence of a near-resonant intermediate state (see Figure 1.1(a) required shaping of the drive pulse in order to maximize the two-photon absorption. Furthermore, experiments proceeded with shaped pulses and atoms in which more than two photons are absorbed. In particular, researchers began to consider atoms in which there is a non-resonant two-photon absorption, followed by a resonant single photon absorption - a so called 2+1 transition (Fig. 1.1(c)). Work by Amitay el al. [13] showed that shaping could enhance three-photon absorption in the weak field limit. And more recently, Ye et al. [14] considered the case of two resonant intermediate states in a four-level atom driven by shaped pulses in the weak field limit. Spanning well over a decade, these experiments make up an important part of the foundation for both non-resonant and near-resonant multiphoton absorption by ultrafast laser pulses where the atom-field interaction is appropriately described by perturbation theory. However, when the exciting fields become strong, perturbation theory breaks down and therefore the atom-field interaction must be formally described by other means.

Many techniques have been developed which make use of strong-field coupling to atomic or molecular states via single-photon (dipole allowed) transitions. These include Adiabatic Rapid Passage (ARP) and variants - Chirped Adiabatic Rapid Passage (CARP)[15–21] and Stimulated Raman Adiabatic Passage (STIRAP)[22]. These approaches are powerful and effective and there is interest in extending them to multi-photon coupling between atomic and molecular levels [7, 23–26]. The thesis work of Carlos Trallero-Herrero [27] showed that for a non-resonant two-photon absorption to proceed efficiently in the strong-field limit, one must appropriately shape the drive pulse to keep its phase and the phase of the atomic coherence in lock-step to counteract the effect of Stark shifts induced by the strong pulse.

This thesis describes a series of strong field experiments, where the electronic dynamics and control possibilities are richer, that aim to extend the above work and advance our understanding of strong field control of multi-state systems with both resonant non-resonant coupling between states. Our approach to strong field control utilizes both parameterized scans of various pulse shapes and closed-loop learning control [6] to identify pulse shapes that

are optimal for populating a target quantum state. Combined with numerical integration of the time-dependent Schrödinger equation, we highlight the difference between sequential population transfer and adiabatic rapid passage in multilevel systems with multiphoton coupling between levels. Additionally, we examine strong field control of a four-level atomic interferometer and show how interference in a target state changes from resonant pathways in the frequency domain to time-domain interference via a singe path.

In addition to controlling single-atoms, interest has developed in controlling an ensemble and work in this area has been growing [28–31]. In particular, the phenomenon of Superfluorescence (SF) (stimulated emission)[32, 33] driven by ultrafast pulses has been demonstrated in Sodium and Rubidium [30, 34, 35]. We further develop work on control over stimulated emission from an ensemble of atoms/molecules and demonstrate that by shaping a strong drive field it is possible to achieve a large degree of discrimination be two emitting atoms/molecules. Currently, there is interest in using the control of stimulated emission to image biological system [36].

The chapter breakdown is as follows. Chapter 2 discusses the laser system used to generate shaped femtosecond pulses as well as how they are characterized. We also discuss how the pulses are shaped in time via optical pulse shaping. Details of the atomic and molecular experiments are then covered where we talk about the atomic and molecular sample cells, as well as how we measure spontaneous and stimulated emission.

Chapter 3 examines the issue of space-time coupling in an optical pulse shaper. There, we both simulate and measure space-time coupling for a specific pulse shape parameter and develop an understanding of when this can become substantial. Lastly we discuss the effect of space-time coupling on the experiments presented in this thesis.

Chapter 4 lays out the theory of two and three-photon absorption in the weak and strong field limits with multiphoton coupling between states. There we first develop an understanding of single photon absorption from an electric field where the amplitude and phase are allowed to vary. We then extend this to the weak and strong field absorption of two photons [12, 15, 37, 38] when there is a resonant intermediate state (Fig. 1.1(a) and a non-resonant intermediate state (Fig. 1.1(b). Going one step further, we extend this to the absorption of three photons with multiphoton coupling between states in both the weak and strong field limits [13, 39].

Chapter 5 presents work on demonstrating a population inversion in a three-level system with multiphoton coupling between the levels. Using closed-loop feedback to discover a pulse that is optimal at populating the exited state, we use the optimal pulse to measure the inversion. The inversion is measured

with a combination of spontaneous and stimulated emission. The experimental results are then compared to theory and we highlight the difference between sequential population transfer and Adiabatic Rapid Passage (ARP) with non-linear coupling between states.

Chapter 6 explores the atomic analog of an interferometer by using the four-level atom where two resonant intermediate states lead to the same final excited state. Using a single shaped femtosecond pulse, we highlight how interference between two quantum paths (defined by resonant frequency component in the weak field limit) changes to interference between resonant and non-resonant pathways and warrants a time-domain description of the dynamics governing the interference.

Chapter 7 takes the learned time dynamics governing chapters 5 and 6 and applies it to an ultrafast analog of Electromagnetically Induced Transparency (EIT). Although much different than conventional EIT, the pump-probe scheme is quite similar only now the pump and the probe are produced with a pulse shaper form a single ultrafast laser pulse. There, we will see that when the atoms are coupled to the pump light, they act as an ultrafast phase modulator for the probe pulse.

Chapter 8 finishes off by using a single shaped pulse to control the superfluorescent emission from two-separate atomic or molecular species. Here, we use closed-loop feedback to discover a pulse that is optimal for suppressing emission from one atom/molecule while maintaining or enhancing the emission from the other. We then perform a systematic study of superfluorescent emission using a single shaping parameter to understand the underlying control mechanism.

Chapter 9 gives concluding remarks and observations, followed by an appendix for mathematical derivations and source code related to simulation presented throughout the thesis.

Chapter 2

Experimental Setup

2.1 Laser System

Our laser system consists of a KM Labs Kerr-lens mode-locked oscillator and multi-pass amplifier that both employ Titanium:Sapphire as a gain medium. The oscillator is pumped by a Coherent Verdi V5 Continuous Wave (CW) laser and the amplifier by a Quantronix CW-pumped Q-switched Nd:YLF laser. At its output, the laser system produces 30 femtosecond (fs) pulses at a repetition rate of 1 kHz. The central wavelength is 780 nm and the bandwidth (as measured by the full-width at half-maximum) is approximately 30 nm. A typical laser pulse is shown in Fig. 2.2 When tightly focused, the amplified pulses can produce field strengths on the order of the atomic unit of field: 5.14×10^{11}V/m. This system provides the core tool we use to investigate the dynamics of atoms and molecules on their natural time scales and in the strong field limit.

The pulses are characterized in time by Second Harmonic Generation (SHG) Frequency Resolved Optical Gating (FROG) [40]. In SHG FROG, (simply FROG) one splits the pulses into two arms of an interferometer and then spatially and temporally recombines them in a nonlinear crystal, while measuring the spectrally-resolved cross-correlated SHG spectrum for different delays between the two arms. In this way, the electric field amplitude and phase can be retrieved by an appropriate algorithm and thus the electric field can be reconstructed.

2.2 Pulse Shaper

The pulses from our laser amplifier are conveniently described in time as Gaussian with a full-width-at-half-maximum of approximately 30 fs and constant

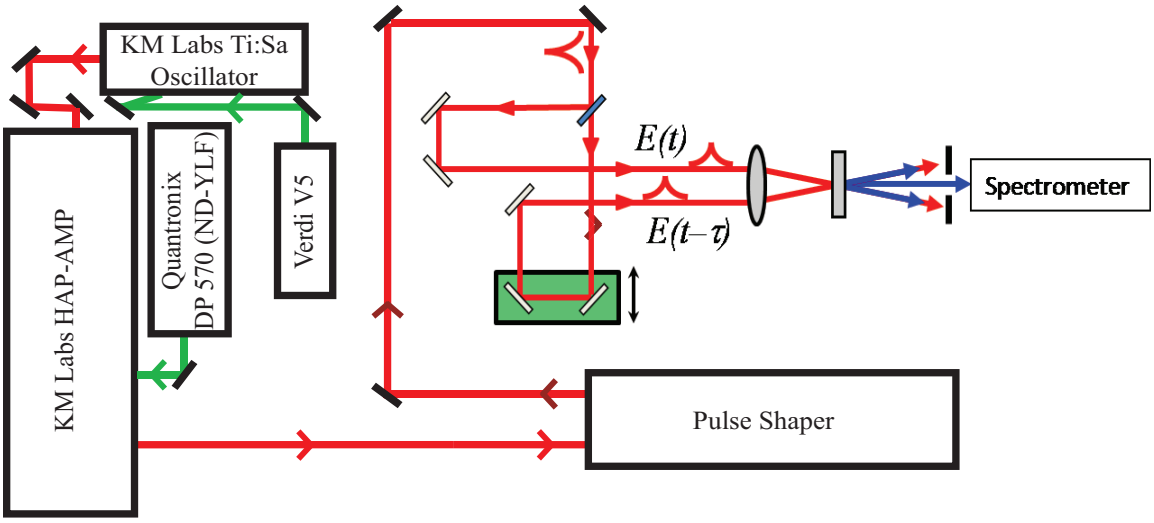

Figure 2.1: Laser system and SHG FROG [40] set up to characterize the pulses.

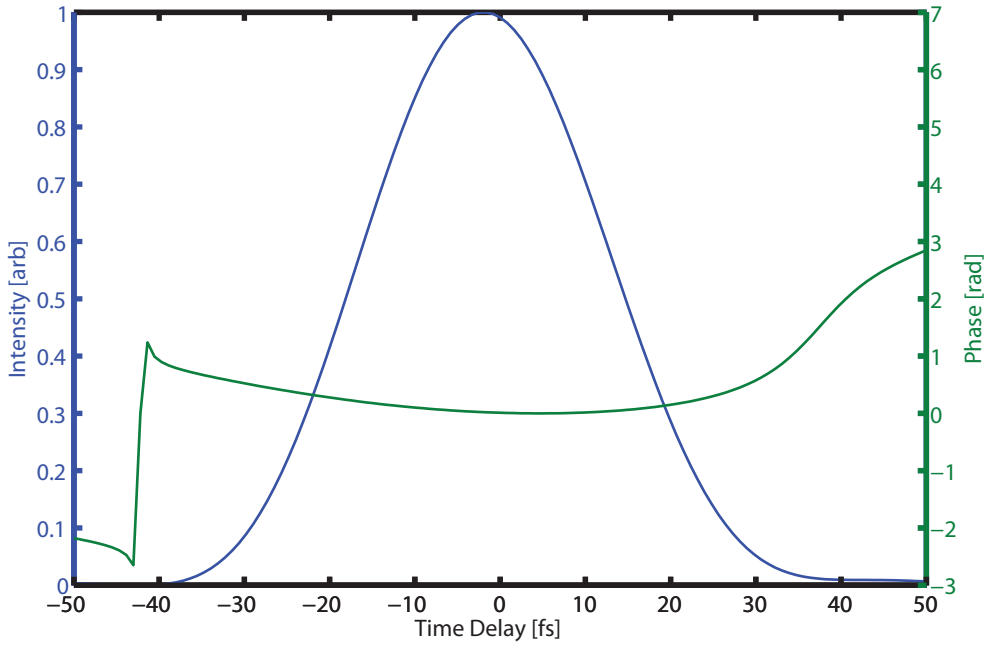

Figure 2.2: Pulse from our laser amplifier. The pulse was characterized using SHG FROG [40].

phase over the pulse duration. In general (and for many experiments presented in this thesis), this is not optimum for driving various physical processes; and in particular, processes that are not linearly proportional to the electric field. Therefore, it becomes necessary to be able to shape the electric field in time. To achieve this we employ the technology of frequency domain optical pulse shaping. At the heart of the experiments presented here is quantum control and in a certain sense the ability to effect quantum control relies on reshaping the electric field in time.

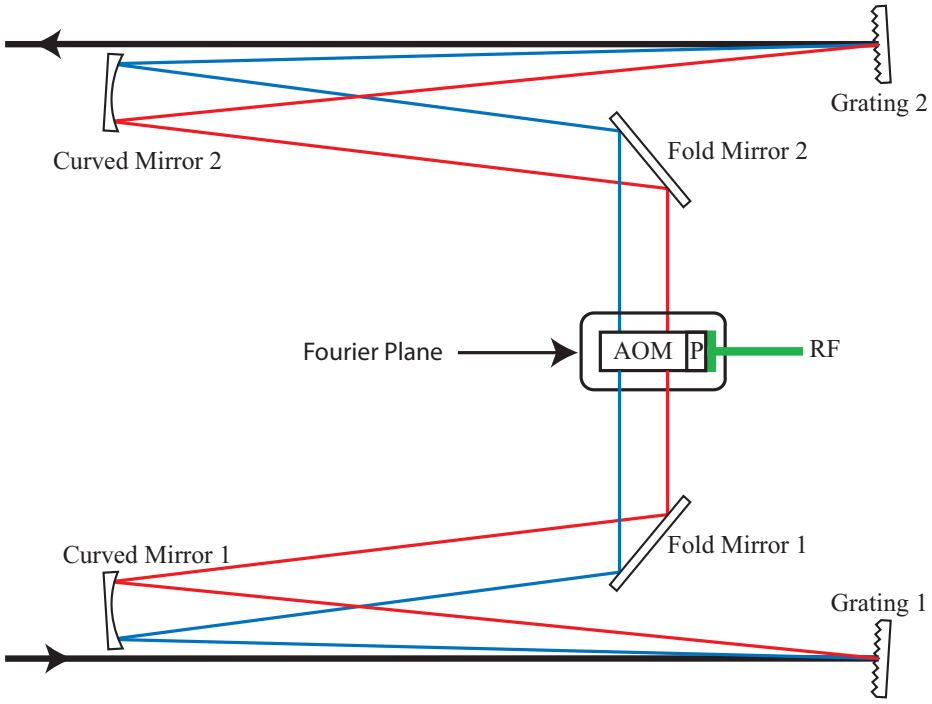

Figure 2.3: Pulse shaper layout. Our pulse shaper consist of two gratings (671 grooves/mm), two curved mirrors (750 mm focal length), two fold mirrors, and a programable SLM at the Fourier plane called an AOM. P is the piezoelectric transducer use to launch the acoustic wave and RF is the radio frequency waveform used to drive it.

Developed in the early 1990s, optical pulse shaping exploits the trick of Fourier transforming the pulse to the frequency domain [41]. There, one can modify the phase and amplitude of each frequency component and simply inverse Fourier transform back to achieve a new pulse in time. We note that shaping the pulse in the time domain directly is impossible because of its short duration (30 fs) compared to the speed of any electrical device. Figure 2.3 shows the layout of our pulse shaper. The pulse is incident at approximately

Littrow angle on a grating one focal length f from a curved mirror. Upon reflection from the curved mirror, the light is subsequently focused another focal length f away at the Fourier plane where we now have each color in the laser spectrally separated in space. At the Fourier plane we place a programmable Spatial Light Modulator (SLM) called an Acousto-Optic Modulator (AOM)[4]. An AOM uses a piezoelectric transducer to launch an acoustic wave down a crystal, from which the light is diffracted. The transducer is driven by a 150 MHz radio frequency wave from a GaGe 11G CompuGen arbitrary waveform generator, where the amplitude and phase of the radio wave are allowed to vary in time. Changing the amplitude and phase of the wave driving the transducer directly changes the amplitude and phase of the acoustic wave in the crystal. Because the light is diffracted from the acoustic wave, one is able to change the amplitude and phase of each frequency component in the pulse. The diffracted light is subsequently sent off another curved mirror and focused onto a second grating to spatially recombine the frequencies. By launching different acoustic waves, we can generate light pulses with different spectral phases and amplitudes and therefore different temporal characteristics for our experiments. Our pulse shaper can access roughly 170 different spectral components.

2.3 Optimization Algorithm

One of the central tenets of quantum coherent control is that a desired quantum state of a system can be achieved by modifying the Hamiltonian to actively steer the system from an initial state to a desired final state. For systems described in this thesis, the electric field is embedded within the Hamiltonian through the dipole approximation. Therefore, modifying the Hamiltonian amounts to modifying the electric field driving the system. However, often times the way in which the Hamiltonian needs to be modified, or the Hamiltonian of the system itself, is not known a priori. One successful approach to discovering the Hamiltonian, and hence electric field, in achieving a desired quantum state is by "trial and error": iteratively modify the electric field and use feedback in a closed loop to discover the electric field, or Hamiltonian, that corresponds to achieving a desired quantum state [42]. We use a closed-loop feedback approach throughout the work presented here, and in particular make us of a Genetic Algorithm (GA) modeled after biological evolution. The details of our GA have been described elsewhere [43], but we give a brief overview of how it works.

We first start with a family of randomly selected pulse shapes. Each pulse shape is then used in the experiment (i.e., used to excite a transition), with each pulse shape producing its own experimental yield. We then rank the dif-

ferent pulse shapes according to how much experimental yield (called Fitness) each one produces. The pulse shapes which produce the most experimental yield are retained and those which produced the least experimental yield are discarded. New pulse shapes are then produced bases on the ones we retain [43] and the process repeats. With each successive iteration (Generation), the algorithm converges onto a pulse that is optimal pulse for producing the maximal experimental yield (i.e., light at a particular wavelength, fragments of a molecule, etc.). Figure 2.4 shows yield of an experimental signal as a function of generation. For many of the experiments presented here, by approximately 160 generations, the GA has converged and an optimal solution has been found.

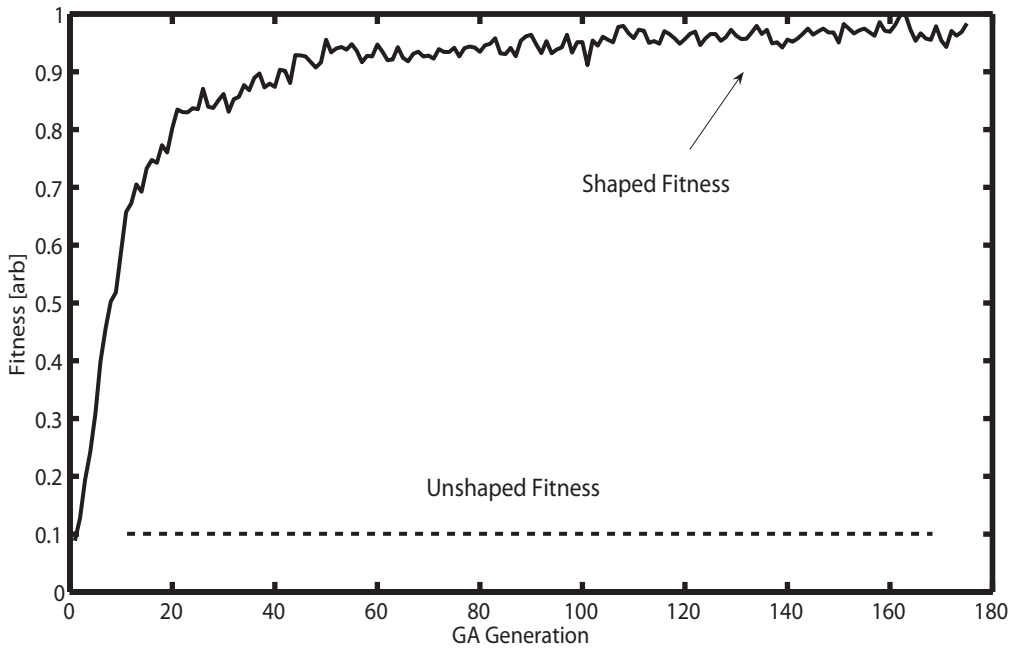

Figure 2.4: Fitness as a function of generation for the Genetic Algorithm. Here, fitness is fluorescence yield from the 7p state of atomic Sodium after three-photon absorption from the 3s ground state. This system is explored further in chapter 5.

2.4 Atomic and Molecular Cells

The work presented in this thesis involves both atoms in gas phase and molecules in liquid phase. In the atomic experiments, we study both single and multi-

photon transitions in Rubidium (Rb) and Sodium (Na). For Rubidium, we use a 6 cm long glass cell which has been back-filled with Rb and sealed off. Because Rb is not a gas at room temperature, the cell must be heated. Therefore the cell is first wrapped in heating tape and then wrapped with aluminium foil, leaving only two openings for the beam to enter and exit, as well as an opening at 90 degrees with respect to the beam propagation direction to capture fluorescence from the excited atoms. Typically, the cell is heated to 150 ^oC and inside, the Rb vapor pressure is given by [44],

$$\log_{10} P_v = 15.882 - \frac{4529.6}{T} + 0.000586T - 2.991 \log_{10} T \tag{2.1}$$

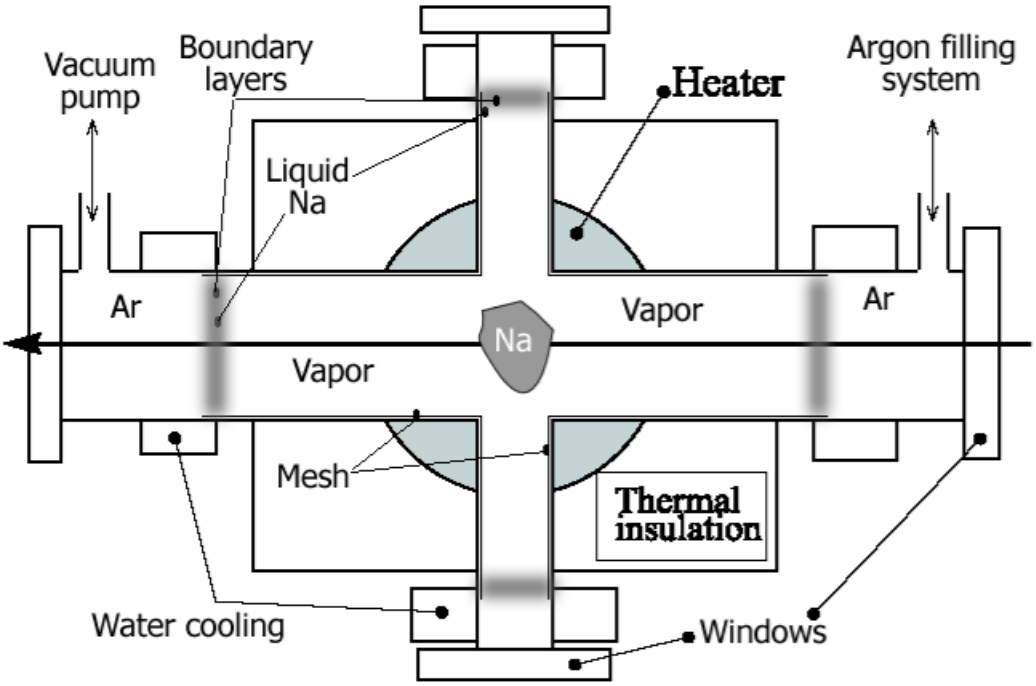

Figure 2.5: Heat pipe layout.

For Sodium, it is difficult to achieve a high enough vapor pressure in such a small cell at similar temperatures without coating the inside of the glass with Sodium atoms. Figure 2.6 shows the density of Rubidium and Sodium as a function of temperature where it's clear that Rubidium is orders of magnitude higher in density than Sodium for a given temperature. Therefore, we employ a heat pipe oven design to achieve a high enough vapor pressure for the experiments while minimizing the likelihood of having the Na react with the glass windows. Details of the heat pipe oven are given in [43], but we briefly

describe it here. Figure 2.5 shows the layout of the oven. The chamber has a cross-pipe design so that fluorescence form the excited atoms can be imaged onto a photomultiplier tube (PMT) at 90 degrees with respect to the beam propagation axis. Solid Na is heated between 200 and 400 celcius at the center of the oven, resulting in Na vapor with a pressure given by [45],

$$\log_{10} P_v = 133.429 - \frac{9302}{T} + 0.031144T - 49.367 \log_{10} T. \tag{2.2}$$

The oven is back-filled with Argon (Ar) gas and has cooling jackets to prevent Na from coating the oven windows. As the Na vapor expands toward the cooling jackets, it condenses onto a stainless steel mesh grid upon exchanging energy with cool argon atoms. Through capillary action the Na reaches the center of the pipe and the process repeats resulting in a steady state of Na vapor pressure.

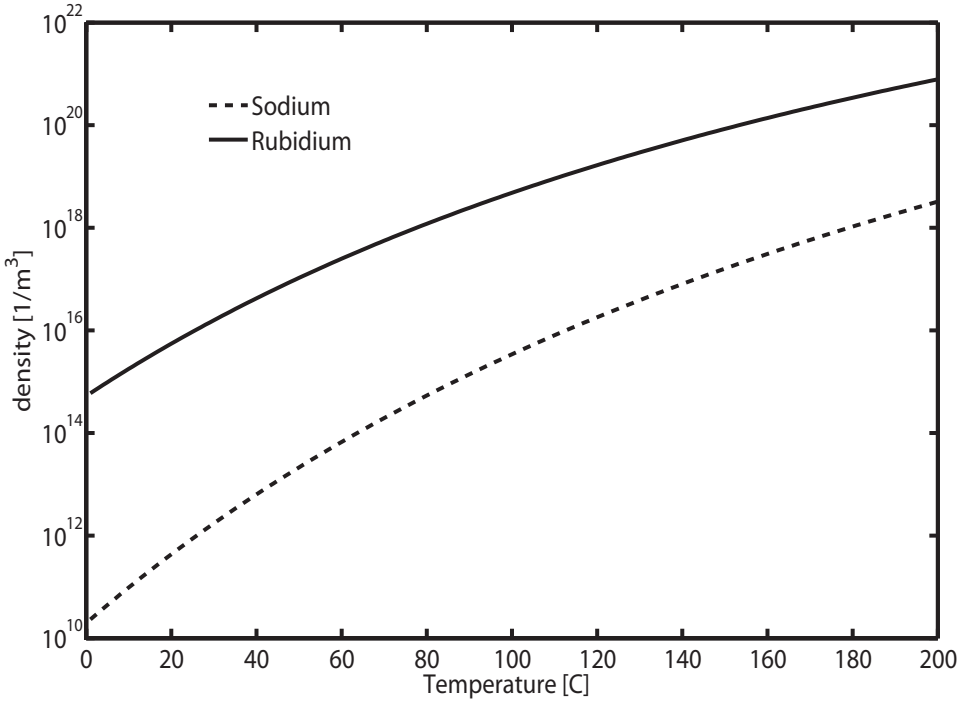

Figure 2.6: Calculated density ($1/m^3$) vs temperature (Celsius) according to Eqs. 2.2 and 2.1. The solid line corresponds to Rubidium and the dashed line Sodium.

For the molecules in liquid phase, we use two 6 cm long glass cells containing DCM (4-dicyanomethylene-2-methyl-6-p-dimethylaminostyryl-4H-pyran) and

Ruthenium $[Ru(dpb)_3](PF_6)_2$ (dpb is 4,4'-diphenyl-2,2'-dipyridine) dissolved in Methanol. Both DCM and Ruthenium are two-photon absorbing dyes.

2.5 Imaging System and Spatial Shaping

The experiments presented here utilize a particular laser beam profile that we achieve through an imaging system. In particular, we seek a beam with a long Rayleigh range to minimize intensity variation in the longitudinal direction. To achieve this, the pulses from our pulse shaper are sent through a 1 m focal length lens. Subsequently, that focus is imaged using a 0.6 m lens to a focus with a magnification factor of ~ 3.6. This effectively produces a Rayleigh range of 19 cm.

In experiments involving Na, the absorption of two photons strongly depends on the intensity of the pulse and not the field. Therefore, changes to the two-photon absorption as a function of intensity for a beam with a Gaussian transverse spatial profile can be washed out - an effect called Volume Averaging. Thus, it becomes necessary to ensure a uniform distribution of intensities as a function of space. To achieve this, we spatially shape the beam by placing a 100 μm diamond pinhole (Lenox Laser HP-3/8-DISC-DIM-100) at the focus of the 1 m long lens. Then, the spatially shaped mode is imaged into the heat pipe oven or cell, resulting in a 360 - 400 μm spot size. An example of the kind of flat intensity profile we can achieve is given in Fig. 2.7. Figure 2.7(a) and (c) show the 2D spatial distribution and lineout, respectively, one can expect without spatially shaping the beam. However, Fig. 2.7(b) and (d) show the distribution achieved with spatial shaping.

2.6 Measurement of Spontaneous and Stimulated Emission

As mentioned and shown in Fig. 2.8, spontaneous emission from the exited atoms was imaged at 90 degrees with respect to the beam propagation axis onto a PMT with single-photon sensitivity (RCA IP 21) using an f2 lens (focal length is twice the diameter). Having a PMT to collect fluorescence allows us to measure the excited state population in the atoms. For experiments where it is necessary to image a spatially shaped beam to a focus, we place an iris ($\sim$ 1 mm opening) in front of the PMT to ensure that we only collect fluorescence from the longitudinal location (focus) where the intensity distribution is flat. Fluorescence from various excited states of the atom can be selected by placing a bandpass filter in front of the PMT. A list of the bandpass filters we use to

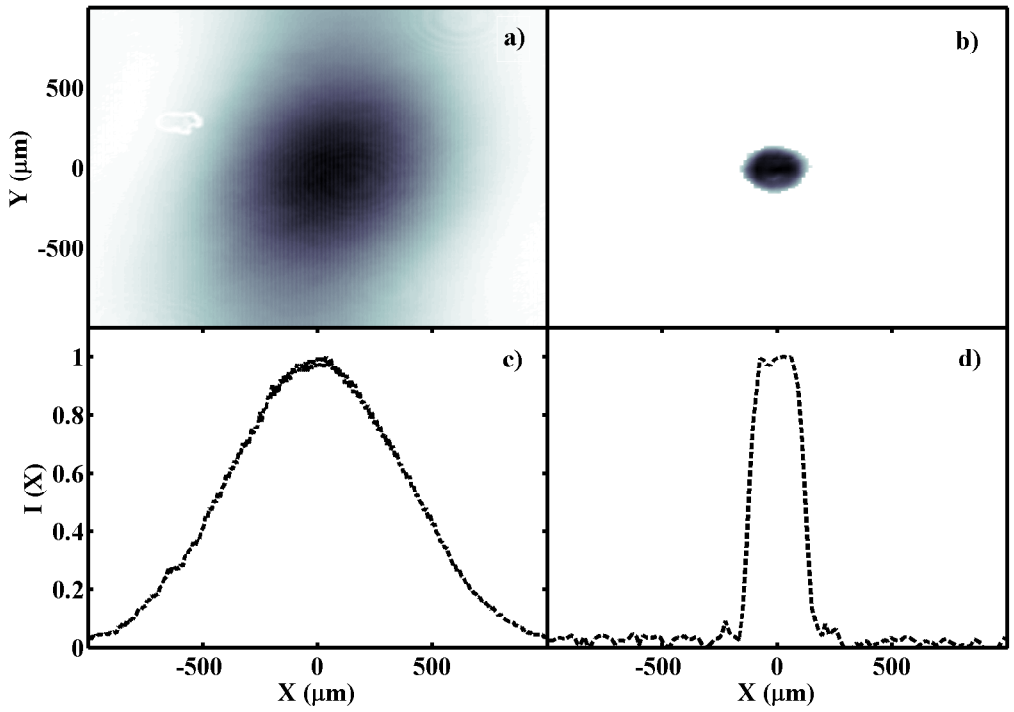

Figure 2.7: a) Mode without spatial filter. b) Mode with spatial filter. c) and d) are an average of 5 line-outs of a) and b), respectively, over the transverse coordinate Y.

isolate spontaneous emission lines, along with their specs, are given in chapter 5.

In other experiments presented in chapters 7 and 8, we measure stimulated emission and employ two main schemes for its detection. When sufficiently pumped, atoms and molecules can give off stimulated emission in the form of superfluorescence [46]. In this case, superfluorescence was measured in the forward direction using large aperture photodiodes (Thorlabs DET 100A), as illustrated in Fig. 2.8 and labeled D1 and D2 for detector 1 and detector 2. In chapter 8 we aim to control the stimulated emission form two separate atoms or two separate molecules by appropriately shaping the pulse. In this case, it is convenient to combine both photodiode signals using a signal combiner and BNC cable to delay one signal with respect to the other. In chapter 7, we make use of one cell alone and use two pulses to control an ensemble of Rubidium atoms in a traditional pump-probe experiment. In this case we are interested in mapping out the spectrum of one of the two pulses (probe) as it propagates through the atoms while the atoms are under the influence of the other pulse (pump). To measure this, we couple the light into an Ocean Optics HR4000 spectrometer with 0.16 nm resolution and measure the spectrum of the probe light as a function of delay between the pump and the probe. In this case, we swap the photodiode with the spectrometer at, for example, D1 in Fig. 2.8.

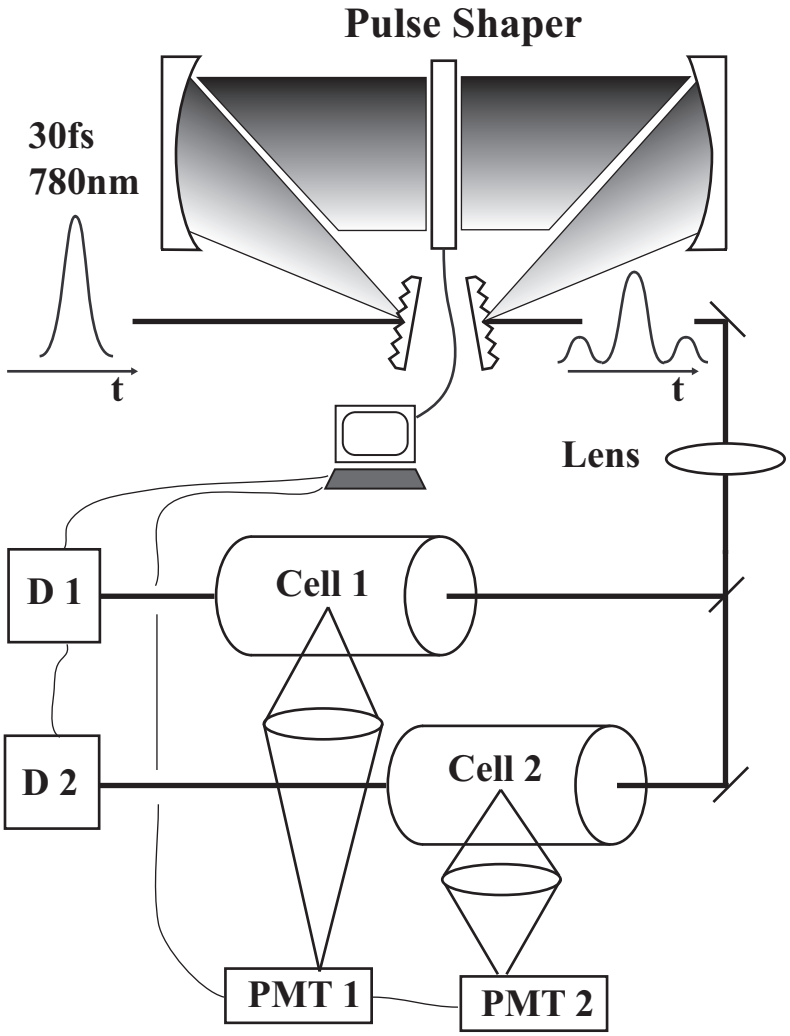

Figure 2.8: Our experimental setup. 30 fs pulses were shaped by an AOM based pulse shaper and split into two arms. Each arm was focused into a cell containing either an atomic or molecular sample.

Chapter 3

Space Time Coupling

In this chapter we examine a technical issue related to optical pulse shaping which has seen interest in recent years [47–49], namely coupling between the temporal and spatial variables describing a pulse after passing through a 4f optical pulse shaper - called space-time coupling. The number of experiments employing ultrafast optical pulse shaping has grown enormously and most implementations make use of a programmable spatial light modulator at the Fourier plane of a zero dispersion stretcher [50], shown in Fig. 2.3. There have been some calculations of the inherent space-time coupling associated with this scheme [51–54] and how it affects the spatial mode of the shaped laser pulses. In this chapter we measure an calculate space-time coupling in our acousto-optic modulator (AOM) based pulse shaper by measuring the spatial mode of the output as a function of pulse shape and compare our measurements to calculations. Several pulse shape parameterizations were studied in our measurements, but we only show data and calculations for the case of a sinusoidal phase modulation, as it captures the essential physics and illustrates the type of coupling one might expect. Additionally, we examine if spatial shaping of the beam effects the temporal structure of the pulse also as a result of space-time coupling.

3.1 Modeling the Pulse Shaper

To fully understand the effect of space-time coupling in a pulse shaper, it is necessary to model its various optical elements. Thus, we aim to simulate the spatial mode of a pulse shaper output and check the predicted mode with experimental measurements. The formulae below used to describe the pulse shaper are not specific to AOM pulse shaping, and may be used by any pulse shaper that makes use of gratings and a spatial light modulator at the Fourier

plane. Throughout this section the laser propagates in the Z direction and the vertical (transverse) spatial coordinate Y is omitted because the treatment of each element in the pulse shaper only depends on the horizontal (transverse) spatial coordinate X. We also observe this experimentally. Following the formalism laid out in [51], we calculate the electric field at each stage of the pulse shaper. As input for the calculations, we use a measured spatial mode from our laser amplifier and consider lineouts averaged over the transverse spatial coordinate y. This roughly corresponds to a Gaussian envelope in x, 1.9 mm in width, but with minor additional features introduced by the amplifier. Additionally, we use a Gaussian pulse envelope in time for simplicity. Using this initial space-time profile, we propagate the field through each optical element of the pulse shaper, finally yielding a field in space and time at the pulse shaper output.

Consider a 4f pulse shaper consisting of two gratings, two lenses, and an AOM located at the Fourier plane, as shown in Fig. 2.3. First, the pulses are incident on a diffraction grating, where a grating maps frequency to angle as follows,

$$E_{out} = E_{in}(\alpha x, t - \beta x). \tag{3.1}$$

The parameters α and β characterize the diffraction gratings:

$$\alpha = \frac{cos(\theta_i)}{cos(\theta_d)}, \tag{3.2}$$

$$\beta = \frac{2\pi p}{\Lambda cos(\theta_d)\omega_0}, \tag{3.3}$$

where p is the diffraction order, Λ gives the groove spacing, ω_0 is the pulse central frequency, and θ_i and θ_d are the incident and diffracted angles, respectively. In our lab, $\alpha = 1$ since the gratings are Littrow configured. Between any two elements in the pulse shaper one can formally describe propagation from one element to another by treating the propagation as if it were through a dispersive medium. However, the treatment is drastically simplified by the fact that propagation happens in air where dispersion is negligible. Propagation between any two elements in the pulse shaper is conveniently given in the Fourier domain as

$$\hat{\tilde{E}}(\xi, \omega, z) = \hat{\tilde{E}}(\xi, \omega, 0) exp(ik(\omega)z) exp(-i\frac{\xi^2}{2k(\omega)}z), \tag{3.4}$$

where $k(\omega)$ is the wave vector at frequency ω, and ξ is spatial frequency. Let

us first expand $k(\omega)$

$$k(\omega) = k_0 + k_0'(\omega - \omega_0) + \frac{1}{2}k_0''(\omega - \omega_0)^2 + ...+, \tag{3.5}$$

where $k_0' = \frac{\partial k(\omega)}{\partial \omega}|_{\omega=\omega_0}$ and $k_0'' = \frac{\partial^2 k(\omega)}{\partial \omega^2}|_{\omega=\omega_0}$. Because dispersion is negligible in air, k_0' and k_0'' vanish and we only keep the term k_0, where $k_0 = \frac{2\pi}{\lambda_0}$ and λ_0 is the central wavelength of the laser. Under the paraxial wave approximation, the action of a thin lens on a femtosecond pulse can be derived geometrically and is given as [55],

$$E_{out} = E_{in}exp(ik_0nd)exp(\frac{-ik_0x^2}{2f}), \tag{3.6}$$

where d is the lens thickness, f is the focal length of the lens, and n is the index of the glass. Lastly, the effect of the mask is rendered by multiplying the electric field by a complex masking function. Since the mask is fixed for a given pulse shape, it only acts to modify the amplitude and phase of each frequency and can be simply written as

$$E_{out}(x, \omega)) = M(\omega)E_{in}(x, \omega). \tag{3.7}$$

Here, M(x) is the masking function and has the form

$$M(\omega) = A(\omega)exp(i\phi(\omega)). \tag{3.8}$$

We choose only phase shaping so that $A(\omega) = 1$ and $\phi(\omega) = \pi sin(\omega T)$ (i.e., not amplitude shaping) and T is the period of the sinusoid.

Using the equations given above, we can numerically simulate the output of a pulse shaper for an arbitrary pulse shape. For simulations described below, we sample at a rate of 0.01 mm in space and 8.0 fs in time and start with a space-time grid set ±30 mm by ±8485 fs in size. The output of the pulse shaper in space and time is then achieved by implementing the appropriate formula at each corresponding element. Finally, integrating over time gives the spatial distribution of the pulse in the direction of the AOM as seen by the dashed curve in Fig.3.1.

3.2 Measurements

As indicated in Fig. 2.3, the beam is sent through a pulse shaper consisting of two Littrow configured gratings (671 g/mm), two curved mirrors (750 mm focal length), two folding mirrors, and an (AOM) 35 mm in length located at

the Fourier plane. We note there is effectively no difference in the simulations between a curved mirror and a lens. However, in practice there is because of dispersion through a dispersive medium.

To measure spatial distortion caused by the SLM, we pointed the laser beam output by the pulse shaper directly onto the chip of a 1024 by 1280 pixel CCD camera (Electrim) after reducing the beam intensity by a series of neutral density filters. [1] We use a waveform generator (GaGe 11G CompuGen) to drive a piezoelectric transducer used to launch an acoustic wave across the AOM. With it we can create arbitrary phase and amplitude profiles across the AOM by modulating the amplitude and phase of a 150 MHz carrier signal. The radio frequency wave from the waveform generator has the form $s(t) = A(t)sin(2\pi f_0 t + \phi(t))$ where A(t) is the RF wave amplitude and $\phi(t)$ is the phase. We note here that frequency and time used to drive the transducer can be converted to velocity and position of the acoustic wave. For the measurements here we only modulate the phase of the RF wave (and therefore the ultrafast pulse) using a sinusoidal phase given by the form

$$s(t) = sin(2\pi f_0 t + \pi sin(2\pi \Omega t)). \tag{3.9}$$

Here, f_0 is 150 MHz, t is time, and Ω is the sinusoidal modulation frequency. The choice of Eq. 3.9 as a pulse shape is motivated by the fact that a sinusoidal phase will produce additional sub-pulses in time. The sub-pulses are spaced in time according to $1/\Omega$ in Eq. 3.9 and have amplitudes governed by the amplitude of the sinusoidal phase. If v_a represents the acoustic velocity, k the number of acoustic wave periods per millimeter, and x the position across the AOM, then (3.9) can be recast to read

$$s(x) = sin(2\pi f_0 \frac{x}{v_a} + \pi sin(2\pi k x)). \tag{3.10}$$

With a length of 35 mm and an acoustic velocity of 4.2 mm/μs, we program the AOM to sweep k from 0 to 2.77 periods/mm in steps of 0.15 while taking snap shots of the laser mode at each step. We focus on two values of k: 0.29 and 1.63 periods/mm.

As discussed in Chapter 2, there are cases where we need to ensure a uniform spatial distribution of intensities. In order to achieve this, we spatially filter the beam by focusing on to a spatial aperture, and then image the spatially apertured beam to a focus. To check that the temporally shaped beam is

[1] It should be noted that a GRENOUILLE [56] is not suitable for pulses longer that approximately 250 fs, and would therefore fail to capture interesting space-time coupling features predicted by our simulations. Further, pulses stretched to 250 fs will not exhibit much space-time coupling.

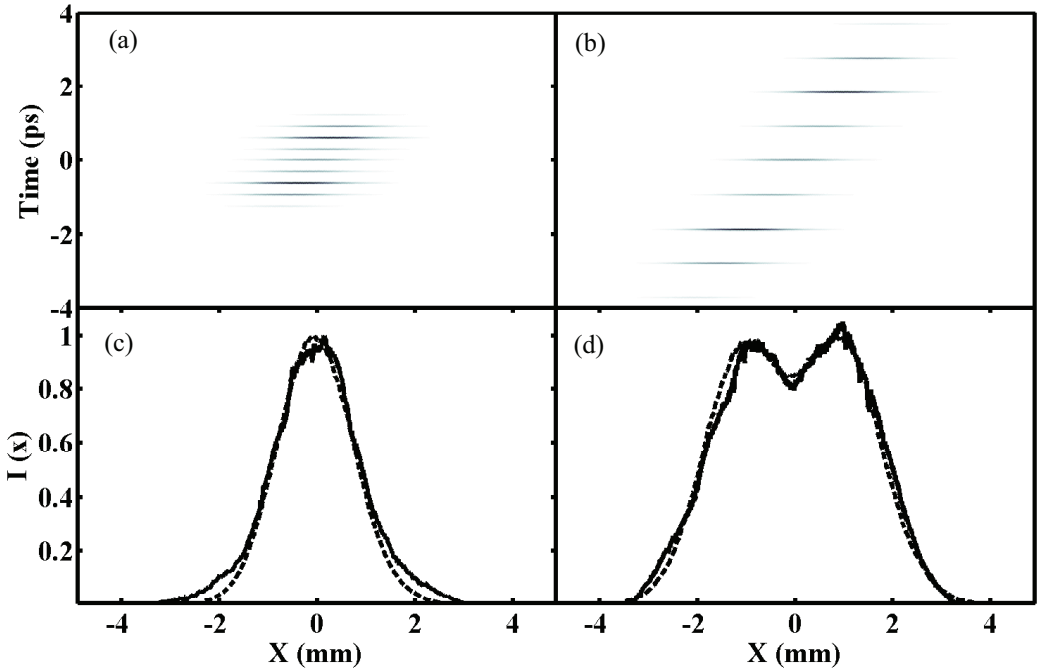

Figure 3.1: Measured and calculated space-time coupling in a 4f optical pulse shaper. a) Calculated intensity in space and time I(x,t) for k = 0.29 cycles/mm on the AOM. b) Predicted (dashed) and measured (solid) marginal of I(x,t) on x. c) Calculated intensity in space and time I(x,t) for k = 1.63 cycles/mm on the AOM. d) Predicted (dashed) and measured (solid) marginal of I(x,t) on x. The spatial variable x is taken across the beam mode, in the direction of the AOM.

not affected by the aperture, we also simulate and measure the effects of both spatially and temporally shaping the pulse together. Using the pinhole and imaging system mentioned before, we applied a sinusoidal phase modulation to our SLM and sent the beam through the 100 μm pinhole. Then we measured the pulses in time via SHG FROG both with and without the pinhole and the results can be seen in Fig. 3.2. Here, all cases agree reasonably well with each temporal lobe displaced in time as expected. The difference inherent in measured pulses with the pinhole vs without likely resulted from dispersive material in the imaging system used to get the beam through the pinhole.

3.3 Results and Discussion

Our results are summarized in Fig. 3.1 and are general to other spatial light modulators. As well panels (a) and (b) show calculated shaped pulses for the two cases mentioned earlier: $k = 0.29$ and $k = 1.63$ periods/mm in Eq. 3.10. The dashed curves in panels (c) and (d) show the marginal over time of (a) and (b), respectively. The solid curves in (c) and (d) correspond to lineouts of the measured spatial mode for each of the two cases. As shown in panels (b) and (d), when the number phase cycles/mm across the AOM is substantial, spatial distortion of the laser is present. However, when the number of cycles/mm is less, spatial distortion as a result of space-time coupling is small. This can be understood from the point of view that the mask modulates the spatial profiles of individual frequency components and therefore cannot be perfectly recombined spatially by the second grating. For an ideal 4f pulse shaper with no mask, the first grating alters the spatial profile for each frequency component, which is then perfectly reversed by the second grating. However, the addition of a mask introduces an additional spatial profile for each frequency in the bandwidth, which cannot be compensated for by the second grating. The effect of this is to create a time-dependent spatial translation, as can be seen in panels (a) and (c) of Fig. 3.1. Because a sinusoidal phase modulation creates a family of sub-pulses in time, this phase shaping profile nicely captures the effect of space-time coupling when the pulse is stretched in time.

A consequence of using a spatial light modulator at the Fourier plane of a 4f optical pulse shaper is that space-time coupling is unavoidable. However we see in Fig. 3.1 that if k (for a sinusoidal phase profile) is small, space-time coupling is small. More generally, when the phase change per unit of frequency is large, distortion of the spatial mode is present. This can be seen in Fig 3.1 panels (b) and (c) when the number of phase cycles per millimeter (or per unit of frequency) became substantially larger than panels (a) and (c). The tilt given to the temporally shaped pulse as a function of space (panels (a)

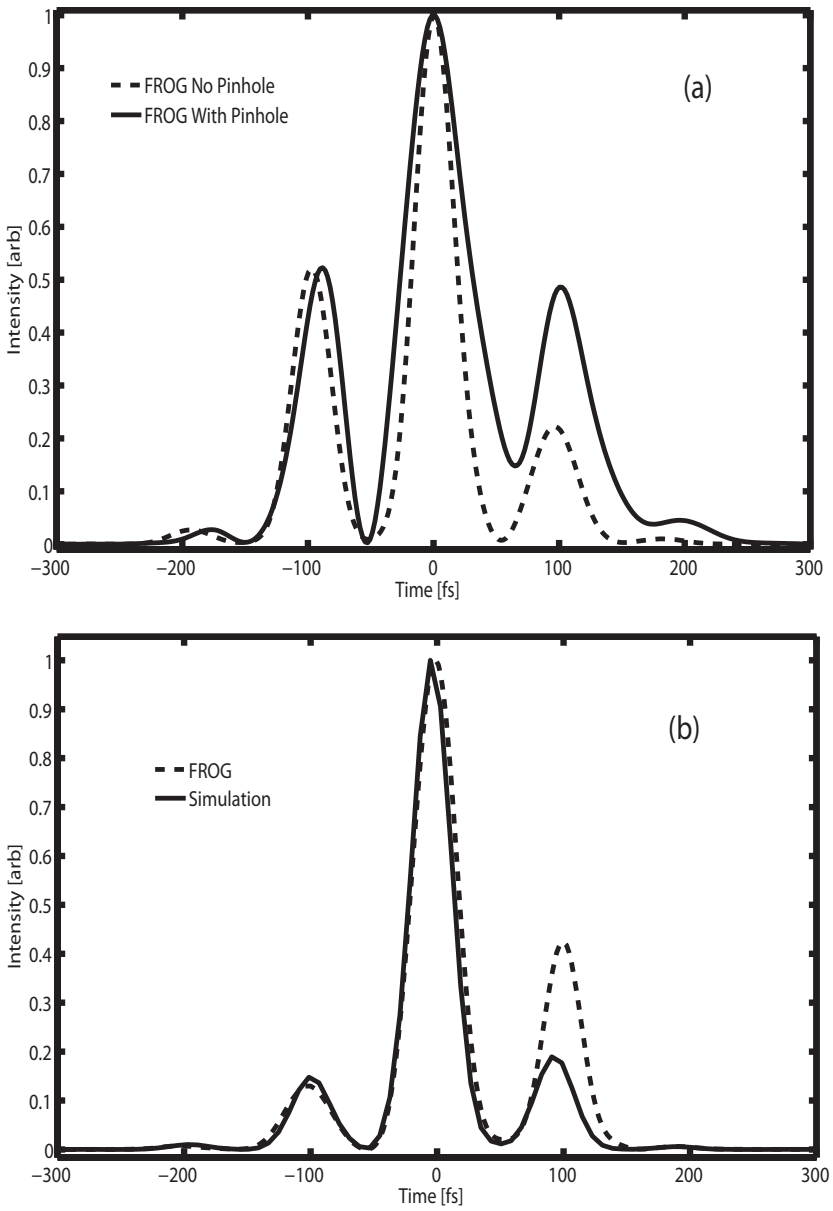

Figure 3.2: Temporal and spatial shaping a) Measured pulses with and without spatial shaping for a sinusoidal phase modulation b) Measured and simulated pulses for a sinusoidal phase modulation.

and (b)) is ultimately governed by the ratio of Eqs. 3.2 and 3.3 [51],

$$\frac{\alpha}{\beta} = \frac{\Lambda cos(\theta_i)\omega_0}{2\pi p}. \tag{3.11}$$

Given that $\alpha = 1$, $\Lambda = 1/671$ mm groove spacing, p = 1, $\lambda_0 = 780$ nm and $\theta_i = sin^{-1}(\frac{p\lambda_0}{2\Lambda}) = 0.2648$ radians, we find that $\beta^{-1} = 0.55$ mm/ps. Thus, a pulse stretched to 0.5 ps FWHM can expect it's spatial mode to stretch by 0.28 mm relative to an unshaped pulse.

From here, it's worth discussing the fact that most ultrafast coherent control experiments are performed in a focus. In a focus, each frequency component and sub-pulse comes to the same place in space. Working in a focus not only allows high enough field strengths to be achieved, but it removes the lateral spatial translation of each temporal sub-pulse (for the case of a sinusoidal phase modulation) while maintaining the pulse's temporal order. Diffraction of the laser at the Fourier plane by the AOM distorts the laser k vectors and therefore the laser's spatial distribution in the far field. This follows from the fact that the far-field diffraction pattern is given by its spatial Fourier transform. If you then subsequently focus the far-field beam (e.g. into an atomic/molecular sample) spatial distortion becomes k-vector distortion in the focus where the experiment takes place. Therefore, space-time coupling introduced by the pulse shaper is rendered minimal by working in a focus. Further, working in a focus helps us ensure that spatially filtering the beam doesn't clip any temporal features present in a shaped pulse that may have been laterally translated because of space-time coupling. This is demonstrated in Fig. 3.2(a) where the time structure remains intact (although modified because of dispersion) after passing through a pinhole. All experiments presented in this thesis we performed in a focused geometry.

Chapter 4

Theory

This chapter covers the theoretical background for experiments presented in subsequent chapters. In it, we cover single and multiphoton excitation by weak and strong femtosecond pulses. For the work in this thesis, we use Alkali atoms to study electronic excitation by ultrafast laser pulses. Therefore, the systems we study can be considered Hydrogen-like, where we neglect the motion of core electrons and the nucleus, and only consider the outer shell S-state electron. In this case, we are only concerned with how an electron is coupled to a laser field, where the standard treatment makes use of the dipole approximation. A very well studied system in atomic physics is the two-level atom coupled to an electric field. From this, the concept of a coherent excitation rate is formed (Rabi frequency), as well as how it depends on detuning and the light field intensity. This system can then provide the foundation for what happens when the laser field becomes strong and other effects start to play a more prominent role.

4.1 Single Photon Absorption

Consider a field-free two-level atom in an energy basis with eigenfunctions given by

$$\hat{H}_0 \left|i\right\rangle = \hbar\omega_i \left|i\right\rangle , \tag{4.1}$$

where i = g,e. The wavefunction for the system can be written as,

$$\psi(t) = a_g(t)e^{-i\omega_g t}\left|g\right\rangle + a_e(t)e^{-i\omega_e t}\left|e\right\rangle , \tag{4.2}$$

where $|g\rangle$ and $|e\rangle$ denote the ground and excited states, respectively, $\omega_g = E_g/\hbar$, $\omega_e = E_e/\hbar$, and the complex coefficients $a_g(t)$ and $a_e(t)$ must satisfy $|a_g(t)|^2 + |a_e(t)|^2 = 1$. If this system is coupled to an electric field whose carrier

frequency and envelope are allowed to vary in time, then their interaction under the dipole approximation is written as,

$$\hat{H}_{AF} = -\boldsymbol{\mu} \cdot \boldsymbol{\epsilon}(t). \tag{4.3}$$

Here, $\hat{\mu}$ is the atomic dipole moment and $\boldsymbol{\epsilon}(t)$ is the electric field where,

$$\boldsymbol{\epsilon}(t) = \frac{\boldsymbol{E}(t)}{2} e^{-i\omega_0 t} e^{i\phi(t)} + c.c., \tag{4.4}$$

and ω_0 is the central frequency of the light field, $\phi(t)$ is the temporal phase, and $E(t)$ is the pulse envelope. Then, the the interaction has matrix elements in the field-free energy basis given by,

$$\langle i| \hat{H}_{AF} |j\rangle = -\mu_{ij}\epsilon(t), \tag{4.5}$$

where for linearly polarized light, $\mu_{ij} = \langle i| \hat{\mu} \cdot \hat{\epsilon} |j\rangle = \mu_{ji}$. For the Alkali atoms we study, many of the dipole matrix elements are tabulated [57]. The time evolution of the wavefunction ψ(t) is governed by the Schrodinger equation

$$\frac{\partial}{\partial t}\psi(t) = \hat{H}(t)\psi(t), \tag{4.6}$$

where $\hat{H}(t) = \hat{H}_0 + \hat{H}_{AF}(t)$. Then, the evolution of the time-dependent coefficients in the interaction representation are,

$$\dot{a}_g(t) = \frac{i\mu_{ge}E(t)}{2\hbar} \left(e^{i(\omega_0 - \omega_{eg})t - i\phi(t)} + e^{-i(\omega_0 + \omega_{eg})t + i\phi(t))}\right) a_e(t) \tag{4.7}$$

$$\dot{a}_e(t) = \frac{i\mu_{eg}E(t)}{2\hbar} \left(e^{i(\omega_0 + \omega_{eg})t - i\phi(t)} + e^{-i(\omega_0 - \omega_{eg})t + i\phi(t))}\right) a_g(t) \tag{4.8}$$

where, $\omega_{eg} = \omega_e - \omega_g$. The Rabi frequency is defined as $\frac{\mu_{eg}E(t)}{\hbar} = \bar{\Omega}(t)$. If $\omega_0 \sim \omega_{eg}$ so that $|\omega_0 - \omega_{eg}| << |\omega_0 + \omega_{eg}|$, we can make the Rotating Wave Approximation (RWA) where we drop terms that oscillate close to $2\omega_0$. Then, for a pulse where $\phi(t) = 0$ the general solutions to these equations are,

$$a_g(t) = \cos(\int_{-\infty}^{t} \frac{\Omega(t')}{2}\, dt') \tag{4.9}$$

$$a_e(t) = i\sin(\int_{-\infty}^{t} \frac{\Omega(t')}{2}\, dt') \tag{4.10}$$

where $\Omega(t') = \sqrt{\overline{\Omega}(t')^2 + \Delta_{eg}^2}$, $\Delta_{eg} = \omega_0 - \omega_{eg}$. The excited state amplitude at all times depends on the arguments of (4.9)and (4.10). In the limit that $t \to \infty$, it is clear (in accordance with the Pulse Area Theorem) that the excited state population $|a_e(t \to \infty)|^2$ depends on the area of the pulse and is independent of pulse shape.

4.2 Multiphoton Absorption in Weak Fields

We now wish to consider more than two states in the atom and in particular an electronic structure that allows the absorption of two photons from a femtosecond pulse. Here we include an intermediate state between the ground and final state and examine two separate cases for the intermediate state: near resonance and far from resonance. Since both cases are studied experimentally in this thesis involving Rubidium and Sodium, respectively, a theoretical description of each system interacting with a femtosecond pulse is appropriate.

4.2.1 Near Resonant Intermediate State

Consider an atom with ground state $|g\rangle$, intermediate states $|m\rangle$, and excited state $|e\rangle$, shown in fig. 1.1a. If illuminated by a weak ultrafast pulse, the excited state population $a_e(t)$ can be described by second-order perturbation theory (after making the RWA) as

$$a_e(t) = -\frac{1}{4\hbar^2} \sum_m \mu_{em}\mu_{mg} \int_{-\infty}^{t} dt' \int_{-\infty}^{t'} dt'' \epsilon(t'')\epsilon(t') e^{i\Delta_{em}t'} e^{i\Delta_{mg}t''}. \tag{4.11}$$

Here, μ_{em} and μ_{mg} are the dipole matric elements, $\Delta_{em} = \omega_0 - \omega_{em}$, $\Delta_{mg} = \omega_0 - \omega_{mg}$ and the sum is performed over all intermediate states $|m\rangle$. In order to obtain the excited state population after the pulse has turned off, we must compute $|a_e(t \to \infty)|^2$.

From here we follow [12] and note that an analytic transformation of the excited state amplitude to the frequency domain is instructive in the weak field limit for several reasons. First, contributions to the excited state amplitude from frequency components exactly on resonance can be isolated from those which are not. Further, it becomes clear in the frequency domain how one can constructively and destructively interfere photon pairs across the laser bandwidth in exciting the atom from the ground state to the excited state. Later, we will see that this picture breaks down for strong fields as the energy levels shift in time and therefore the resonance condition becomes dynamic.

Making a change of variables, let $t' - t'' = \bar{t}$. Then, $t'' = t' - \bar{t}$ and, holding t' constant, $d\bar{t} = -dt''$. Then,

$$a_e = -\frac{1}{4\hbar^2} \sum_m \mu_{em}\mu_{mg} \int_{-\infty}^{\infty} dt' \int_0^{\infty} d\bar{t}\epsilon(t')\epsilon(t' - \bar{t})e^{i\Delta t'} e^{-i\Delta_{mg}\bar{t}} \tag{4.12}$$

where we have defined the two-photon detuning to be $\Delta = 2\omega_0 - \omega_{eg}$. Expressing $\epsilon(t' - \bar{t})$ by its Fourier transform, a_e becomes

$$a_e = -\frac{1}{4\hbar^2} \sum_m \mu_{em}\mu_{mg} \int_{-\infty}^{\infty} d\omega E(\omega) \int_{-\infty}^{\infty} dt'\epsilon(t')e^{-i(\omega-\Delta)t'} \int_0^{\infty} d\bar{t}e^{i(\omega-\Delta_{mg})\bar{t}}. \tag{4.13}$$

Using the fact that,

$$\int_0^{\infty} dt e^{i\omega t} = \pi\delta(\omega) + iP.V.(\frac{1}{\omega}) \tag{4.14}$$

and

$$\int_{-\infty}^{\infty} dt'\epsilon(t')e^{i(\Delta-\omega)t'} = E(\Delta - \omega) \tag{4.15}$$

we find, in agreement with [12], that

$$a_e = -\frac{1}{4\hbar^2} \sum_m \mu_{em}\mu_{mg} \left[\pi E(\Delta_{em})E(\Delta_{mg}) + iP.V. \int_{-\infty}^{\infty} d\omega \frac{E(\omega)E(\Delta - \omega)}{\omega - \Delta_{mg}}\right], \tag{4.16}$$

where P.V. denotes the Cauchy principle value operator. The first term in (4.16) contains the contributions to the excited state amplitude from those frequencies exactly matching the $|g\rangle \to |m\rangle$ and $|m\rangle \to |e\rangle$ transition. The second term contains contributions to the excited state amplitude that come from frequency pairs that still make up the $|g\rangle \to |e\rangle$ transition even though neither is on resonance itself. As one might expect for a harmonically driven system, the off-resonant second term in (4.16) is $\pi/2$ out of phase with the on-resonant term.

4.2.2 Non-resonant Intermediate State

We now wish to consider what happens when the intermediate state is far from resonance (Figure 1.1b). In this case both Δ_{gm} and Δ_{em} are much larger than the laser bandwidth $\Delta\omega$, so that $E(\Delta_{gm}) \to 0$ and $E(\Delta_{em}) \to 0$ in Eqn. 4.16. Therefore, the on-resonance contributions to the excited state amplitude in (4.16) vanish. What remains is to examine the principle value integral under the approximation of large detuning between the ground/excited state and intermediate states. If we note that $\Delta_{mg} >> \Delta\omega$ when the detuning between the ground and intermediate states is large, then $\omega - \Delta_{mg} \sim -\Delta_{mg}$. Therefore the denominator changes by little for the integral over the frequency bandwidth of the laser (i.e., where $E(\omega)$ is nonzero) and can removed from the integral with the value $-\Delta_{mg}$. Then (4.16) is approximated as

$$a_e \approx -\frac{i}{4\hbar^2} \sum_m \frac{\mu_{em}\mu_{mg}}{-\Delta_{mg}} \int_{-\infty}^{\infty} d\omega E(\omega)E(\Delta - \omega), \tag{4.17}$$

in agreement with the result of [37]. If we note that $E(\omega) = A(\omega)e^{i\phi(\omega)}$, where $\phi(\omega)$ is the spectral phase, and we let the two-photon detuning be zero ($\Delta = 0$), then the two-photon absorption probability $|a_e|^2$ is maximized for a transform limited pulse ($\phi(\omega) = 0$).

4.2.3 (2+1)Three-photon Absorption

In this section we lay out the framework for weak (perturbative) interaction between a femtosecond pulse and a three level system with both nonlinear and linear coupling between states. Shown in fig. 1.1, the ground and excited state are coupled by two photons through an off-resonant set of intermediate states $|m\rangle$. Additionally, there is a single photon transition to a resonant state $|r\rangle$. If this system is weakly coupled to a femtosecond pulse, the amplitude for state $|r\rangle$ can be described by third order time-dependent perturbation theory. Here we can use the limiting case of (4.18) to derive an expression for the amplitude to be in the resonant state $|r\rangle$ after the pulse has turned off. Making use of the Fourier convolution theorem, we can express the non-resonant two-photon absorption contributions at any time by,

$$a_e(t) = -\frac{1}{4\hbar^2} \sum_m \frac{\mu_{em}\mu_{mg}}{-\Delta_{mg}} \int_{-\infty}^{t} dt' \epsilon^2(t') e^{i\Delta t'}. \tag{4.18}$$

If we now include the single photon coupling to the resonant state $|r\rangle$, the third order expression in the Rotating Wave Approximation becomes

$$a_r(t) = \frac{1}{i\hbar^3}\mu_{re}\sum_m \frac{\mu_{em}\mu_{mg}}{-\Delta_{mg}}\int_{-\infty}^{\infty} dt' \int_{-\infty}^{t'} dt''\epsilon(t')\epsilon^2(t'')e^{i\Delta_{re}t'}e^{i\Delta t''}. \tag{4.19}$$

From here we can see that (4.19) has a similar form to (4.22), with the exception that the $|g\rangle \rightarrow |e\rangle$ transition now depends on the square of the field, as expected for a two-photon absorption. We make the same change of variables so that $t' - t'' = \bar{t}$. Then, $t'' = t' - \bar{t}$ and, holding t' constant, $d\bar{t} = -dt''$. We now note that,

$$\epsilon^2(t' - \bar{t}) = \int_{-\infty}^{\infty} d\omega \int_{-\infty}^{\infty} d\omega' E(\omega)E(\omega')e^{-i\omega(t'-\bar{t})}e^{-i\omega'(t'-\bar{t})}, \tag{4.20}$$

and find that (4.19) takes the form,

$$a_r \sim \int_{-\infty}^{\infty} d\omega \int_{-\infty}^{\infty} d\omega' E(\omega)E(\omega') \int_{-\infty}^{\infty} dt\epsilon(t')e^{i(\Delta+\Delta_{re}-[\omega+\omega'])t'} \int_0^{\infty} d\bar{t}e^{([\omega+\omega']-\Delta)\bar{t}}. \tag{4.21}$$

Performing the integral over $\bar{t}$ and expressing the integral over t' by its Fourier transform, we come to final expression for state $|r\rangle$ [13],

$$a_r = \frac{1}{i\hbar^3}\mu_{re}\sum_m \frac{\mu_{em}\mu_{mg}}{-\Delta_{mg}}\left[A^{on-res} + A^{near-res}\right] \tag{4.22}$$

$$A^{on-res} = \pi E(\Delta_{re})\int_{-\infty}^{\infty} d\omega E(\omega)E(\Delta - \omega) \tag{4.23}$$

$$A^{near-res} = i\int_{-\infty}^{\infty} d\omega E(\omega)P.V.\int_{-\infty}^{\infty} d\omega' \frac{E(\omega')E(\Delta_{re} + \Delta + [\omega + \omega'])}{[\omega + \omega'] - \Delta}. \tag{4.24}$$

The two terms in (4.22) can be identified in the following way. The first term coherently sums two-photon resonant frequency pairs between $|g\rangle$ and $|e\rangle$ with the single-photon resonant frequency between $|e\rangle$ and $|r\rangle$, indicated by the left side of fig. 1.1c. The second term contains contributions to the $|g\rangle \rightarrow |r\rangle$ transition from photon triplets that are neither single or two-photon resonant, and is indicated by the right side of fig. 1.1c. It's worth noting that A^{on-res}

has the same form as 4.18 (i.e., a non-resonant two-photon absorption), but now multiplied by the frequency component connecting $|e\rangle$ to $|r\rangle$.

4.3 Multiphoton Absorption in Strong Fields

In this section we discuss the absorption of two photons in the cases of near-resonant and non-resonant intermediate states when the exciting field is strong. Once the exciting field becomes strong, a perturbative description is no longer valid because the ground state population can become substantially depleted. Further, the energy levels of the atoms can shift as a function of time. This leads to a time-dependent detuning that causes the phase of atomic coherence to advance relative to that of the laser. Consequently, a time domain description of two photon absorption in strong fields is more appropriate.

4.3.1 Dynamic Stark Shifts from Adiabatic Elimination

Here, we give a derivation of how the electronic structure of an atom can shift in time as a result of a strong driving field, known as Dynamic Stark Shifts (DSS). The example we derive here is for a single photon absorption in a two-level atom and is extendable to more than two levels. We are particularly interested deriving a description of what happens to the electronic states when the exciting field becomes strong.

Starting with 4.8, we can integrate this equation to get

$$a_e(t) = \int_{-\infty}^{t} dt' \frac{i\mu_{eg}E(t')}{2\hbar}\left(e^{i(\omega_{eg}-\omega_0)t'+i\phi(t')} + e^{i(\omega_{eg}+\omega_0)t'-i\phi(t'))}\right) a_g(t'). \quad (4.25)$$

If the detuning between the ground and excited state is large compared to the pulse bandwidth, then $E(t)$ and $e^{i\phi(t)}$ both evolve much slower than $e^{i(\omega_{eg}-\omega_0)t}$ and $e^{i(\omega_{eg}+\omega_0)t}$ and can therefore be removed from the integral. Calculating the remaining integrals by parts, we keep the boundary terms and ignore the remaining terms because they are small. This is known as Adiabatic Elimination [58]. Thus $a_e(t)$ becomes

$$a_e(t) = \left(\frac{i\mu_{eg}\tilde{E}(t)}{2\hbar}\frac{e^{i(\omega_{eg}-\omega_0)t}}{i(\omega_{eg}-\omega_0)} + \frac{i\mu_{eg}\tilde{E}^*(t)}{2\hbar}\frac{e^{i(\omega_{eg}+\omega_0)t}}{i(\omega_{eg}+\omega_0)}\right) a_g(t), \quad (4.26)$$

where $\tilde{E}(t) = E(t)e^{i\phi(t)}$. Substituting 4.26 into 4.7, we drop terms that evolve at $E(t)^2e^{\pm i2\omega_0 t}$ because $E(t)$ changes slowly compared to $e^{\pm i2\omega_0 t}$. Then $\dot{a_g}(t)$

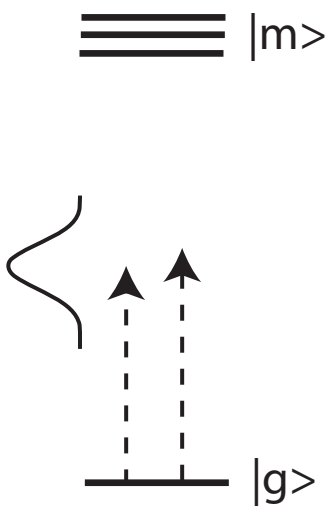

Figure 4.1: Electronic Levels for Adiabatic Elimination (laser bandwidth shown at the left). Single-photon absorption between a ground state $|g\rangle$ and a manifold of far off-resonant excited states $|m\rangle$

.

becomes

$$\dot{a}_g(t) = \frac{i\mu_{eg}^2|\tilde{E}(t)|^2}{(2\hbar)^2}\left(\frac{2\omega_{eg}}{\omega_{eg}^2-\omega_0^2}\right)a_g(t). \tag{4.27}$$

We can now define the Dynamic Stark Shift (DSS) to be,

$$\omega_g^s(t) = \frac{\mu_{eg}^2|\tilde{E}(t)|^2}{2(\hbar)^2}\frac{\omega_{eg}}{\omega_{eg}^2-\omega_0^2} = \omega_g^s|\tilde{E}(t)|^2. \tag{4.28}$$

The DSS is interpreted as the time-dependent shift of an energy level due to coupling to another level with a strong field. Further, if the ground state is coupled to a manifold of dipole allowed states far from resonance($|m\rangle$), then the expression for the DSS becomes

$$\omega_g^{(s)}(t) = \sum_m \frac{\mu_{mg}^2|\tilde{E}(t)|^2}{2(\hbar)^2}\frac{\omega_{mg}}{\omega_{mg}^2-\omega_0^2}. \tag{4.29}$$

In the case of a two-photon absorption through a manifold of far off-resonant intermediate states (see Figure 1.1(b)), adiabatic elimination of the off-resonance

states can also be performed [59]. In this case, the DSS becomes

$$\omega^{(s)}_{\{e,g\}}(t) = \sum_m \frac{\mu^2_{\{e,g\}m}|\tilde{E}(t)|^2}{2(\hbar)^2}\frac{\omega_{m\{e,g\}}}{\omega^2_{m\{e,g\}} - \omega_0^2}. \tag{4.30}$$

4.3.2 Near Resonant Intermediate State

With an understanding of how the dynamic Stark shift can change energy levels in time due to other far off-resonant states, we can now formally describe two-photon absorbing atoms where the intermediate states are near resonance and the exciting field is strong. First consider the ground state $|g\rangle$ and ask which other dipole allowed states are far from resonance. If we adiabatically eliminate those off-resonant state in the same way for arriving at Eq. 4.29, we can calculate the DSS for ground state $\omega^s_g(t)$. Likewise, we can adiabatically eliminate the off-resonant states for the intermediate $|m\rangle$ and excited states $|e\rangle$ and also calculate the DSS $\omega^s_m(t)$ and $\omega^s_e(t)$ for $|m\rangle$ and $|e\rangle$, respectively. Since the DSS describes the time-dependent shift of the energy levels, they end up as diagonal entries in the Hamiltonian. The Hamiltonian in the interaction representation then becomes (after applying the RWA)

$$\hat{\mathbf{H}}(t) = \begin{pmatrix} \omega^{(s)}_g(t) & \chi_{gm}(t)e^{i(\Delta_{gm}t-\phi(t))} & 0 \\ \chi^*_{gm}(t)e^{-i(\Delta_{gm}t-\phi(t))} & \omega^{(s)}_m(t) & \chi_{me}(t)e^{i(\Delta_{me}t-\phi(t))} \\ 0 & \chi^*_{me}(t)e^{-i(\Delta_{me}t-\phi(t))} & \omega^{(s)}_e(t) \end{pmatrix}, \tag{4.31}$$

where $\omega^{(s)}_g(t)$, $\omega^{(s)}_m(t)$, and $\omega^{(s)}_e(t)$ represent the Dynamic Stark Shifts of the ground, intermediate, and excited stats of the atom, respectively, and are calculated the same as Eq. 4.29 and as in [60]. Here Δ_{gm} and Δ_{me} represent the detuning between the ground to intermediate and intermediate to excited state transitions, respectively, $\chi_{gm}(t)$ and $\chi_{me}(t)$ represent the single photon Rabi frequencies give by $\chi_{gm}(t) = E(t)\mu_{gm}/\hbar$ and $\chi_{me}(t) = E(t)\mu_{me}/\hbar$.

It is instructive to transform this Hamiltonian into a form that has only off-diagonal elements at each instant of time. Finding the appropriate unitary transformation matrix and carrying out the necessary matrix multiplication and addition (see appendix A) we can express the transformed Hamiltonian as,

$$\hat{\mathbf{H}}(t) = \begin{pmatrix} 0 & \chi_{gm}(t)e^{i\alpha_{gm}(t)} & 0 \\ \chi^*_{gm}(t)e^{-i\alpha_{gm}(t)} & 0 & \chi_{me}(t)e^{i\alpha_{me}(t)} \\ 0 & \chi^*_{me}(t)e^{-i\alpha_{me}(t)} & 0 \end{pmatrix}, \tag{4.32}$$

where

$$\alpha_{gm}(t) = \int_{-\infty}^{t} dt' \delta^{s}_{mg}(t') + \Delta_{mg} t + \phi(t) \tag{4.33}$$

and

$$\alpha_{me}(t) = \int_{-\infty}^{t} dt' \delta^{s}_{em}(t') + \Delta_{em} t + \phi(t) \tag{4.34}$$

represent the relative phases between the atom and the pulse (called the atom-field phase) for the corresponding transitions. The atom-field phase represents the phase advance of the $|g\rangle \rightarrow |m\rangle$ and $|m\rangle \rightarrow |e\rangle$ coherence relative to the phase of the laser field. Here, $\delta^{(s)}_{ij}(t) = \omega^{(s)}_{i}(t) - \omega^{(s)}_{j}(t)$ and is defined as the differential Stark shift. The above will be used later to describe experiments involving two-photon absorption in Rubidium where absorption from the 5S state to 5D state is resonantly enhanced by the $5P_{1/2}$ and $5P_{3/2}$ states.

4.3.3 Non-resonant Intermediate State

As before, we are interested in two-photon transitions where the states mediating the two-photon absorption are far from resonance, so that $\Delta\omega << \Delta_{mg}$. This was studied in considerable detail as part of the thesis work of Carlos Trallero-Herrero [27], and here we highlight the main results.

Again, referring to Fig. 1.1(b) the intermediate states $|m\rangle$ can be removed by Adiabatic Elimination [59]. For the case of a non-resonant two-photon absorption in the limit of a strong field, Carlos Trallero-Herrero found that the Hamiltonian for a strong field two-photon absorption could be written as,

$$\hat{\mathbf{H}}(t) = \begin{pmatrix} \omega^{(s)}_{g}(t) & \chi^{*}(t) e^{i(\Delta t - \varphi(t))} \\ \chi(t) e^{-i(\Delta t - \varphi(t))} & \omega^{(s)}_{e}(t) \end{pmatrix}, \tag{4.35}$$

where here $\chi(t)$ is the effective two-photon Rabi frequency given by,

$$\chi(t) = -\sum \frac{\mu_{em}\mu_{mg}}{(2\hbar)^2} \frac{\epsilon^2(t)}{\omega_{mg} - \omega_0} = \chi_0 \epsilon^2(t) \tag{4.36}$$

and $\omega^{(s)}_{e,g}(t)$ is given by Eqn. 4.30.

Further insight was gained [27, 61] by rotating the Hamiltonian in Eqn. 4.35 to a frame that removes the diagonal elements. Performing a unitary transformation to the rotating frame (see appendix A) we find that the Hamil-

tonian becomes,

$$\hat{\mathbf{H}}(t) = \begin{pmatrix} 0 & \chi^*(t)e^{i\alpha(t)} \\ \chi(t)e^{-i\alpha(t)} & 0 \end{pmatrix}, \tag{4.37}$$

where

$$\alpha(t) = \int_{-\infty}^{t} dt' \delta_{\omega}^{(s)}(t') + \Delta t + \phi(t) \tag{4.38}$$

is the atom-field phase. Here, $\Delta = 2\omega_0 - \omega_{eg}$ represents the two-photon detuning, $\delta_{\omega}^{(s)}(t) = \omega_e^{(s)}(t) - \omega_g^{(s)}(t)$ represent the differential Stark shift, and $\phi(t)$ is the time-dependent phase of the electric field. In this case, the $|g\rangle \rightarrow |e\rangle$ transition can proceed efficiently if one makes $\alpha(t)$ a slowly varying function of time. In Eqn. 4.37, the strong-field two-photon version of the pi pulse condition [38]is evident,

$$\int_{-\infty}^{\infty} dt \chi(t) e^{i\alpha(t)} = \frac{\pi}{2}. \tag{4.39}$$

From 4.39, it is clear the integral is maximal when $\alpha(t)$ varies slowly in time and therefore the population of the excited state is maximal.

4.3.4 (2+1)Three-photon Absorption

In the last section of this chapter, we formally focus on one of the main systems emphasized in this thesis - a (2+1) three-photon absorbing atom excited by a strong femtosecond pulse (see Figure 1.1(c)). Deriving the Hamiltonian of this system amounts to taking the result of Eq. 4.35 and extending it to include another a single-photon absorption to a dipole-allowed state. In doing so, we can express the time-dependent atom-field Hamiltonian as:

$$\hat{\mathbf{H}}(t) = \begin{pmatrix} \omega_g^{(s)}(t) & \chi^*(t)e^{i(\Delta t - \phi(t))} & 0 \\ \chi(t)e^{-i(\Delta t - \phi(t))} & \omega_e^{(s)}(t) & \chi_{er}^*(t)e^{-i[\phi(t)/2 - \Delta_{er}t]} \\ 0 & \chi_{er}(t)e^{i[\phi(t)/2 - \Delta_{er}t]} & \omega_r^{(s)}(t) \end{pmatrix}. \tag{4.40}$$

Here, $\phi(t)$ is field phase, $\Delta = 2\omega_0 - \omega_{eg}$ is the two-photon $|g\rangle \rightarrow |e\rangle$ atom-field detuning, $\omega_g^{(s)}(t)$, $\omega_e^{(s)}(t)$, and $\omega_r^{(s)}(t)$ represent the time-varying dynamic Stark shift of the ground $|g\rangle$, excited $|e\rangle$, and resonant $|r\rangle$ states, respectively, $\chi(t)$ represents the two-photon Rabi frequency, μ_{re} and Δ_{er} are the one-photon coupling between the excited and resonant states and corresponding detuning, $\varepsilon(t)$ is the electric field, and $\chi_{er}(t) = \frac{\mu_{re}}{2\hbar}\varepsilon(t)$. Here, the DSS of the resonant state $|r\rangle$ is again calculated according to Eq. 4.29 and [59].

Chapter 5

Strong Field Control of a Three Level System

5.1 Introduction

In this chapter, we concentrate on strong field population transfer in a three-level system with multiphoton coupling between states. An important aspect of coherent control is selectively populating a particular target state with high efficiency. Many techniques have been developed which make use of strong-field coupling to atomic or molecular states via single photon (dipole allowed) transitions. These include Adiabatic Rapid Passage (ARP) and variants - Chirped Adiabatic Rapid Passage (CARP)[15, 16], piecewise Adiabatic Rapid Passage [17], and Stimulated Raman Adiabatic Passage (STIRAP)[22]. These approaches are powerful and effective and there is interest in extending them to multi-photon coupling between atomic and molecular levels [7, 23–26]. In order to achieve efficient population transfer beyond the limits of single-photon excitation, one has to take into consideration multiple interfering pathways and dynamic Stark shifts, which make resonance conditions time-dependent and modify the phase advance of the bare states during the atom/molecule-field interaction. A dramatic example of this is the transition from stimulated absorption to stimulated emission well before half a Rabi cycle is complete in strong-field two-photon absorption [38, 60]. It is precisely these phase modulations of the bare states that ARP techniques are very sensitive to [24].

For complex systems excited by strong fields, it is often difficult to design optimal pulse shapes for control, and closed-loop experiments are carried out to discover effective pulses. While closed-loop experiments are often capable of finding pulses which lead to improvements in the population of a target state, interpreting the control dynamics is often challenging. Here, we demonstrate

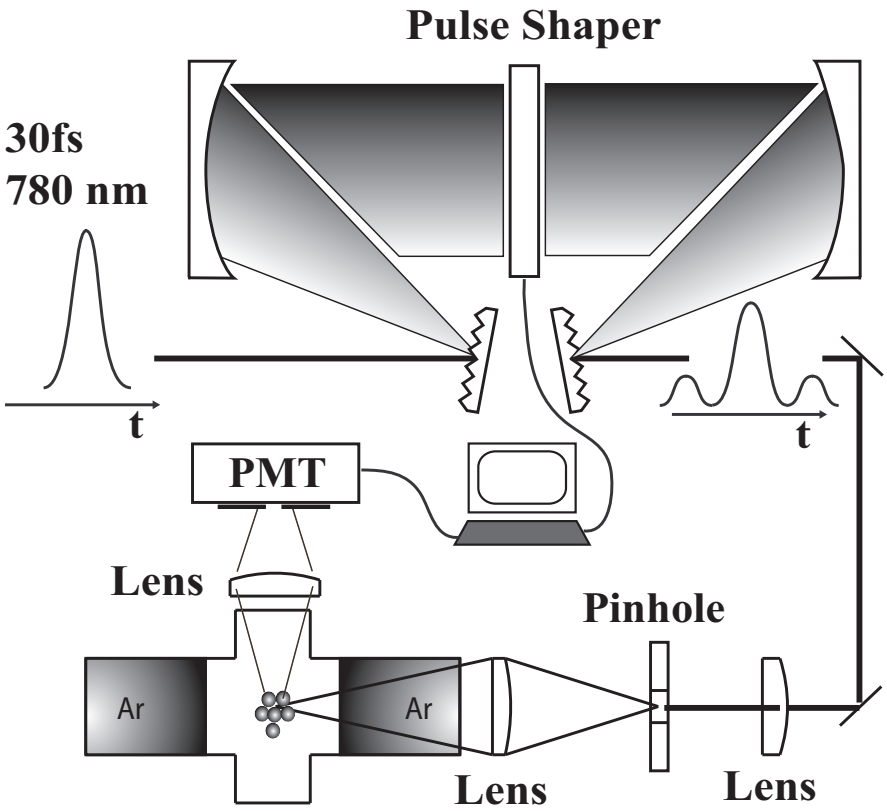

Figure 5.1: Experimental diagram showing the laser system, spatial filter (pinhole) with imaging system, heat pipe oven, photomultiplier tube (PMT) with entrance iris, and computer used in the feedback loop.

and interpret a population inversion using three-photon absorption from a single intense ultrafast laser pulse shaped in a closed-loop learning control experiment. Our experiments are performed with atomic sodium, where three-photon absorption to the 7p state from the 3s ground state is possible at 778 nm, with a two-photon resonant enhancement at 777 nm provided by the 4s state. Figure 5.4 illustrates the relevant atomic levels. Previous work on alkali atoms has looked at perturbative two and three-photon absorption [11, 13, 62], non-perturbative two-photon absorption [23, 38], as well as multi-photon ionization [63]. Adiabatic elimination of the off-resonant states in the system allows for a quantitative description in terms of a three-level Hamiltonian [64].

5.2 The Strong Field Limit

As mentioned in Chapter 2, both fluorescence and superfluorescence (SF) were collected from the excited atoms. Fluorescence from the center of the heat pipe is collected at 90^o with respect to the beam propagation direction with an f2 (focal length is twice the diameter) lens and imaged onto a photomultiplier tube (PMT), as illustrated in Fig. 5.1a. Interference filters were used to isolate specific transitions (e.g. $3p - 3s$). In order to avoid collecting fluorescence from atoms exposed to different laser intensities in the focal region, the beam is focused onto a diamond pinhole prior to the heat pipe oven. We produce a laser focus with minimal intensity variation by imaging the spatially filtered focus into the sample chamber. Figure 2.7 shows the measured transverse spatial profile of the intensity at the image plane of the heat pipe oven with and without the pinhole present. We avoid collecting fluorescence from atoms exposed to different intensities along the longitudinal axis by placing a small ($\approx$ 1mm) aperture in front of the PMT. These adjustments allow us to measure the dependence of fluorescence yield vs pulse shape, which otherwise would be masked by spatial intensity averaging, an example of which is given in [64].

5.3 Measuring the Excited State Population

Figure 5.3 shows the energy levels of sodium that contribute to the measurement of the $4s$ and $7p$ populations. The dashed lines indicate the three (2+1) photon absorption process and the solid lines show transitions that we measure with our PMT. Fluorescence decay from the 7p state is complicated by the face that the excited atoms undergo collisions with Argon atoms in the oven. Here we lay out a basic description of how atoms initially excited to the $7p$ state undergo inelastic l-mixing collisions with argon atoms in the heat pipe oven. While there has been considerable theoretical work on related collisional phenomena such as [65], we have not found predictions for the specific conditions and states of our experiment. Collisional transfer effects after excitation of Na d and s Rydberg states were studied experimentally [66, 67], and transfer from the $6p$ state was investigated in [68], where it is reported that l-changing collisions between nearly degenerate levels have a much larger cross-section than $p - d$ transfer, for which the energy mismatch is larger.

Our experimental measurements indicate that atoms initially excited to the $7p$ state by our laser undergo rapid collisional transfer to neighboring states, eventually populating an array of states from the $6s$ to the $7p$ in energy (see the upper half of Fig. 5.4) before spontaneous decay takes place. At the Na and Ar densities used in our experiments, these collisions take place in 10s to 100s

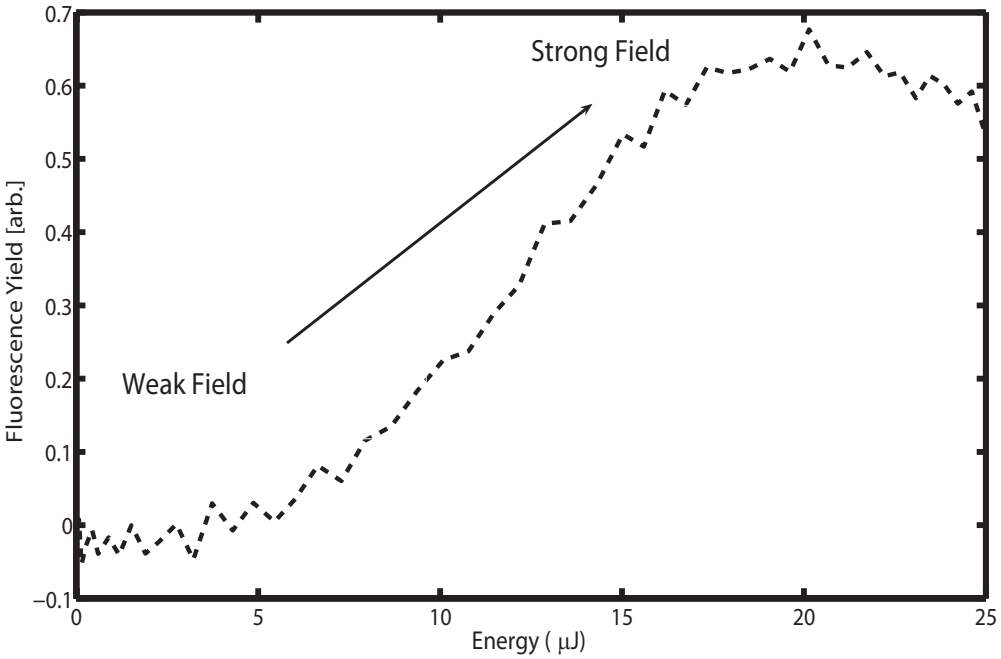

Figure 5.2: 7p fluorescence yield as a function of pulse energy for an unshaped pulse. The transition to a non-perbative response is evident by a roll-over of the 7p signal. In the weak field limit, one expects the fluorescence yield to behave quadratically with pulse energy.

of ps, while spontaneous emission takes 10s to 100s of ns. For states below the $6s$, the energy difference between states is sufficiently large that collisions are no longer efficient in populating them. Thus, states below the $5p$ are populated via spontaneous emission. All transition to the 3p state starting from states above the $5p$ show detector-limited rise times (<4ns), which is consistent with those states being collisionally populated. Fluorescence signals originating below the $5p$ have significant risetimes greater than 10 ns, as illustrated in Fig. 5.5(b). Figure 5.4 shows the states mainly populated by collisions with argon atoms.

Based on this picture of collisional and fluorescence decay, we used the measured fluorescence from the $7s-3p$, $6d-3p$, $4d-3p$, $6s-3p$, and $5s-3p$ transitions to determine the initial population in the $7p$ state immediately after the shaped pulse. Comparing this fluorescence with fluorescence on the $3p-3s$ line allowed us to determine the fraction of excited atoms which were excited to the $7p$ state vs the $4s$ state (two photon resonant at 777 nm). What remains is to simply know what fraction of the atoms are excited out of the ground state (i.e., out of the 3s state and into the 4s or 7p). Measurements

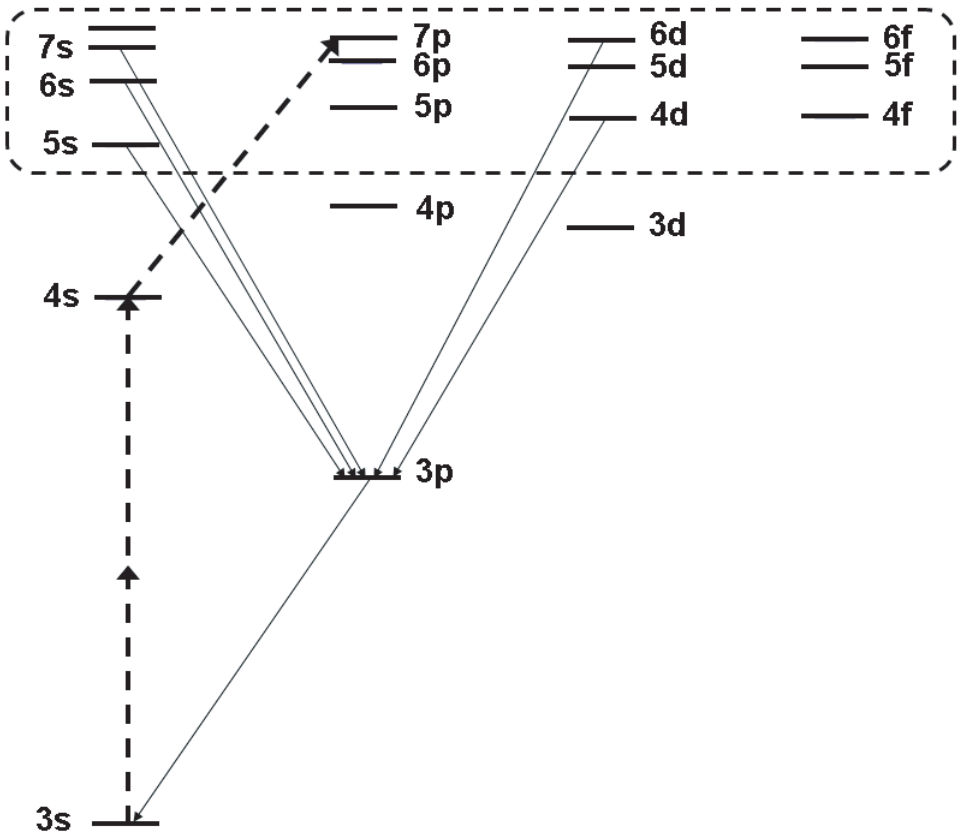

Figure 5.3: The dashed lines indicate the three (2+1) photon absorption process. The solid lines include transitions measured by the PMT. The dashed box shows a region which is enlarged in Fig. 5.4 to show which states are populated by collisions.

Table 5.1: Table of fluorescence lines we measure in the Sodium atom. For each line we list the transition wavelength, quantum efficiency of the PMT, efficiency of the interference filter, filter part number, and the width of the interference filter.

	7s	6d	5d	3p	4d	5s	6s
Wavelength [nm]	475	467	498	589	569	615	515
Quantum Efficiency	0.0875	0.091	0.07	0.013	0.02	0.01	0.058
Filter Transmission	0.17	0.46	0.78	0.56	0.52	0.19	0.28
Filter Thorlabs (FB)	470-10	470-10	500-40	590-10	570-10	610-10	510-10
Filter Width [nm]	10	10	40	10	10	10	10

of superfluorescence (SF) on the $3p - 3s$ transition for a pulse that excites the $4s$ state allowed us to determine the fraction of atoms excited above the ground state ($4s$ and $7p$), since earlier work demonstrated a sharp threshold in the $4s$ state population (0.66) is needed for superfluorescence to occur at high densities [30].

Combining these two measurements allowed us to determine the population of the $7p$ state after the atoms interacted with the shaped laser pulse (but before inelastic collisions) without having to rely on knowledge of the density of atoms in the focus, the solid angle subtended by the detector or our absolute detection efficiency. We note that this calculation yields a lower bound for the population in the $7p$ state because the superfluorescence threshold may be higher than 0.66 for sodium vapor at 270^{o}C. This follows from the fact that coherent emission is based on an achieved population inversion and density of the gain medium. If the gain medium has a smaller density (as you would expect for a lower temperature of the Sodium vapor) the required population inversion would be higher for the build up of coherent emission.

5.4 Control results

In order to discover an optimal pulse shape for populating the 7p state, we used the $7s - 3p$ and $6d - 3p$ fluorescence lines [57] as a feedback signal for our GA. The fluorescence for a shaped and unshaped pulse is shown in Fig.5.5(a) and illustrates the order of magnitude fluorescence enhancement achieved by our GA. Fitness (integrated fluorescence yield) as a function of GA generation

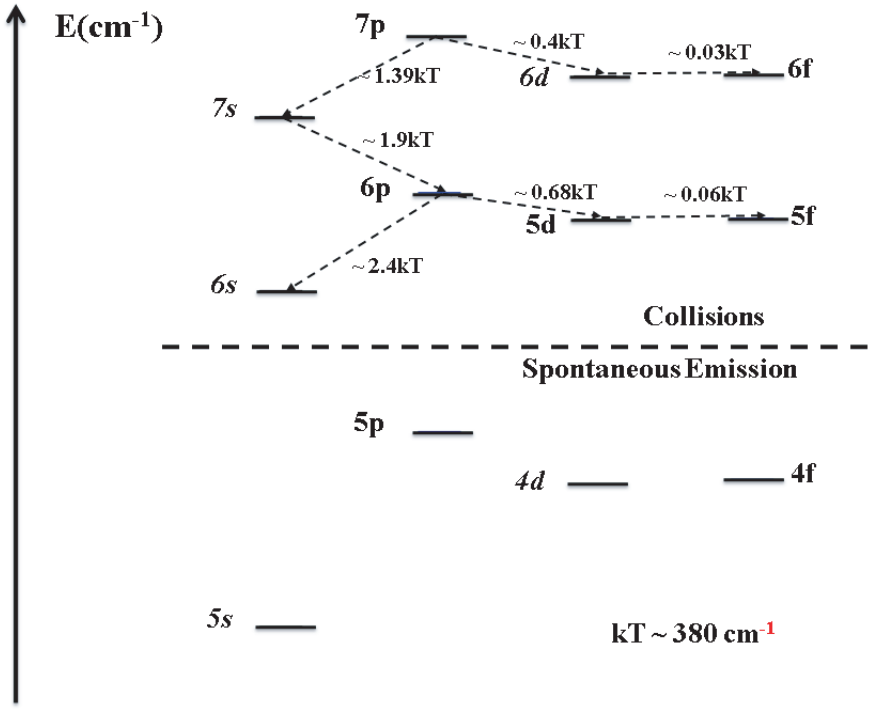

Figure 5.4: Grotrian diagram indicating which states are populated via collisions from the 7p state. This figure is an enlargement of the dashed box region in 5.3. The dashed line separates the states primarily populated by collisions from those populated by spontaneous emission. States we measure fluorescence from are labelled with italics.

is shown in the inset of Fig.5.5(a). Table 5.2 summarizes our measurements of the $7p$ population for an optimized laser pulse. The numbers were calculated in the following manner. We first measured fluorescence for the $7s-3p$, $6d-3p$, $4d-3p$, $6s-3p$, and $5s-3p$ transitions and used the integrated fluorescence in conjunction with branching ratios to calculate the number of atoms initially in the 7s, 6d, 6f, 6s and 5s states (collisionally populated after the atom-laser interaction). All the transitions could be isolated with interference filters except the $7s-3p$ and $6d-3p$, which were collected with a single filter and then fitted with the known lifetimes [69] to extract independent contributions. We explicitly looked for evidence of ionization by checking for decays from states that would be populated by recombination. Based on our measurements, we estimate that less than 1% of the fluorescence signal on the transitions listed above was due to ionized atoms.

Our goal was to establish a population inversion ($|\Psi_{7p}|^2$ ¿ 0.5) by an optimally shaped pulse and this relied on two key measurements: spontaneous emission from excited states of the atom and stimulated emission (superfluorescence) from one of its ground to excited state transitions. One important aspect of our measurements is that by always measuring the ratio of fluorescence, we sidestep uncertainties associated with collection efficiency like transmission through glass, solid angle subtended by the lens used to collect fluorescence, and the number of atoms in the laser focus. The collection efficiencies to worry about are quantum efficiency of the PMT, efficiency of the interference filters used to isolate fluorescence, and radiation trapping.

The number of atoms decaying from the collisionally populated states (after the shaped pulse populated the 7p excited state) were summed to give a lower bound for the initial number of atoms in the 7p state per unit detection efficiency. The total number of atoms excited per unit detection efficiency was calculated from the integrated $3p-3s$ fluorescence after correcting for radiation trapping (discussed below). The ratio of the two quantities (the number of atoms excited to the 7p state per unit detection efficiency divided by the number of atoms excited per unit detection efficiency) yielded the fraction of excited atoms which were in the 7p state ($|\Psi_{7p}|^2/(|\Psi_{4s}|^2+|\Psi_{7p}|^2)$ in table 5.2). What remains is to calculate the fraction of atoms excited out of the ground state ($|\Psi_{4s}|^2+|\Psi_{7p}|^2$ in table 5.2). In order to calculate the fraction of atoms excited out of the ground state, we measured $3p-3s$ fluorescence as a function of superfluorescence (SF) from the $3p-3s$ transition. Thus, by noting the $3p-3s$ fluorescence at the SF threshold (for which earlier work has established an initial 4s population of 0.66 [30]), we could determine the population of the 4s state for a given fluorescence signal. We note that the oscillator strength of the $7p-3s$ transition (roughly two orders of magnitude

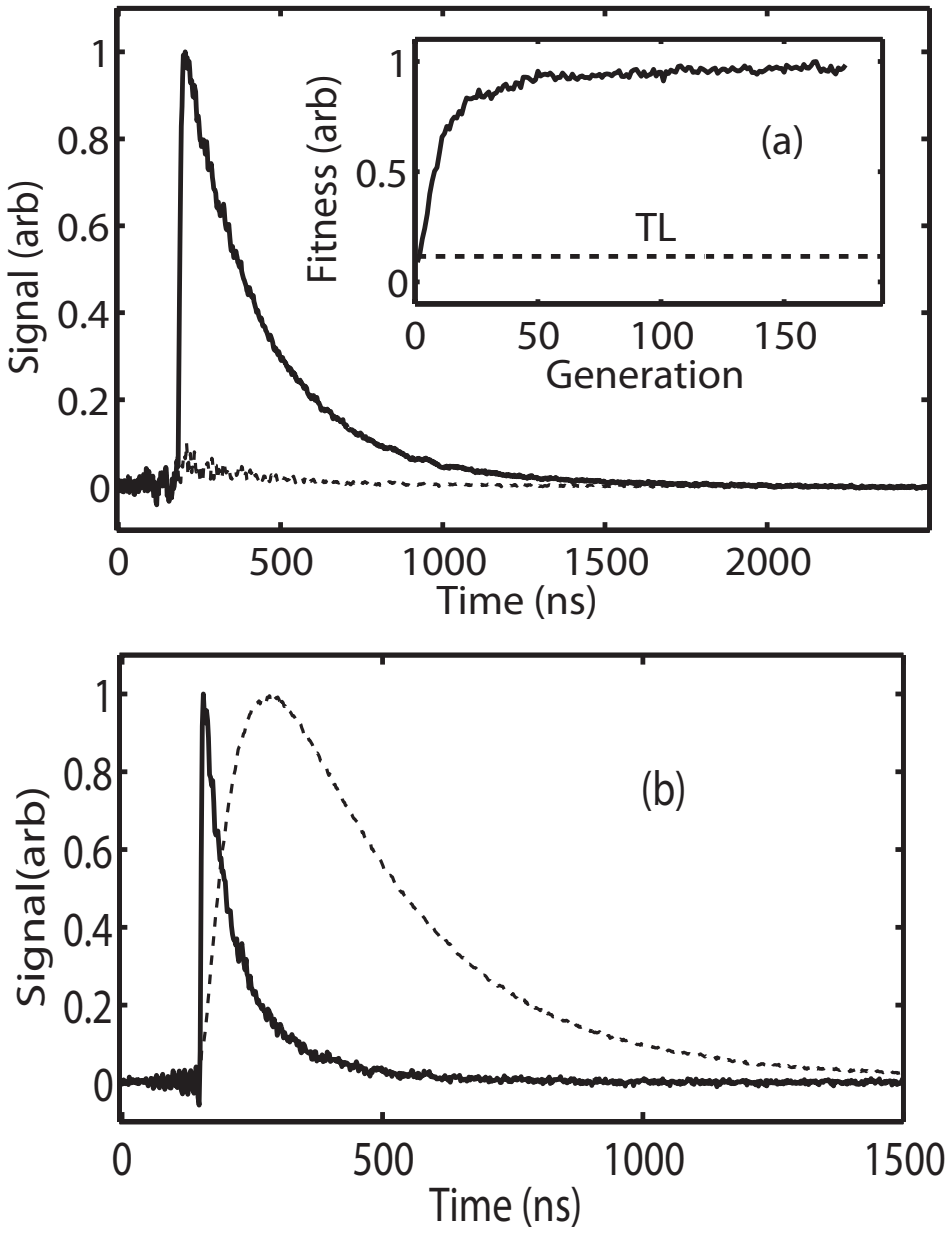

Figure 5.5: (a) The solid curve is a fluorescence measurement (including light from the $7s-3p$ and $6d-3p$ transitions) for a GA optimized pulse; the dashed curve is for an unshaped pulse. The inset is fitness (integrated fluorescence yield) as a function of generation. The dashed line indicates the fitness of a transform-limited (unshaped) pulse. (b) The solid curve is $6s-3p$ fluorescence and the dashed curve is $4d-3p$ fluorescence; both curves are normalized and correspond to a GA optimized pulse.

Table 5.2: Measured fraction of excited atoms, fraction of atoms in the 7p state, and 7p population with corresponding standard deviation (STD). The values represent an average of 5 different GA trials at a fixed temperature of 270^{o}C and central wavelength of 778 nm.

	$\lvert\Psi_{4s}\rvert^2 + \lvert\Psi_{7p}\rvert^2$	$\lvert\Psi_{7p}\rvert^2/(\lvert\Psi_{4s}\rvert^2 + \lvert\Psi_{7p}\rvert^2)$	$\lvert\Psi_{7p}\rvert^2$
Value	0.69	0.89	0.61
STD	0.09	0.08	0.09

lower than the $3p - 3s$) makes stimulated emission on this transition difficult to measure at the densities used in our experiments.

As the mode imaged from the diamond pinhole into the heat pipe is not perfect, there is some intensity variation across the transverse spatial profile. Therefore, the population of the $4s$ state is not uniformly 0.66 across the spatial profile of the laser and we correct for this by calculating the average population across the measured mode profile for a peak population at SF threshold of 0.66. We calculate the population of the $4s$ state averaged over the transverse spatial profile of the mode to be ≈ 0.49 when SF is observed. Taking the ratio of an integrated PMT trace at 589 nm for a 7p optimized pulse to an integrated PMT trace at 589 nm for an unshaped pulse at SF threshold and multiplying by the average 4s population gives the fraction of excited atoms. We note that this approach yields a conservative value for the average $7p$ population, with the peak population at the center of the beam being significantly higher. Finally, computing the ratio of light measured from the collisionally populated states to light from the 3p states and multiplying by the fraction of excited atoms (also accounting for transitions to the ground state that don't go through the 3p state) we arrive at the final population in the 7p state of 0.61

5.5 Radiation trapping

Since $3p-3s$ fluorescence is resonant with excitation of the ground state, a significant portion of the radiation is absorbed and re-emitted (radiation trapping [70]) such that it is not imaged onto our PMT. In order to correct for the light not detected due to radiation trapping, we measured the $3p - 3s$ fluorescence as a function of temperature from 270^{o}C to 147^{o}C, corresponding to densities from 8.3×10^{19} atoms/m^3 to 1.3×10^{17} atoms/m^3. At low temperatures (and

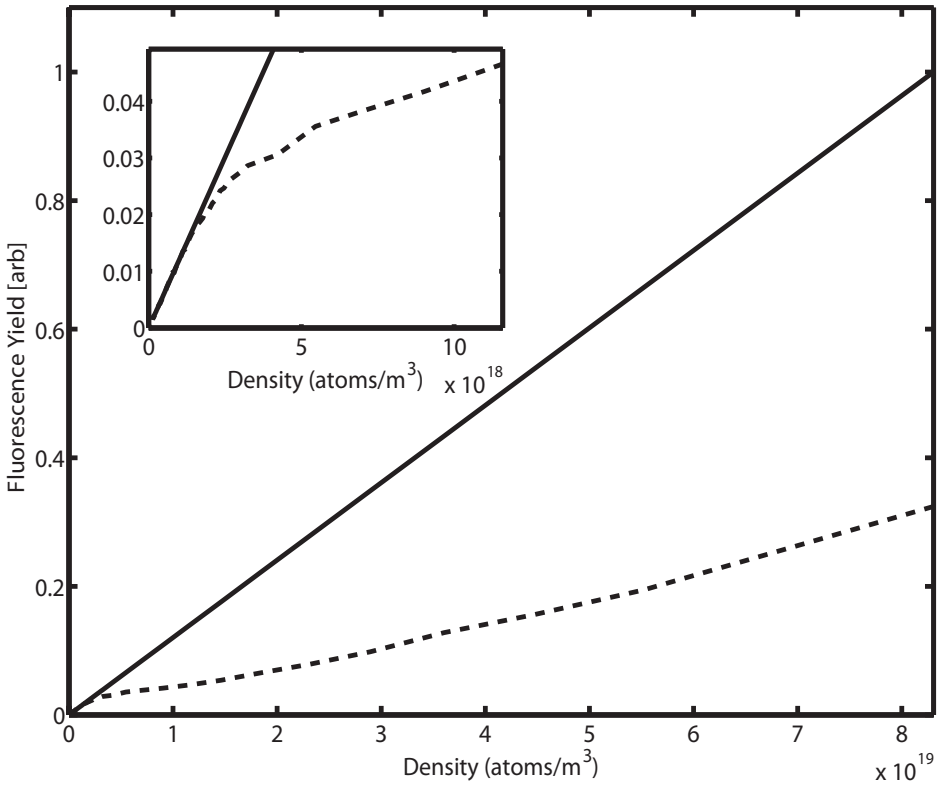

Figure 5.6: Dashed line is measured fluorescence yield vs sodium density and the solid line is a fit in the linear region. The inset is zoomed to highlight the region where fluorescence yield (arbitrary units) varies linearly with density.

densities) where radiation trapping is negligible, the integrated fluorescence is a linear function of density. However, the relationship between integrated fluorescence and density deviates from linearity as the density increases. We derived a correction factor for the measured $3p-3s$ light by first extrapolating the linear dependence of fluorescence with density to high densities and then taking the ratio of the linear extrapolation with the measured fluorescence. The linear fit of fluorescence yield vs density gave a correction factor of ≈ 3 for light collected at 270^oC, corresponding to the temperature of the experiment. Figure 5.6 illustrates the measurements of $3p-3s$ fluorescence as a function of density along with our linear fit for low densities. We note that while the atomic gas is optically dense for the $3p-3s$ fluorescence radiation, the drive laser pulse at ≈ 780nm is not attenuated as it propagates through the sample and measurements of the pulse shape at the heatpipe exit are similar to those at the entrance.

5.6 Interpreting the Control

A key aspect of the experiment is understanding the dynamics underlying the efficient population transfer driven by the shaped laser pulse. As a starting point for the interpretation, we constructed Wigner distributions for our measured (SHG FROG) optimal pulses [71], where the Wigner distribution is given as

$$w(t,\omega) = \frac{1}{\pi}\int_{-\infty}^{\infty} d\omega' E^*(\omega + \frac{\omega'}{2})E(\omega + \frac{\omega'}{2})e^{-i\omega' t}, \tag{5.1}$$

and $E(\omega)$ is the electric field in the frequency domain [71]. The Wigner function is a quasi probability distribution (not positive definite) and shows how the instantaneous frequency varies with time. Typical Wigner distributions for two different optimal pulses are shown in Fig. 5.7. The optimal pulses found by the GA showed varying temporal structure, but many in the experimental trials showed clear indications of a negative linear chirp, such as the pulses shown in Fig. 5.7. This motivated the experimental and numerical study of population transfer as a function of linear chirp or quadratic spectral phase. Therefore, we numerically integrated the Schrödinger equation and measured the fluorescence yield as functions of pulse intensity and chirp. Working in the rotating wave approximation and adiabatically eliminating nonresonant atomic levels, as discussed in chapter 4, we can express the time-dependent atom-field Hamiltonian as:

$$\hat{\mathbf{H}}(t) = \begin{pmatrix} \omega_g^{(s)}(t) & \chi^*(t)e^{i(\Delta t-\varphi(t))} & 0 \\ \chi(t)e^{-i(\Delta t-\varphi(t))} & \omega_e^{(s)}(t) & \chi_{er}^*(t)e^{-i[\varphi(t)/2-\Delta_{er}t]} \\ 0 & \chi_{er}(t)e^{i[\varphi(t)/2-\Delta_{er}t]} & \omega_r^{(s)}(t) \end{pmatrix}. \tag{5.2}$$

Here, $\varphi(t)$ is field phase, $\Delta = 2\omega_0 - \omega_{eg}$ is the two-photon $3s-4s$ atom-field detuning, $\omega_g^{(s)}(t)$, $\omega_e^{(s)}(t)$, and $\omega_r^{(s)}(t)$ represent the time-varying dynamic Stark shift of the $3s$, $4s$, and $7p$ states, respectively, $\chi(t)$ represents the two-photon Rabi frequency, μ_{re} and Δ_{er} are the one-photon coupling between the (4s) and (7p) states and corresponding detuning, $\varepsilon(t)$ is the electric field, and $\chi_{er}(t) = \frac{\mu_{re}}{2\hbar}\varepsilon(t)$.

The numerical results shown in Fig. 5.8(b) agree with the measurements in Fig. 5.8(a). Here, U_0 is the minimum pulse energy for an inversion on the $3s-4s$ transition, which corresponds to $\approx 12\mu$J with a uniform intensity profile in our focal geometry. We note that a significant increase in population transfer is observed for negative chirp, while positive values yield very little transfer. The intuitive ordering of frequencies in the pulse, where first the

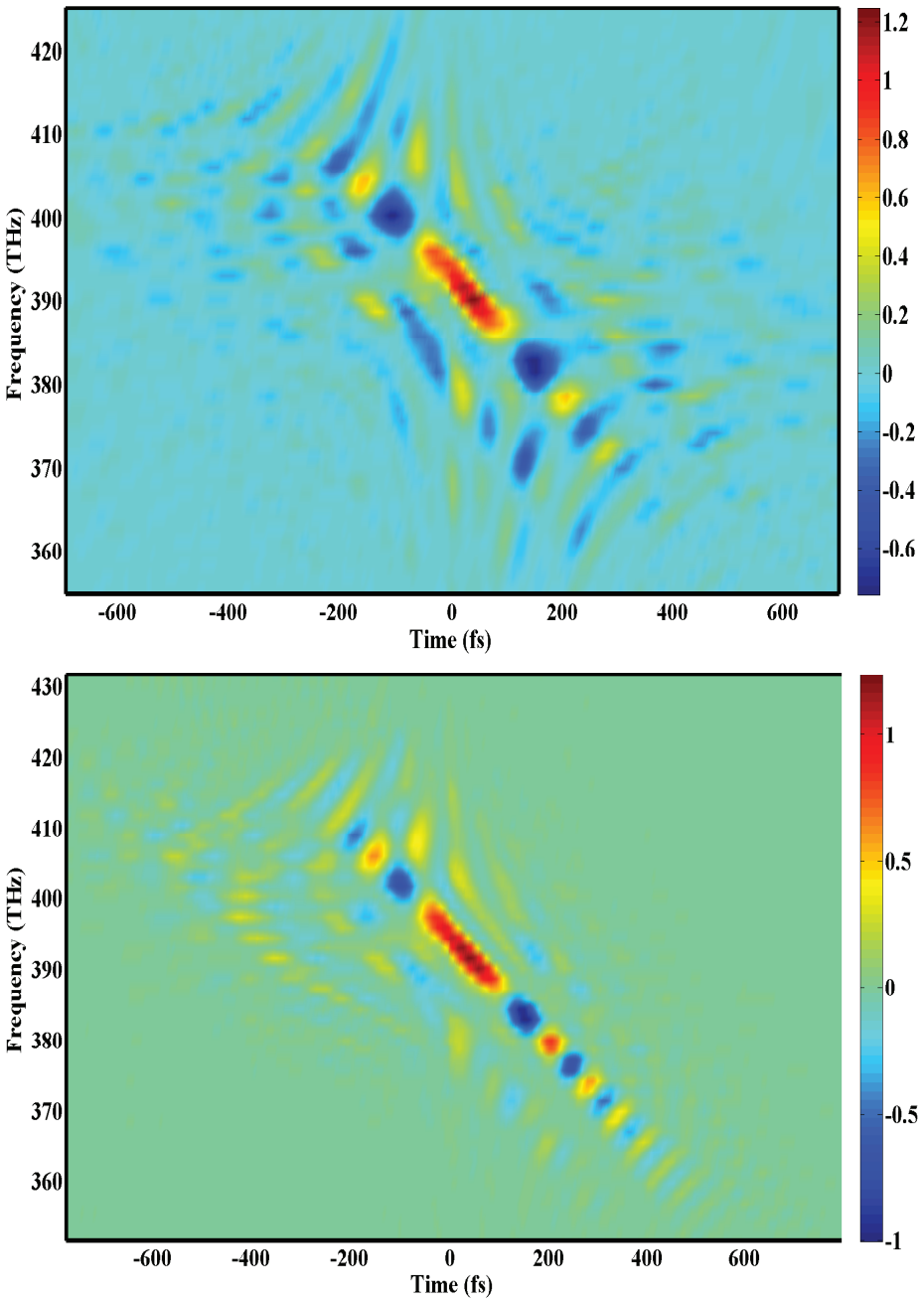

Figure 5.7: Wigner distributions for two pulses optimized by the GA for 7p population transfer. The central wavelength of the pulses corresponds to λ_0 = 783 nm.

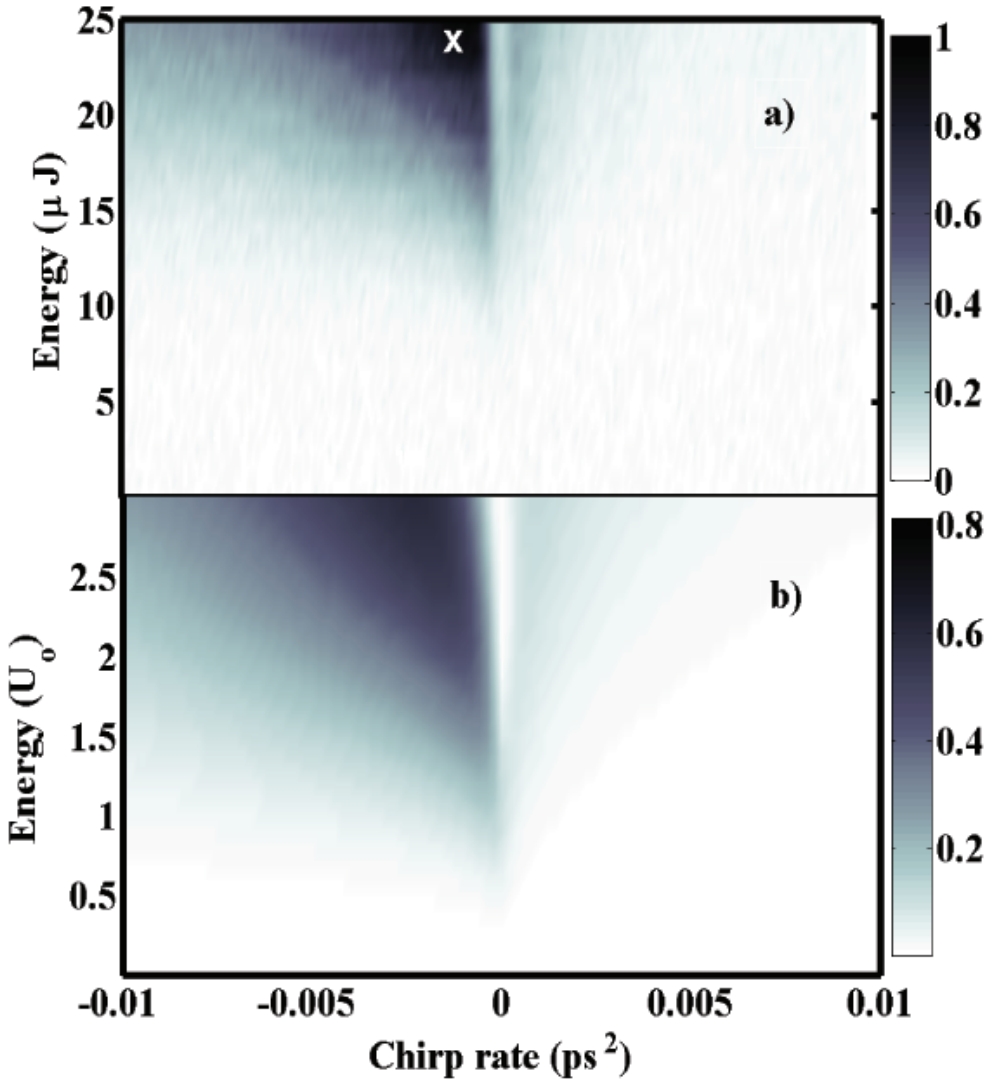

Figure 5.8: Calculated and measured population transfer to the 7p state as a function of energy and chirp a) Measurement of $7s - 3p$ and $6d - 3p$ fluorescence as a function of chirp. The data is normalized to the maximum fluorescence measured and the white X marks the chirp rate associated with a pulse discovered by the GA. b) Simulation of the 7p population as a function of pulse energy and chirp. U_0 is the minimum pulse energy for an inversion on the $3s - 4s$ transition, which corresponds to $\approx 12\mu$J for a uniform intensity profile with our focal geometry.

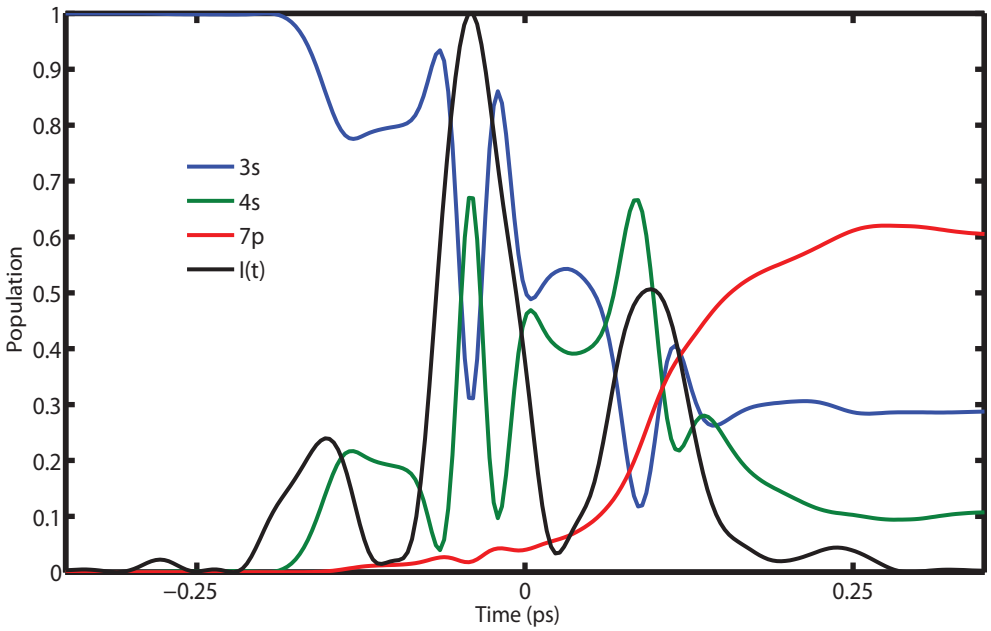

Figure 5.9: Calculated 7p, 4s, and 3s populations for a for an optimal pulse.

atoms are driven from the 3s to 4s state (two photon resonant at 777 nm and Stark shifted to the higher frequency, lower wavelengths) with the blue frequency components and then from the 4s to 7p state (resonant at 781 nm) with the red components, is effective. However, the counterintuitive ordering of the frequencies, as used in STIRAP, is not effective in this case. This is in direct contrast to measurements of ultrafast population transfer with single-photon mediated coupling between the levels [15]. We also used a measured optimal pulse to numerically integrate the Schrödinger equation using Eq. 5.2 and a pulse energy of 20μJ, shown in Fig. 5.9. In Fig. 5.9, the GA optimized pulse has temporal structure that is different from the pulses used in Fig. 5.8. However, the dynamics associated with a GA optimized pulse show that not only is the 7p population ~ 0.6 after the pulse turns off, but also the 4s intermediate state is populated throughout the atom-field interaction. The latter become important in paragraphs to come. Figure 5.10 shows calculated populations of the $3s$, $4s$ and $7p$ states as a function of time for pulses with a fixed energy of $3U_0$ and chirp rates of -0.002 ps^2 (panel c) and 0.002 ps^2 (panel d). Panels a) and b) show Wigner distributions for pulses with chirp rates of a) -0.002 ps^2 and b) 0.002 ps^2. The Wigner function for a chirped Gaussian

pulse is given by (see appendix A),

$$w(t,\omega) = \sqrt{\frac{2}{\pi\alpha}} e^{-[2\alpha\omega + \frac{1}{2\alpha}(\beta\omega - t)^2]} \tag{5.3}$$

where $\alpha = 1/\Delta\omega$, $\Delta\omega$ is the laser bandwidth, and β is the frequency domain chirp rate. For a negative chirp, the pulse starts blue detuned relative to the bare $3s - 4s$ transition frequency and is able to efficiently drive population from the $3s$ to $4s$ state on the rising edge of the pulse since a blue detuning can compensate for the average dynamic Stark shift on this transition [60]. Then as the frequency of the pulse sweeps to the red at high intensity, off-resonance Rabi oscillations (coherent transients [72]) drive population between the $3s$ and $4s$ states with decreasing amplitude. Finally, as the frequency of the pulse sweeps through resonance for the $4s - 7p$ transition, population is transferred to the $7p$ state resulting in a population inversion. The final $7p$ population is about ≈ 0.6. However, the opposite chirp, shown in panel b), yields a different behavior. Here, the pulse starts out closer to resonance with the $4s - 7p$ transition, but far off resonance with the $3s - 4s$ transition. As the intensity increases, the separation between the 3s and 4s states increases with the DSS, keeping these states out of resonance despite the increasing instantaneous frequency of the pulse. Once the pulse intensity reaches its peak and starts to decrease, with the instantaneous frequency still increasing, the pulse can sweep through resonance on the $3s - 4s$ transition, transferring population to the 4s state. Now the frequency is far detuned from the $4s - 7p$ transition frequency and the intensity is sufficiently low that there is ineffective transfer to the 7p. Rather than driving population from the $3s$ to the $7p$ state without going through the $4s$ (as one might expect if STIRAP were effective here), significant population is driven to the $4s$ state, and there is marginal transfer to the $7p$ state (≈ 0.09).

A dressed state analysis illustrates a key problem associated with adiabatic passage involving multiphoton coupling. Not only are the shape of the dressed states influenced unfavorably by the DSS (the avoided crossings become smaller), but more importantly, the spacing between avoided crossings scales differently with the intensity for single vs multiphoton coupling between levels, making the nonadiabatic corrections large for all chirp values at our pulse energies. Figure 5.11 shows the dressed states as a function of central wavelength for an intensity of $1.44 \times 10^{15} W/m^2$.

Analytic calculations of the nonadiabatic corrections to STIRAP are complicated by two features of our Hamiltonian: the detunings between the two pairs of states are not the same, and dynamic Stark shifts are on the diagonal entries of the Hamiltonian [73]. Therefore, we have calculated the nonadi-

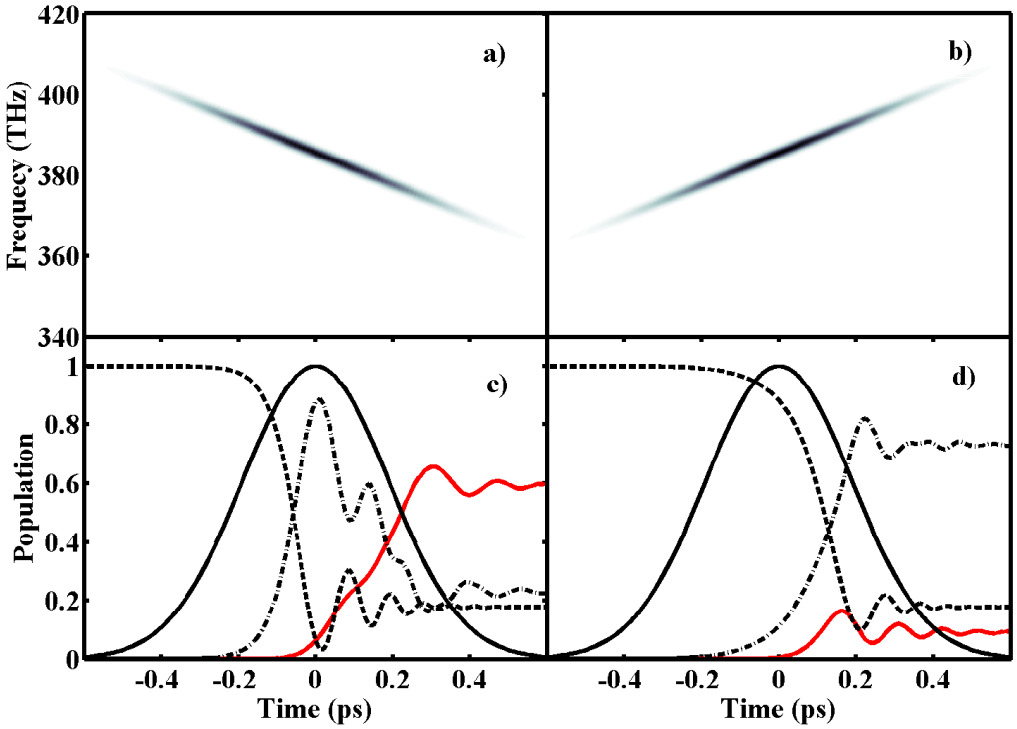

Figure 5.10: Calculated Wigner distributions according to Eq. (A.53) for chirp rates of a) -0.002 ps^2 and b) 0.002 ps^2. Panels c) and d) show the $3s$ (dashed), $4s$ (dash-dot), and $7p$ (solid red) populations, as well as the intensity envelope (solid black), corresponding to panels a) and b), respectively. U_0 is the minimum energy required for an inversion on the $3s-4s$ transition, which corresponds to $\approx 12\mu$J for a uniform intensity profile with our focal geometry.

abatic corrections to adiabatic passage numerically as a function of spectral chirp rate, β. This is the most natural pulse shape parameter to vary as it directly controls the time dependent detunings $\Delta(t)$ and $\Delta_{er}(t)$, and can be easily controlled at a fixed pulse energy. Our calculations compare the difference between the eigenvalues for the total effective interaction Hamiltonian and the adiabatic Hamiltonian normalized by the eigenvalues for the adiabatic Hamiltonian. This is a direct measure of adiabaticity [73] - when this normalized difference is much smaller than 1, then the passage can be adiabatic, but when the difference is large, then population can cross between dressed states and adiabaticity is lost.

If $\mathbf{U}(t)$ is the matrix that diagonalizes $\mathbf{H_I}(t)$: $\mathbf{D(t)} = \mathbf{U(t)}^{-1}\mathbf{H_I(t)U(t)}$, then the evolution of the dressed states is given by the total effective interaction Hamiltonian: $\mathbf{H_I'} = \mathbf{D} - i\mathbf{U}^{-1}\dot{\mathbf{U}}$, where $\mathbf{D}$ is a diagonal matrix with the dressed state energies as the diagonal elements. We computed the eigenvalues of $\mathbf{H_I'}$ and $\mathbf{D}$, and then divided their difference by the eigenvalues of $\mathbf{D}$ as a function of the frequency domain chirp parameter, β. Intuitively, one might expect the nonadiabatic corrections to decrease with increasing values of β since for $\beta >> 1/\tau^2$, $|\dot{\Delta}(t)| \sim \frac{1}{\beta}$, and the passage is more adiabatic for smaller $|\dot{\Delta}(t)|$. However, increasing β also decreases the peak electric field of the pulse. As the splitting between dressed states scales nonlinearly with the field for multiphoton coupling ($\chi \sim \varepsilon^2$ in our case), increasing β can actually increase the importance of the nonadiabatic corrections to the eigenvalues and make the passage less adiabatic. The criterion for adiabatic passage with single photon coupling, a single detuning, and a slowly varying envelope is usually given by $\frac{|\dot{\Delta}(t)|}{\chi^2(t)+\Delta^2(t)} \ll 1$ [73]. In our case, since $|\dot{\Delta}(t)| \sim 1/\beta$ and $\chi \sim 1/\beta$, it is clear by this criterion (for $\Delta = 0$) that increasing β makes the passage less adiabatic despite the fact that the frequency sweep is slower. Our numerical calculations of the nonadiabatic corrections, shown in fig. 5.11 illustrate this point for our Hamiltonian. The structure in the graph for low β is a result of the fact that we are showing the variation with β (as this is the experimentally relevant parameter), while it is $\dot{\Delta}(t)$ which determines the frequency sweep in time and $\Delta(t) = \Delta_0 - \frac{\beta t}{2(1/\tau^4+\beta^2)}$. For $\beta >> 1/\tau^2$ it is clear that increasing β leads to larger nonadiabatic corrections, as one expects from the reasoning above. Adiabatic passage for a chirped ultrafast laser pulse would require pulse energies one to two orders of magnitude higher than we have used in our experiments. For the optimal β value shown in the graph (~ 0.002), an increase in pulse energy by an order of magnitude would still leave nonadiabatic corrections of about 30%. Increasing the pulse energy by over an order of magnitude at this β value would lead to peak intensities higher than for an unshaped laser pulse and ionization would no

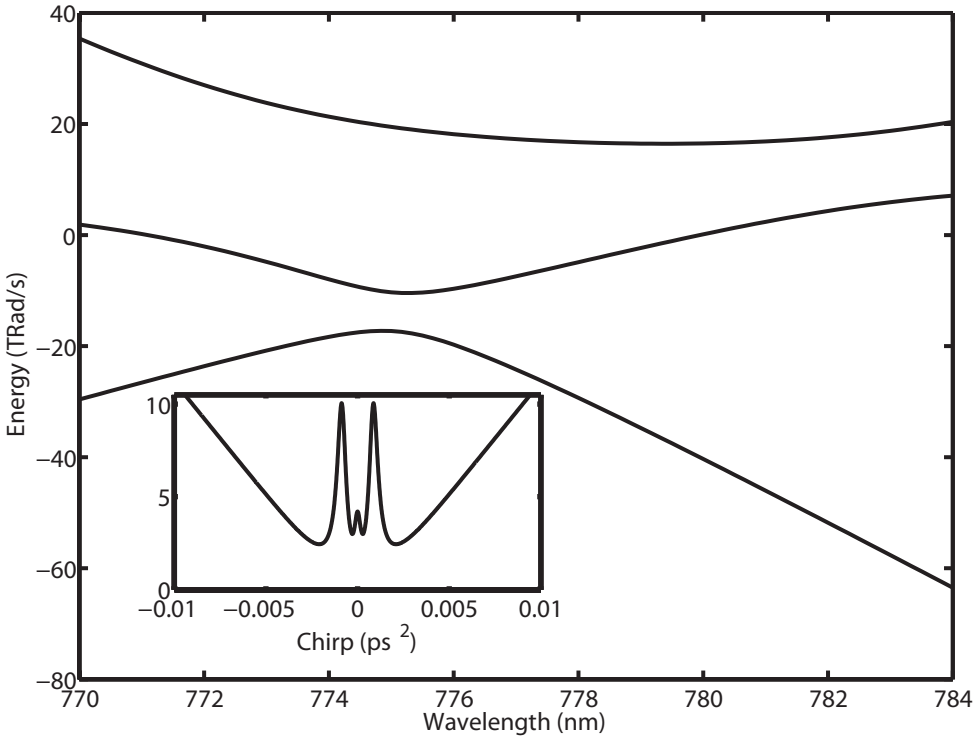

Figure 5.11: Calculated dressed states using $\mathbf{H_I}(t)$. The inset shows normalized nonadiabatic corrections for one of the eigenvalues of equation $\mathbf{H'_I}(t)$ as a function of β.

longer be negligible. Therefore, we argue that sequential population transfer is inherently more effective than adiabatic passage when using shaped ultrafast lasers to drive population transfer in a multilevel system using multiphoton coupling between levels.

Chapter 6

A Four Level Atomic Interferometer

6.1 Introduction

In this chapter, we extend the discussion of strong field population transfer to more that three levels and allow for two resonant intermediate states between a ground and excited state, where this four-level system forms the analog of an interferometer. Interference is one of the most fundamental aspects of quantum mechanics, and it has been exploited in a wide array of experiments with atoms to infer the phase of a wave function or to make sensitive measurements of energy shifts. Interference has also been used as a way to control the state of quantum systems by arranging for constructive interference in the desired final state and destructive interference in all others [74]. With this type of 'coherent control', the phase of different frequency components of a coherent light field are adjusted in order to vary the phase of different pathways in quantum phase space from a given initial state to the desired target state. When the applied electric fields are weak, and perturbation theory applies, the phase between pathways is directly proportional to the phase of the light fields corresponding to each pathway [11–13] However, for strong fields, where perturbation theory breaks down, the phases of the different frequency components in the light field are no longer directly related to the phases of the different pathways between initial and final states [15, 38, 39, 64, 75].

Here we analyze a four-state, two-path atom interferometer, where each path in the interferometer is excited by pairs of frequency components in a shaped ultrafast laser pulse, as shown in Fig. 6.1. By modulating the phase of one of the four resonant frequency components, we can modulate the phase of one arm of the interferometer relative to the other, thereby modulating the

population in the final state. As we move from only resonant frequencies to the full broadband spectrum of the pulse, and increase the strength of the field, we see that the phase of the interference fringes change substantially, while still displaying a sinusoidal dependence on the applied spectral phase. In weak fields where only the resonant frequency components are present, the interference fringes result from interference between the two pathways in the interferometer. With a broadband source, where non-resonant frequency components present, we demonstrate that the majority of the interference is occurring within a given pathway.

Our experiment is carried out in atomic Rubidium, where two-photon absorption through two separate intermediate states is possible using a single shaped femtosecond pulse [14]. The four resonant transition frequencies are contained within the bandwidth of the pulse (the bandwidth of our laser is about 30 nm FWHM, with spectral intensity from approximately 750 nm to 810 nm) and our ultrafast optical pulse shaper [41] is able to modify the phase of each resonant frequency. The four level system is the atomic analog of a Mach-Zehnder interferometer [76–78]. By varying the phase of either resonant frequency, we measure the interference of both $5S \rightarrow 5P \rightarrow 5D$ transitions as a function of pulse energy. We compare our measurements to calculations of the dynamics which are valid in both weak and strong field domains.

6.2 Experimental Apparatus

The shaped pulses were directed into a 6 cm long glass cell containing Rubidium gas at 150^{o}C. The maximum pulse energy and intensity at the center of the cell for the focal geometry we use are 30μJ and 10^{14} W/m^2, respectively. To capture the pulse shape dependence on two-pathway two-photon absorption from the 5S to 5D states, we measured fluorescence from the excited atoms. The fluorescence was collected from the center of the cell at 90^o with respect to the beam propagation direction using a photomultiplier tube. We measured the $6P \rightarrow 5S$ transition (as part of the $5D \rightarrow 6P \rightarrow 5S$ decay) at 420 nm.

Using our pulse shaper, we could vary the phase of any of the four resonant transition frequencies ($5S_{1/2} \rightarrow 5P_{1/2}$, $5S_{1/2} \rightarrow 5P_{3/2}$, $5P_{1/2} \rightarrow 5D_{3/2}$, and $5P_{3/2} \rightarrow 5D_{3/2}$) by placing a spectral phase window around the transition frequency (as shown in Fig. 6.1(a) and (b)), and block out any frequency components from our spectrum, such as the non-resonant frequency components in the pulse spectrum (as shown in Fig. 6.1(c)). The phase modulation was over a narrow window approximately 0.8 nm wide that was programmed to vary between 0 and 2π. We made separate measurements of the fluorescence as a function of applied phase for the phase window centered on each of the

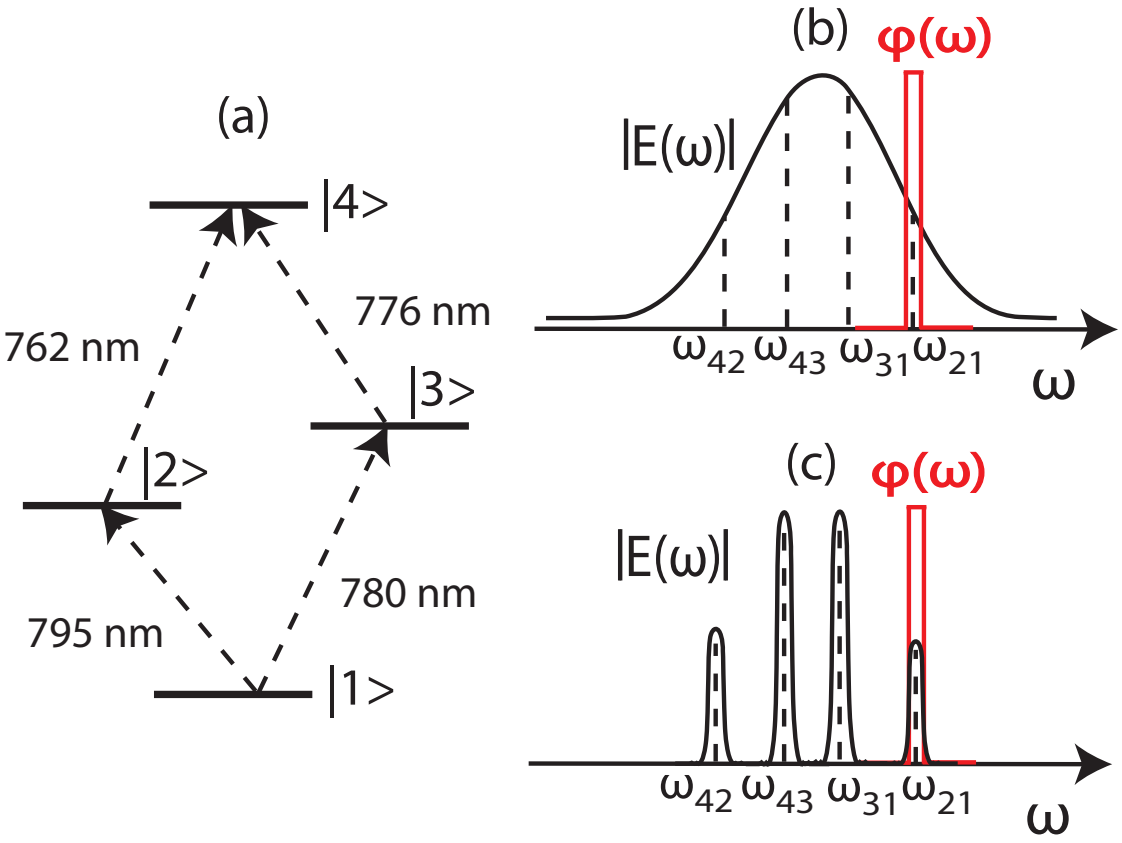

Figure 6.1: Grotrian diagram and illustration of the laser. (a) Grotrian diagram showing the two-path interferometer in atomic Rubidium with the relevant transition wavelengths. (b) Illustration of the electric field amplitude $|E(\omega)|$, the four resonant transition frequencies, and the spectral phase $\varphi(\omega)$. (c) Illustration of the electric field with only the resonant frequencies and the spectral phase

resonance lines in the atom, as illustrated in Fig. 6.1(b) by ω_{21}, ω_{31}, ω_{42}, and ω_{43}.

6.3 Experimental Results

Fig. 6.2 shows the $6P \rightarrow 5S$ fluorescence (proportional to the 5D population immediately after the excitation pulse) as a function of spectral phase for a narrow window around 776 nm. The results are shown for the case of weak field excitation with resonant frequencies only, as illustrated in Fig. 6.1(c) (dotted black curve), weak field excitation with resonant and non-resonant frequencies present, as illustrated in Fig. 6.1(b) (solid red curve) and strong field excitation with all frequencies present (dot dash blue curve). Measurements performed for varying the phase of the light at 795 nm, 780 nm and 762 nm yielded similar results to the ones shown in Fig. 6.2(a).

As we only modulate one transition frequency at a time (in contrast with earlier work [14]), the fluorescence yield goes through one modulation per 2π applied phase. Measurements we performed where the window was placed at half the two photon resonance (778 nm) displayed two periods per 2π phase at higher strengths.

6.4 Discussion

As one expects from perturbation theory, the fluorescence yield varies sinusoidally with the applied window phase, independent of which resonant frequency is phase modulated. Denoting the 5S ground state by $|1\rangle$, the $5P_{1/2}$ by $|2\rangle$, the $5P_{3/2}$ by $|3\rangle$ and $5D_{3/2}$ state by $|4\rangle$, the excited state amplitude through both intermediate resonances is given in the perturbative limit as [12]:

$$P_{5D} \propto \Bigg| \mu_{12}\mu_{24} \left[E(\omega_{21})E(\omega_{42}) + iP.V. \int_{-\infty}^{\infty} d\omega \frac{E(\omega)E(\omega_{41}-\omega)}{\omega_{21}-\omega} \right] + \mu_{13}\mu_{34} \left[E(\omega_{31})E(\omega_{43}) + iP.V. \int_{-\infty}^{\infty} d\omega \frac{E(\omega)E(\omega_{41}-\omega)}{\omega_{31}-\omega} \right] \Bigg|^2 . \quad (6.1)$$

Here, μ_{ij} is the transition dipole moment between states $|i\rangle$ and $|j\rangle$ for linearly polarized light, P.V. is the Cauchy principle value operator, and $E(\omega_{ij}) = |E(\omega_{ij})|\, e^{i\phi_{ij}}$. In Eqn. 6.1, $E(\omega_{21})E(\omega_{42})$ and $E(\omega_{31})E(\omega_{43})$ can be interpreted as the resonant contributions for each pathway with the principle value

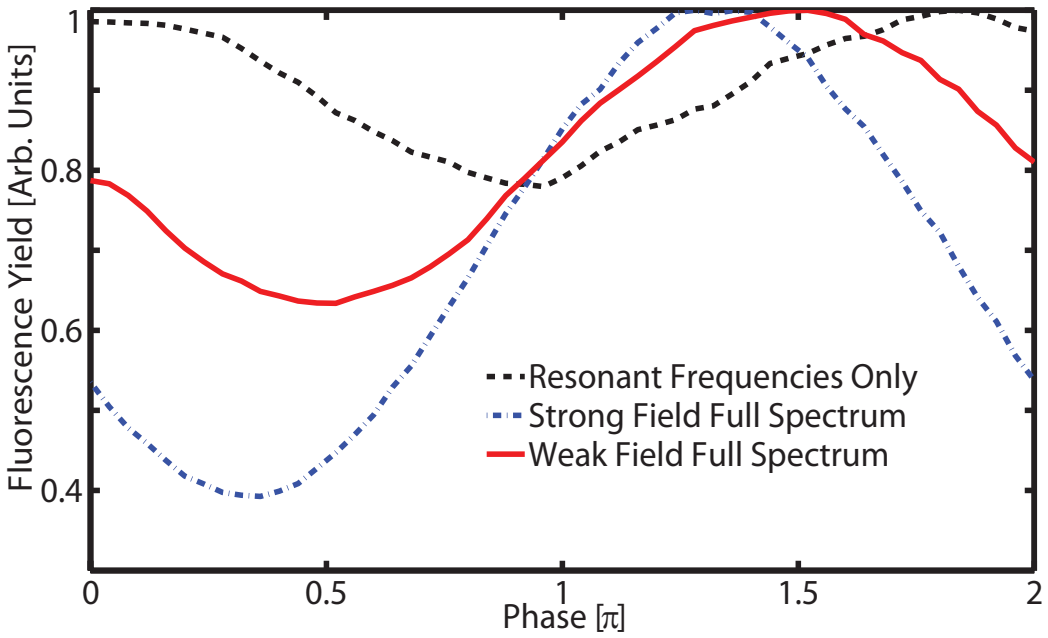

Figure 6.2: 5D population as a function of spectral phase on the 776 nm $5P3/2 \rightarrow 5D$ transition. The dotted black curve corresponds to the case where only the resonant frequencies in the broadband pulse were present and all other frequencies were blocked. The solid red curve corresponds to the case of spectral phase modulation with the full spectrum, but weak fields (where perturbation theory is valid and there is no significant ground state depletion). The blue dot dashed curve represents measurements for the case of the full spectrum with strong fields where significant population is transferred from the ground state.

integrals corresponding to the non-resonant contributions for each pathway.

The perturbative expression above has four terms which can all interfere with one another and yields a simple and intuitive interpretation of the weak field measurements shown in Fig. 6.2. In the simplest case of weak field excitation with only the resonant frequencies present, only $E(\omega_{21})E(\omega_{42})$ and $E(\omega_{31})E(\omega_{43})$ in Eqn. 6.1 contribute to the 5D population. Varying the phase of one of the resonant frequencies in one of the two pathways leads to constructive and destructive interference in the $5D3/2$ state. The $5D$ population is maximum for zero applied spectral phase and minimum for π, as one expects given that the transition dipole moments are real and positive (dotted black curved of Fig. 6.2. The limited modulation depth is a consequence of the fact that the two resonant pathways have different amplitudes (both the dipole moments and the spectral density are lower for the $5P1/2$ pathway) and that while we measure florescence from both the $5D5/2$ and $5D3/2$ states, the $5D5/2$ cannot be accessed via the $5P1/2$ pathway.

In the case of weak field excitation with the full spectrum, all four terms in Eqn. 6.1 must be taken into account, as there can be interference between resonant and non-resonant terms. The phase of the modulation in the data for this case (a maximum at $3/2\pi$ and a minimum at $\pi/2$) indicates that the modulation is no longer determined by interference between the first two terms, but is rather now largely occurring between the first and third and second and fourth terms. These have a $\pi/2$ difference between them in Eqn. 6.1. Applying a $-\pi/2$ (equivalent to $3\pi/2$) phase on the light at 776 nm compensates for intrinsic phase offset between resonant and non-resonant contributions for the $5P3/2$ pathway and allows the second and fourth terms to interfere constructively, leading to a maximum in the 5D population. Further evidence that interference shifts from between resonant pathways in the resonance only case (Fig. 6.1(b)) to between resonant and non-resonant terms in a given pathway in the full spectrum case (Fig. 6.1(c)) is found by blocking one of the resonant transition frequencies for the $5P1/2$ pathway and noting that the $5D$ population as a function of phase applied to the light at 776 nm looks the same as shown in Fig. 6.2. Figure 6.3 below shows that the modulations in the $5D$ population as a function of applied spectral phase window persist with a large depth of modulation when one arm of the interferometer is blocked. Both measurements and calculations (described below) are shown, and are in excellent agreement.

Finally, in the case of strong field excitation, we note that the phase of the modulation shifts from the case of weak field excitation and the modulation depth increases significantly. These features cannot be described by Eqn. 6.1, and we therefore turn to numerical integration of the time-dependent

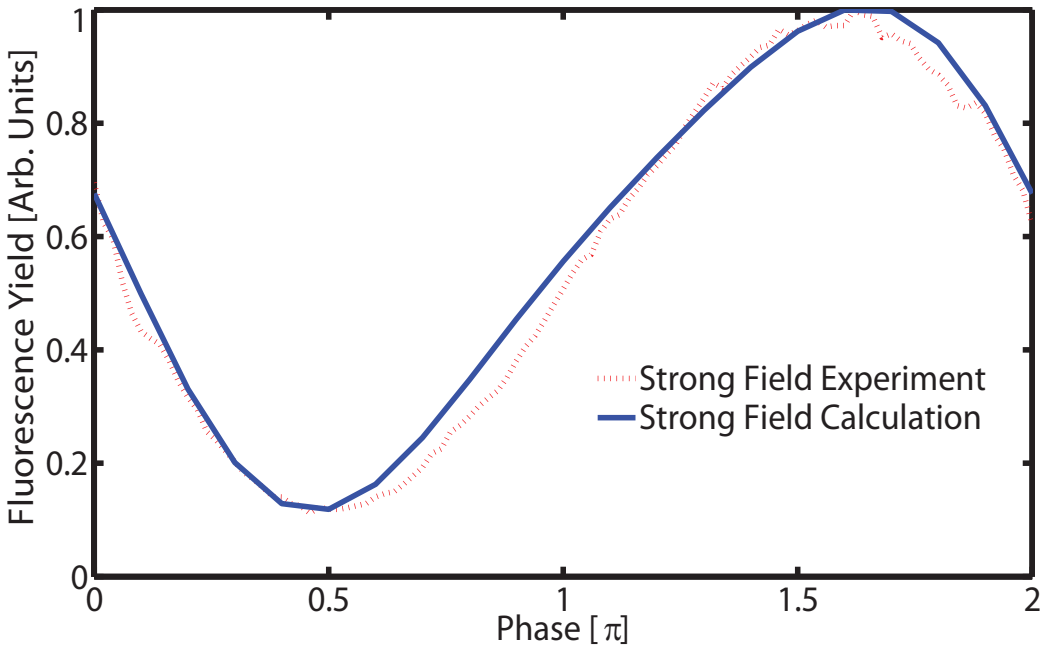

Figure 6.3: Measured and calculated $5D$ interference as a function of phase applied to 795 nm while blocking 780 nm.

Schrödinger equation for some more detailed insight into the measurement. We consider the atom as a 4-level system where the $5S_{1/2} \rightarrow 5P_{1/2}$, $5S_{1/2} \rightarrow 5P_{3/2}$, $5P_{1/2} \rightarrow 5D$ and $5S_{3/2} \rightarrow 5D$ transitions are all within the bandwidth of our laser. We can express the Hamiltonian for the atom-field interaction (after making the Rotating Wave Approximation) as, $\mathbf{H}\hat{(}t) =$

$$\begin{pmatrix} 0 & \chi_{12}(t)e^{i(\Delta_{21}t-\phi(t))} & \chi_{13}(t)e^{i(\Delta_{31}t-\phi(t))} & 0 \\ \chi^*_{12}(t)e^{-i(\Delta_{21}t-\phi(t))} & 0 & 0 & \chi_{24}(t)e^{i(\Delta_{42}t-\phi(t))} \\ \chi^*_{13}(t)e^{-i(\Delta_{31}t-\phi(t))} & 0 & 0 & \chi_{34}(t)e^{i(\Delta_{43}t-\phi(t))} \\ 0 & \chi^*_{24}(t)e^{-i(\Delta_{42}t-\phi(t))} & \chi^*_{34}(t)e^{-i(\Delta_{43}t-\phi(t))} & 0 \end{pmatrix}. \tag{6.2}$$

Here, $\chi_{ij}(t) = \frac{\mu_{ij}E(t)}{\hbar}$ is the Rabi frequency where E(t) is the field envelope, ω_0 is the central frequency of the laser, $\omega_{ij} = \omega_i - \omega_j$, $\Delta_{ij} = \omega_0 - \omega_{ij}$ is the detuning, and $\phi(t)$ is the field phase. Using Eqn. 6.2 we numerically simulated the 5D population as a function of phase modulation and pulse energy. We

modeled the shaped electric fields used in the experiment by:

$$\begin{aligned} E^{res}(\omega) = E(\omega_{21})e^{-(\omega-\omega_{21})^2/(\delta\omega)^2} + \\ E(\omega_{31})e^{i\phi}e^{-(\omega-\omega_{31})^2/(\delta\omega)^2} + \\ E(\omega_{42})e^{-(\omega-\omega_{42})^2/(\delta\omega)^2} + \\ E(\omega_{43})e^{-(\omega-\omega_{43})^2/\delta\omega^2} \end{aligned} \tag{6.3}$$

and

$$\begin{aligned} E^{full}(\omega) = E(\omega)e^{-(\omega-\omega_0)^2/(\Delta\omega)^2} - \\ E_{nm}e^{-(\omega-\omega_{nm})^2/(\delta\omega)^2} + \\ E_{nm}e^{i\phi}e^{-(\omega-\omega_{nm})^2/(\delta\omega)^2} \end{aligned} \tag{6.4}$$

for the case of the spectrum with just the resonant frequency components present and the full spectrum, respectively. The central frequency of the laser pulse is given by ω_0, the frequencies of the four resonant transitions are given by ω_{nm} (Fig. 6.1), the width of the full and resonant components only spectra are given by $\Delta\omega$ and $\delta\omega$ respectively, and the applied phase in the window of choice is given by ϕ. Our calculations are able to reproduce our experimental measurements of the $5D$ population as a function of applied spectral phase and intensity. An example of the agreement is shown in Fig. 6.3 for the case of modulating the phase of 795 nm while blocking a narrow window of frequencies around 780 nm.

In order to appreciate the population dynamics for the phase-window-shaped pulses, it is helpful to look at the shaped laser pulses in a time-frequency distribution. Figure 6.4 shows the Wigner function for pulses with phase modulation at 776 nm and 780 nm [71]. In the time domain, the phase window shaping results in an intense broadband short pulse, surrounded by a low amplitude narrowband pulse whose central frequency corresponds to the location of the phase window, shown in Fig. 6.4.

Fig. 6.5 highlights the atomic dynamics behind single path (time domain) interference, when one of the interferometer arms is blocked. Panels (a) and (b) show the $5S_{1/2}$, $5P_{1/2}$ and $5D_{3/2}$ populations as a function of time for pulses shaped with a phase window at 795 nm and the light at 780 nm blocked. Both panels also show the electric field envelope for the phase-shaped pulses. The calculations are for an intermediate field strength/intensity, corresponding to the calculations and measurements shown in Fig. 6.3. Panel (a) shows the dynamics for a pulse with a phase of 0.6π at 795 nm and panel (b) shows the dynamics for a pulse with a spectral phase of 1.6π around 795 nm.

As Fig. 6.4 shows, the phase window shaping results in a short pulse

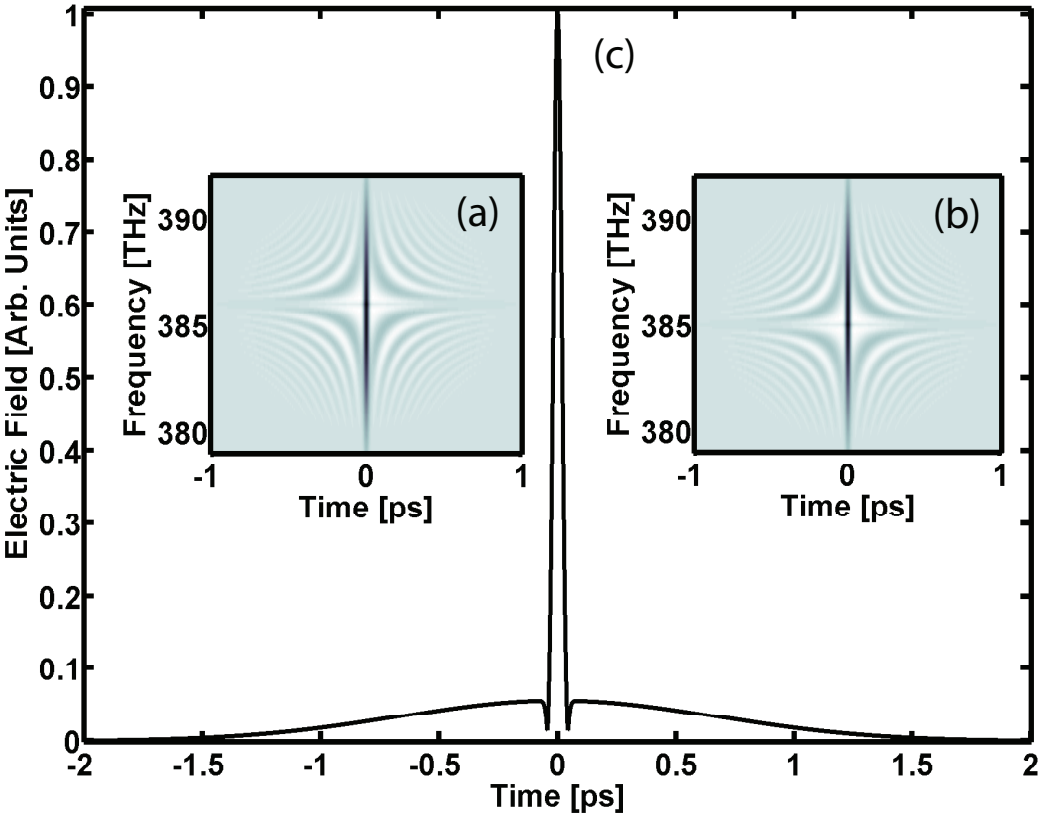

Figure 6.4: Wigner plots of the phase shaped pulses. (a) The Wigner plot of a pulse with the phase window located at 776 nm (386.5 THz). (b) The Wigner plot of a pulse with the phase window located at 780 nm (384.6 THz). (c) The electric field envelope associated with (a) and (b).

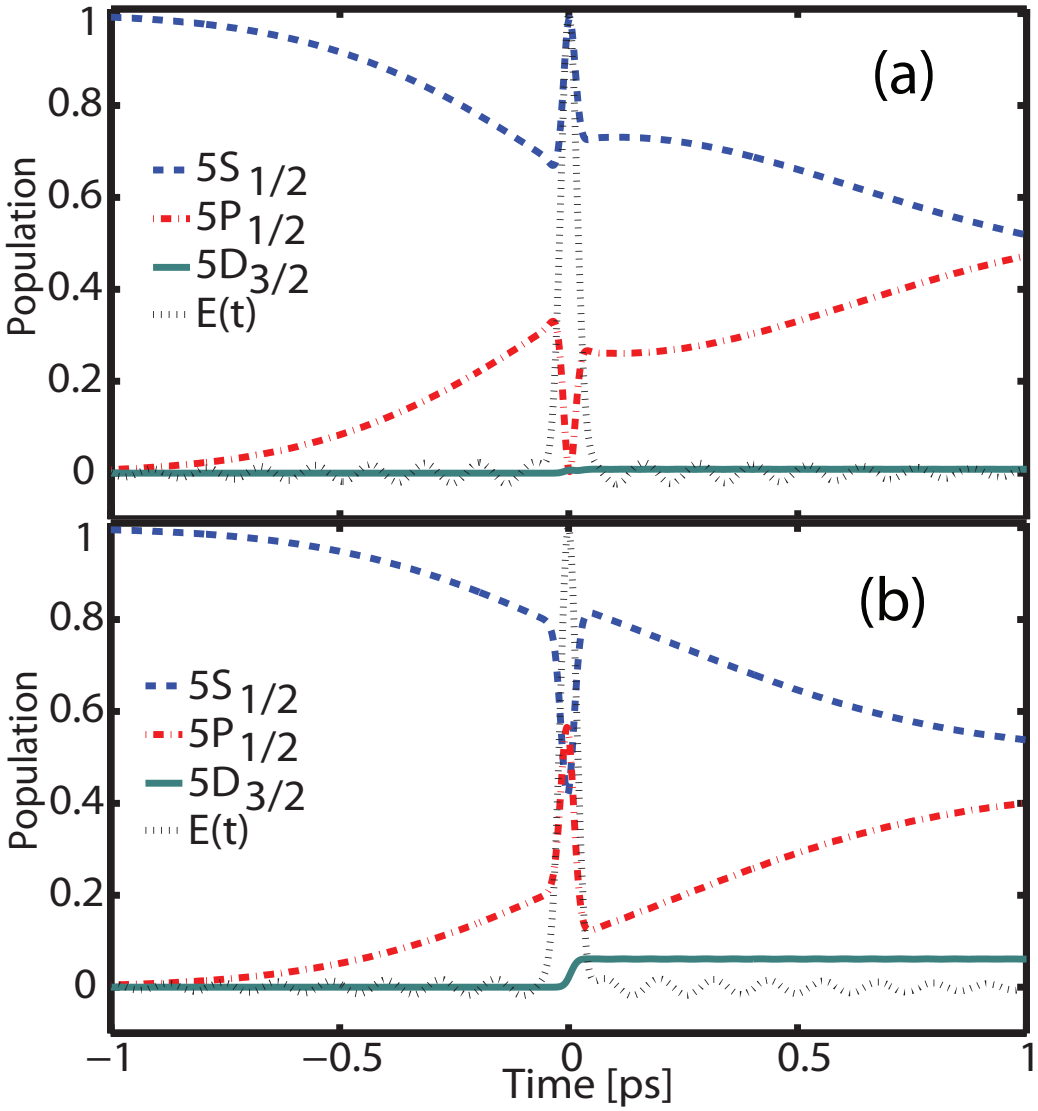

Figure 6.5: Populations dynamics as a function of time for phase shaped pulses. The dynamics in panel (a) correspond to the interference minimum in Fig. 6.3. The dynamics in panel (b) correspond to the interference maximum in Fig. 6.3).

surrounded by a broad ps pulse whose central frequency corresponds to the frequency whose phase is modulated. Modulating the phase of light at 795 nm results in a broad ps pulse which begins to transfer population between the $5S_{1/2}$ and $5P_{1/2}$ states (resonant at 795 nm) before the short pulse arrives. Varying the spectral phase of the light at 795 nm controls both the amplitude of the long pulse as well as the phase relative to the short one. Thus, the population transferred by the long pulse can add destructively (as shown in panel (a)) or constructively (as shown in panel (b)). This leads to a maximum or minimum in the 5D population as a function of applied spectral phase. The shift in the phase of the modulations with field strength (shown in Fig. 6.2) can be understood in the time domain in terms of the strong field phase advance of the atomic coherences -i.e. Rabi oscillations [64, 79]. Perturbation theory works well in describing the interaction between the atoms and a laser pulse whose Rabi frequency is much smaller than the laser frequency, or where the pulse area is much smaller than π. However, when the pulse area approaches or exceeds π (considering any pair of levels in the system), then the phase advance of the atomic coherence is not locked to the phase advance of the optical field (they evolve by exactly π for a π pulse). The phase of the field for the long pulse relative to the short pulse to must therefore be adjusted from the weak field case in order to maximize population transfer to the $5D$ state.

Chapter 7

Ultrafast Atomic Phase Modulation

7.1 Introduction

In this chapter we utilize the time-domain concepts developed in chapters 4 and 5 to carry out and interpret a simple ultrafast pump-probe experiment in atomic Rb which demonstrates Electromagnetically Induced Transparency (EIT) like features. EIT can render an optically-dense transition transparent and influence its dispersion [80, 81]. The technique is based on the interaction of two fields with a three-level Λ- or ladder-system. A resonant coupling field dresses the two unpopulated states and produces an Autler Townes (AT) splitting [82], which is measured by a probe field. If the AT splitting is larger than the probe pulse bandwidth and the natural linewidth of the probe transition, then the probe pulse can pass through unabsorbed. EIT differs from transparency off resonance, where the time-averaged cycling of absorption and emission leads to transparency. Rather, in EIT the absorption associated with two dressed states created by the coupling pulse cancel each other at all times. EIT has been used in applications where large absorption masks other physical attributes of the system such as dispersion at the transition frequency. Experiments have demonstrated slow light [83] and enhancement of nonlinear processes [84, 85].

There is significant interest in developing ultrafast implementations of EIT for applications such as ultrafast phase modulation and switching of x-rays [86–88]. In ultrafast applications of EIT there are two important differences to consider. First, the pulse durations can be much faster than relaxation processes, such as spontaneous emission and collisions. Second, the time dependence of the coupling Rabi frequency leads to a varying AT splitting, thus

complicating a description of the dynamics. A strong coupling pulse drives an atomic coherence which modifies the transmission of a probe pulse. The probe and coupling pulses are generated by a pulse shaper from a single ultrafast laser pulse. Here we find that a time-domain picture is useful in describing the dynamics and interpreting the results. The changing coupling field strength leads to changing phase differences between the probe field and dressed states (the 'atom-field phase' discussed below) during the interaction, which causes an interplay of absorption and stimulated emission at different frequencies. Our experimental measurements are compared with calculations of the atom-field interaction in order to arrive at a detailed understanding of the dynamics. Our measurements illustrate transparency at the quadratically Stark shifted transition frequency [1], as well as lasing without inversion.

7.2 Experiment

The experiment was carried out in atomic Rb, where probe and coupling pulses were resonant on the $5S_{1/2} \rightarrow 5P_{3/2}$ transition at 780 nm and $5P_{3/2} \rightarrow 5D_{3/2,5/2}$ transition at 776 nm, shown in Fig. 7.1. As the separation between the $5D_{3/2}$ and $5D_{5/2}$ states is less than the bandwidth of the coupling pulse, these two states were treated as one. The coupling pulse intensity was adjusted to yield a coupling Rabi frequency on the order of the probe pulse bandwidth and the intensity of the probe pulse was chosen to be more than 100 times lower than the coupling pulse to ensure minimal population transfer by the probe pulse. Our main results consist of measurements of the probe spectrum as a function of delay between the probe and coupling pulses. Additionally, we also measured cross-correlations between the probe and coupling pulses before and after the sample.

We created two pulses resonant on the coupling and probe transitions, with spectral widths of 0.5 nm and 1.8 nm, respectively, as illustrated in Fig. 7.1. Additionally, the pulse shaper allowed us to delay the coupling pulse with respect to the probe pulse, up to ± 20 ps, by introducing a linear spectral phase across the coupling pulse. Light from the pulse shaper was directed into a 6.0 cm long heated Rb cell ($T \sim 130\text{C}^\circ$) with a combination of two lenses used to generate a 440 μm focal spot size with a 19.5 cm Rayleigh range, ensuring minimal longitudinal intensity variation. Working in a focus helped to overcome the small steering of the coupling beam due to the applied phase

[1] Since the detuning of the coupling pulse from the probe transition is larger than either of the two Rabi frequencies, there is a quadratic Stark shift of the 5s-5p transition directly due to the coupling pulse: $\delta_{\text{AC}} = \frac{1}{2}\left(\sqrt{(\omega_c - \omega_{12})^2 + (\mu_{12}\varepsilon_c/\hbar)^2}\right)$ [58] and yields a value of $\delta_{\text{AC}} = (0.16 \pm 0.06)$ THz.

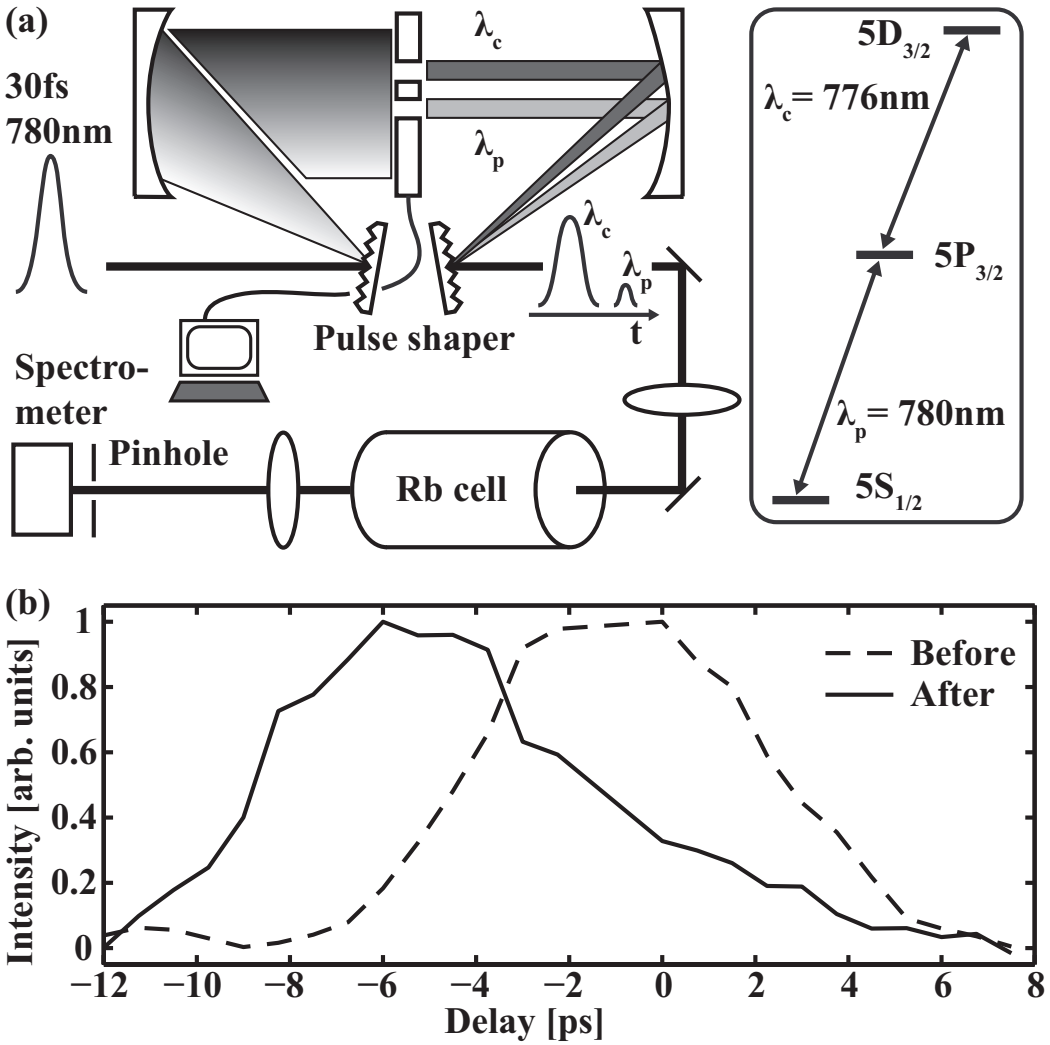

Figure 7.1: (a) shows the experimental setup. A 30 fs pulse was used by the pulse shaper to create two narrow bandwidth pulses resonant on the coupling and probe transitions at 776 nm and 780 nm respectively, delayed in time by up to ±20 ps. They were focused into the Rb cell and measured with a spectrometer. (b) shows the temporal cross-correlation of probe and coupling pulses before (dashed) and after (solid) the cell.

in the pulse shaper [49]. A third lens after the cell imaged the interaction region onto a 75 μm pinhole in front of a spectrometer, thus circumventing transverse intensity volume averaging. We averaged about 1300 pulses for each measured probe pulse spectrum.

To characterize the atom-field interaction, we measured the probe pulse spectrum as a function of delay between the coupling and probe pulse. The pulse shaper delayed the coupling pulse in time between +7 ps and −14 ps with respect to the probe pulse. Second Harmonic Generation Frequency Resolved Optical Gating [89] measurements calibrated the delay time with an error of 5%. The spectrum of the probe pulse was measured at 30 different equally spaced delays within the given range. The coupling pulse used in our measurements had a duration $\tau_c = (3.5 \pm 0.5)$ ps. The peak coupling field strength was $\varepsilon_c = (4.7 \pm 1.0) \times 10^7$V/m, as determined from the measured pulse energy, temporal duration, and spot size in the cell. The probe pulse was 130 times smaller in intensity and three times shorter. Figure 7.1(b) shows the intensity cross-correlation of the two pulses, measured by recording the probe-coupling sum frequency generation signal in a KDP crystal before and after the cell. The dashed line is the result from before and the solid line from after the cell. Negative time delays refer to a retardation of the coupling pulse in the pulse shaper. Before the cell the cross correlation is peaked at roughly zero, whereas after the cell the cross-correlation maximum was shifted by -5 ps, indicating that the probe pulse is delayed relative to the coupling in passing through the sample.

7.3 Results

Figure 7.2(a) shows the probe spectrum as a function of delay between the coupling and probe pulses. For long delay times (at the upper and lower edge of the data) the pulses were not temporally overlapped in the cell. Thus, the probe pulse did not experience any AT splitting on the transition and was therefore absorbed at and near 780 nm [2]. The scale is normalized to the maximum intensity in these spectra at long delays. Around -3 ps the small absorption feature at the center of the spectrum changes into a structure with two absorption features at shifted frequencies, a peak at the quadratically Stark-shifted line center, and two peaks at the edges of the spectrum as a result of gain in the sample. The inset in Fig. 7.2(b) shows the marginal of

[2]For an infinitesimally weak probe pulse longer than the relaxation time of the excited state, the absorption should be within the natural linewidth of the transition. However, for a short pulse with a non-negligable pulse area, the probe will experience absorption across a spectrum of frequencies determined by the Rabi frequency of the probe pulse.

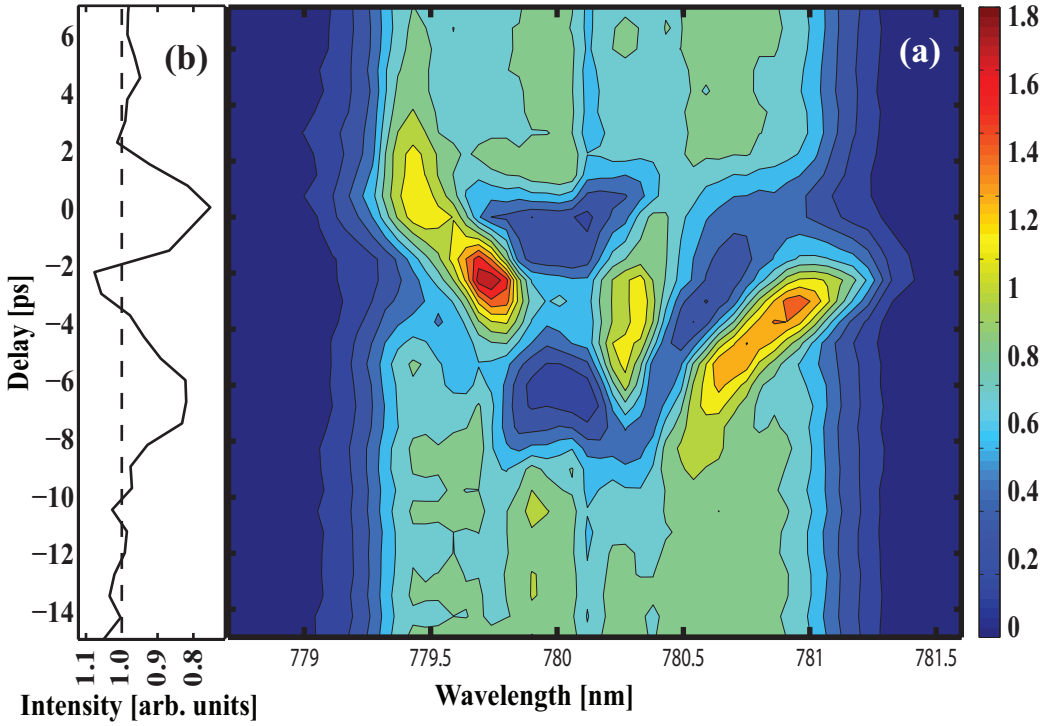

Figure 7.2: Probe spectrum vs probe-coupling delay with wavelength marginal. (a) shows the probe spectrum as a function of time delay between coupling and probe pulse. Around -3 ps the regular absorption line changes into a symmetric structure of three gain and two absorption regions. (b) shows the projection of the data onto the delay time axis. For 0 ps and -7 ps the probe pulse shows a reduction of 20% in integrated intensity whereas for -3 ps there is none.

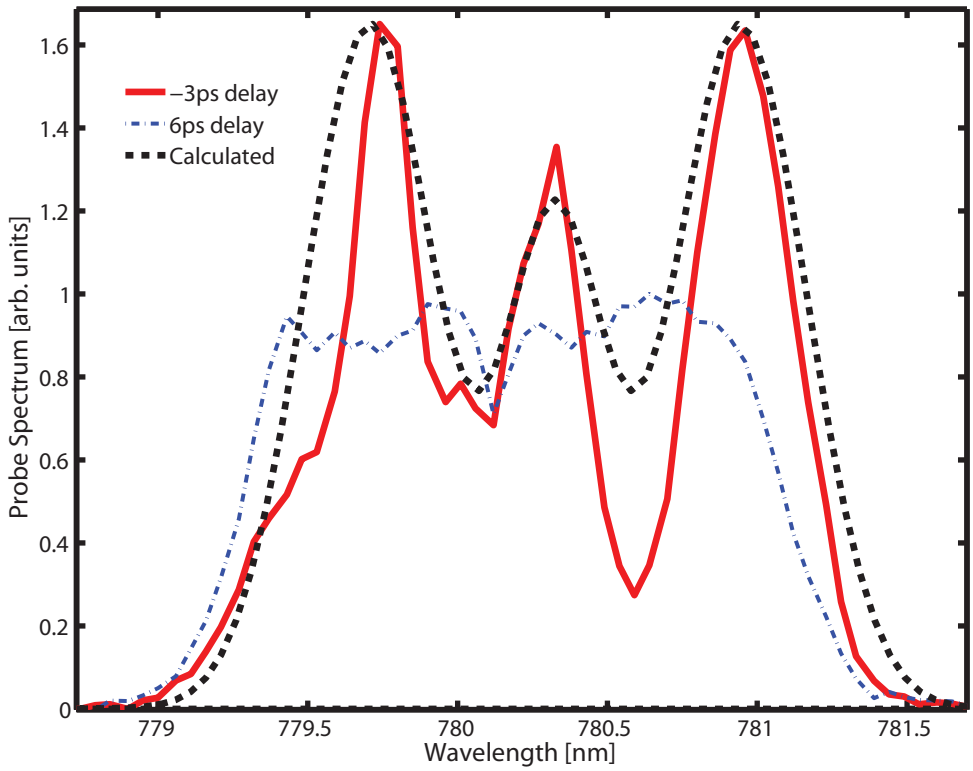

Figure 7.3: Measured and calculated probe spectra. The dashed-dot blue line shows the probe spectrum with an absorption line at 780 nm at 6 ps delay time (no interaction between the pulses). The solid red curve from delay time -3 ps shows a symmetric structure with two absorption and three gain regions. The dashed black curve shows the result of numerically integrating the coupled Maxwell-Bloch equations.

the 2D data on the time delay axis (generated by integrating over the spectrum of the probe at each time delay). The curve is normalized to the integral at long delay times. Around 0 ps and -7 ps the probe pulse shows an absorption of $\sim 20\%$ relative to long probe-coupling delays.

Figure 7.3 shows lineouts of Fig. 7.2(a) at -3 ps (solid red) and at 6 ps (dashed-dot blue) along with the result of calculations described below (dashed black). The scale is normalized to maximum value in the spectrum at long delays (6 ps). The spectrum at 6 ps shows absorption at 780 nm, broadened and damped by the resolution of our spectrometer. The line at -3ps shows gain and absorption features noted in the 2D data above.

7.4 Discussion

There are two main features in the data which merit discussion. The first is the fact that the probe pulse is delayed with respect to the coupling pulse and reshaped in traversing the sample. The second is that the probe spectrum changes significantly with probe-coupling delay, showing both stimulated absorption and emission. To understand these features, we numerically solved the coupled Maxwell-Bloch equations (see appendix A) for a three-level Rubidium ensemble interacting with two light fields over the distance of our cell [90], using parameters measured in our experiment.

$$\frac{\partial}{\partial z}\mathbf{E}_p(z,t) = \frac{i\omega_p N\mu_{12}}{2\epsilon_0 c}\rho_{21}(z,t) \tag{7.1}$$

$$\frac{\partial}{\partial z}\mathbf{E}_c(z,t) = \frac{i\omega_c N\mu_{23}}{2\epsilon_0 c}\rho_{32}(z,t). \tag{7.2}$$

Here, $5s_{1/2} \rightarrow 5p_{3/2}$ ($|1> \rightarrow |2>$) and $5p_{3/2}$ - 5d ($|2> \rightarrow |3>$), $\mathbf{E}_p(z,t)$ and $\mathbf{E}_c(z,t)$ are the probe and coupling fields, respectively, ω_p and ω_c are the probe and coupling central frequencies, N is the atomic density, μ_{12} and μ_{23} are the dipole matrix elements taken from [91], and ρ_{21} and ρ_{32} are the atomic coherences for the probe and coupling transitions, respectively. We also performed the calculations with relaxation included in the equations above and found no significant difference in the results within the time window of interest.

The dashed-black line in Fig. 7.3 shows that our calculations of the probe spectrum reproduce the experimental measurement with no adjustable parameters. We thus make use of the calculations to interpret the atom-field dynamics leading to the features observed in our measurements. Figure 7.4 shows the results of our calculations relevant to interpreting the measurements. The red-dashed and red-solid lines show the calculated probe pulse field envelope before and after the cell, respectively, as well as the coupling pulse field envelope after the cell, represented by the blue-dashed-dot line. The dotted black line shows the atom-field phase plotted in units of π. The atom-field phase is the phase advance of the probe transition coherence (with the coupling laser dressing the $5P_{3/2} \rightarrow 5D$ transition) relative to the probe field, $\varepsilon_p(t)$, as a function of time [92]. In the case of no coupling field and a resonant cw probe, the atom-field phase advances at one half of the probe Rabi frequency, Ω_p, with the atom cycling between absorption and emission as the atom-field phase evolves between even and odd values of π. For a strong coupling field and a weak resonant probe (such that $\Omega_p \ll \Omega_c$), the atom-field phase for the probe field and the $5S_{1/2} \rightarrow 5P_{3/2}$ coherence advances at half the generalized *coupling* Rabi frequency ($\tilde{\Omega}_\mathrm{c} = \sqrt{\Omega_\mathrm{c}^2 + \Delta_\mathrm{c}^2}$, where Δ_c is the detuning of the

coupling pulse) and is given by,

$$\alpha(t) = \pm\frac{1}{2}\int_{-\infty}^{t} \tilde{\Omega}_{\mathrm{c}}(\tau)d\tau. \tag{7.3}$$

Our calculations indicate that the probe pulse is absorbed and emitted at later times during the coupling pulse as it propagates through the sample - the probe pulse creates an atomic polarization which radiates and is modulated by the coupling pulse. The absorption of the probe pulse occurs on the leading edge of the coupling pulse where the atom-field phase is advancing slowly and stays less than $\pi/2$. The coupling pulse facilitates absorption over a broad range of probe frequencies via dynamic Stark shifting of the probe transition, and hence a changing AT splitting. As the atom-field phase evolves to be larger than $\pi/2$, the atoms go from stimulated absorption to stimulated emission resulting in the large emission peaks in the probe at around 2 ps in Fig. 7.4. The emission is peaked as the atom-field phase goes through π. Note that the change from absorption to emission does not result from a population inversion ($\rho_{22} < \rho_{11}$) and it is not driven by the probe pulse advancing the phase between the two states but rather the coupling pulse. As the atom-field phase advances to 2π, the atoms switch back to stimulated absorption. However, as the probe pulse going into the sample has turned off by this time, there is no field to absorb and thus the atoms emit a field which is simply π out of phase with the initial probe pulse. This highlights the fact that stimulated absorption can be regarded as emission of a field out of phase with the applied field. As the atom-field phase again advances by π, the sign of the emitted field changes again. Finally, as the population of the excited state goes to zero and the coupling pulse turns off, the atoms stop emitting. Note that the modulations seen in the calculation of the probe pulse envelope shown in Fig. 7.4 are not observed in the measurement shown in Fig. 7.1 because the cross correlation with the longer coupling pulse washes them out.

The oscillations of the probe pulse field envelope due to coupling-pulse-driven modulated atomic emission explains the reshaping of the probe pulse spectrum that we measure and calculate. The emission peaks near the edges of the probe pulse spectrum result from rapid oscillations in the probe transition coherence. These oscillations are dictated by the evolution of the atom-field phase, which is driven by the coupling pulse. In this sense, the atoms can be regarded as an ultrafast phase modulator driven by the coupling pulse, which can be tailored by our pulse shaper. The transparency, absorption and gain features in Fig. 7.3 thus have a very simple explanation in terms of the atom-field phase advance as driven by the coupling pulse. Furthermore, one can imagine controlling or switching the probe pulse by tailoring the coupling

pulse Rabi frequency as a function of time [93–95]. This interpretation is well suited to ultrafast implementations of EIT, which involve time-dependent Rabi frequencies much larger than the natural linewidth of the transitions in question. In comparing this picture with the traditional frequency domain approach, we note that interference between red and blue detuned dressed states, which is a hallmark of EIT, is still present in our experiments, although it is not playing a crucial role because the Rabi frequency of the coupling field is much larger than the linewidth of the probe transition. This means that the transparency at the transition frequency is mostly based upon Stark shift driven detuning rather than interference between dressed states. The absorption and re-emission of the probe pulse also explains the delay of the probe relative to the coupling we observe in our measurements. It is natural that the probe pulse is delayed relative to the coupling pulse in passing through the sample since the atoms are all initially in the ground state and so the probe pulse experiences the large dispersion associated with an absorption line. Since the coupling laser couples two states which are not populated, it does not experience any dispersion and travels close to the speed of light in vacuum.

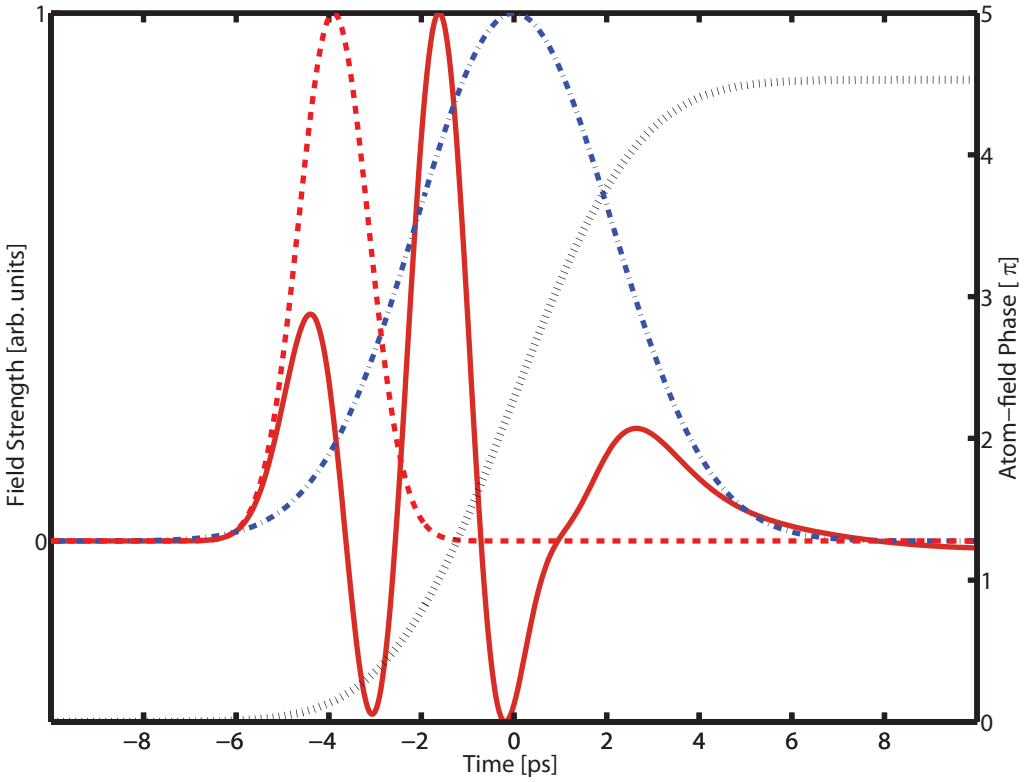

Figure 7.4: Calculated probe and coupling fields and the atom-field phase given by (7.3). The red-dashed and red-solid lines show the calculated probe pulse envelope before and after the cell, respectively. Both curves are normalized to their peak values. The black-dotted line is the atom-field phase, $\alpha(t)$. The blue-dashed-dot line is the normalized coupling pulse.

Chapter 8

Strong Field Control of Stimulated Emission

8.1 Introduction

In the final chapter of this thesis, we apply the method of closed-loop feedback to control stimulated emission from pairs of atomic/molecular species instead of spontaneous emission as in previous chapters. With an eye towards microscopy, standoff detection and other applications, some coherent control experiments have focused on discriminating between multiple atomic or molecular systems [96–99]. While control over target state preparation and discrimination between excitation of multiple samples has been demonstrated in a wide variety of systems, the control yields are typically modest, with control factors on the order of 10 or less. However, it has been shown that stimulated emission can lead to significant enhancement of single atom or molecule control yields [30], [1]. In this chapter we'll show how stimulated emission, in conjunction with coherent control over multi-photon absorption, can lead to almost perfect discrimination between two dye molecules in solution, whereas control over fluorescence in these same molecules yields a control factor of about 2 [96]. As liquid-phase control experiments have proven difficult to interpret [100–102], we also present control results on selective two-photon absorption driven superfluorescence in separate atomic vapors. In the atomic case, the light-matter interaction is well understood [15, 64] and we demonstrate explicitly how the large discrimination in the superfluorescence yields is driven by the single atom dynamics.

[1] In using the phrase 'single atom or molecule control' we refer to control over an ensemble of atoms or molecules in which each atom or molecule acts independent of the others

8.2 Experiment

The shaped laser pulses were split into two arms, with each arm focused to separate atomic or molecular samples. For the experiments with atomic samples, one arm contained a heated glass cell with Rubidium vapor at the focus and the other contained a Sodium heat pipe oven at the focus. Both fluorescence and superfluorescence (SF) were collected from the excited atoms, where fluorescence from the center of the heat pipe / cell was collected at 90^o with respect to the beam propagation direction collected onto a photomultiplier tube (PMT). Interference filters were used to isolate specific transitions (the $3p-3s$ transition in Na and the $6p-5s$ transition in Rb). Stimulated emission from the atoms (in the forward direction) was collected with two separate photodiodes (PD) and combined onto one cable using a signal combiner for ease of digitization. All signals were acquired by a digital oscilloscope mounted in a computer. The Na signal was delayed with a long cable in order to distinguish between the two signals on the oscilloscope. The experiments involving dyes in liquid phase used the same focal geometry with the solutions placed in glass cells at room temperature. We carried out closed-loop learning control experiments in order to maximize the discrimination between the atom and dye-molecule pairs, as well as parameterized pulse shape scans, in order to highlight the relationship between the spontaneous and stimulated emission yields.

8.3 Results

Earlier work has demonstrated that the forward emission from our ensemble of Na atoms is superfluorescence (SF) [30]. This was established via measurements of the pulse duration, coherence, delay relative to the drive pulse, the absence of backward emission, and comparisons between our measurements and numerical integration of the Maxwell-Bloch equations. In Rb, we also observed an absence of backward emission and performed measurements of the forward scattered intensity as a function of density in order to confirm that the emission was SF. Figure 8.1, and its inset, show the stimulated emission yield on the $6p-5s$ transition as a function of density. The inset shows an enlargement for low densities where the forward emission varies quadratically with density (a quadratic fit is shown along with the data). Combined with the absence of backwards emission, this suggests the light is neither Amplified Spontaneous Emission (ASE) or parametric wave mixing in the Rb sample.

We performed two separate learning control experiments with the atomic samples. We aimed to maximize the Rb/Na SF yield in one experiment and

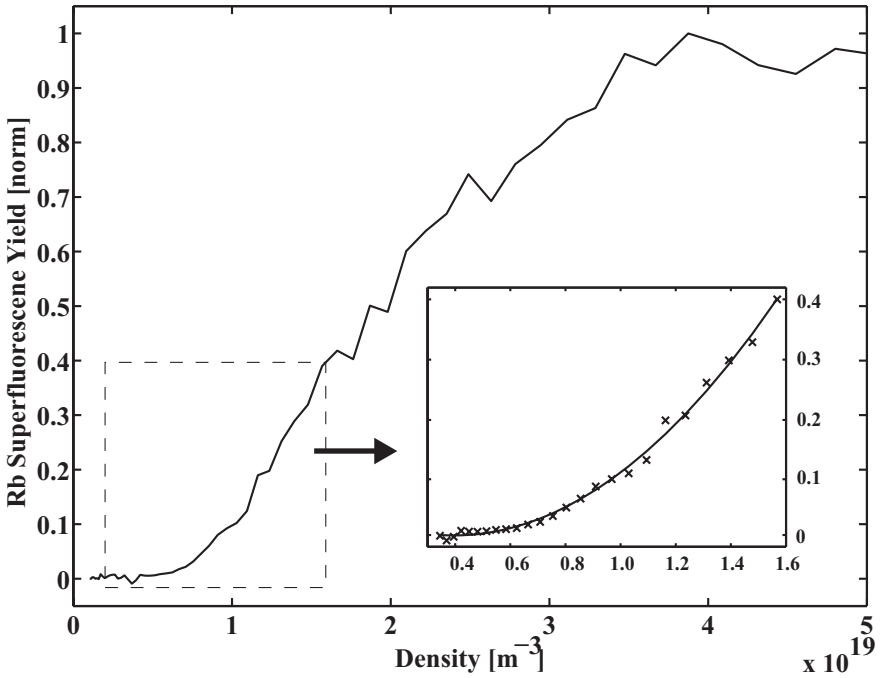

Figure 8.1: Rubidium superfluorescence. The outer figure shows Rubidium superfluorescence ($6p - 5s$) yield as a function of density. The inset shows the superfluorescence yield as a function of density for low densities (the region in the dashed box) along with a quadratic fit. We used a pulse energy of approximately 45 μJ for the measurement.

maximize Na/Rb SF yield in another. The control factor (explained below) is then the product of these two optimal ratios. The results are shown in Fig. 8.2. In Fig. 8.2, the signal (both solid and dashed curves) starting at ∼0 ns is SF from Rb, while the signal just before 250 ns is SF from Na. Here, the solid curve shows the signal for a pulse shape designed to maximize Na/Rb and the dashed curve shows the signal for another pulse shape designed to maximize Rb/Na. The inset shows the relevant atomic structure for both atoms where we measure light from the transition corresponding to the blue line in Rb ($6p - 5s$) and the orange line in Na ($3p - 3s$). The duration of the signals is determined by the capacitance of the large aperture photodiodes, which we used for the measurements in order to digitize them without sampling errors, where the sampling rate of our PC-mounted oscilloscope is 500 MHz.

For the dye experiments, we used methanol solutions of the same two dyes that were used in earlier control experiments which used the spontaneous emission yield for feedback: DCM (4-dicyanomethylene-2-methyl-6-p-dimethylaminostyryl-4H-pyran) and Ruthenium $[Ru(dpb)_3](PF_6)_2$ (dpb is 4,4'-diphenyl-2,2'-dipyridine) [96]. The dye solutions were held in cells approximately 5.5 cm long. The normalized single-photon absorption and emission spectra for DCM and $[Ru(dpb)_3]^{2+}$ are shown in Fig. 8.3. Both DCM and $[Ru(dpb)_3]^{2+}$ have overlapping absorption spectra from 400 nm to 600 nm, requiring two photons to be absorbed from our laser centered at 780 nm. Figure 8.4 shows the stimulated emission spectra for DCM and $[Ru(dpb)_3]^{2+}$. The stimulated emission spectra are very similar to each other, centered at the same wavelength as the emission spectra for the dyes and somewhat narrower than the emission spectra shown above, as expected. We observed some evidence of continuum generation in the dye samples, which we suspect seeded the stimulated emission from the two-photon excited dye molecules. This is consistent with previous two-photon driven lasing measurements [103].

Fig. 8.5 shows the results for selective excitation in DCM and $[Ru(dpb)_3]^{2+}$. The control goals were to maximize the DCM/$[Ru(dpb)_3]^{2+}$ and $[Ru(dpb)_3]^{2+}$/DCM stimulated emission yields, respectively, where we collect the whole stimulated emission spectrum with the photo diodes. The pump laser light was filtered out with a short pass filter. The solid curve shows the signal for a pulse shape designed to maximize DCM/$[Ru(dpb)_3]^{2+}$ and the dashed curve shows the signal for a pulse shape designed to maximize $[Ru(dpb)_3]^{2+}$/DCM. The signal starting close to 0 ns represents $[Ru(dpb)_3]^{2+}$ and the signal just after 150 ns represents DCM. In the case of a transform limited pulse, both dyes gave a similar stimulated emission yield.

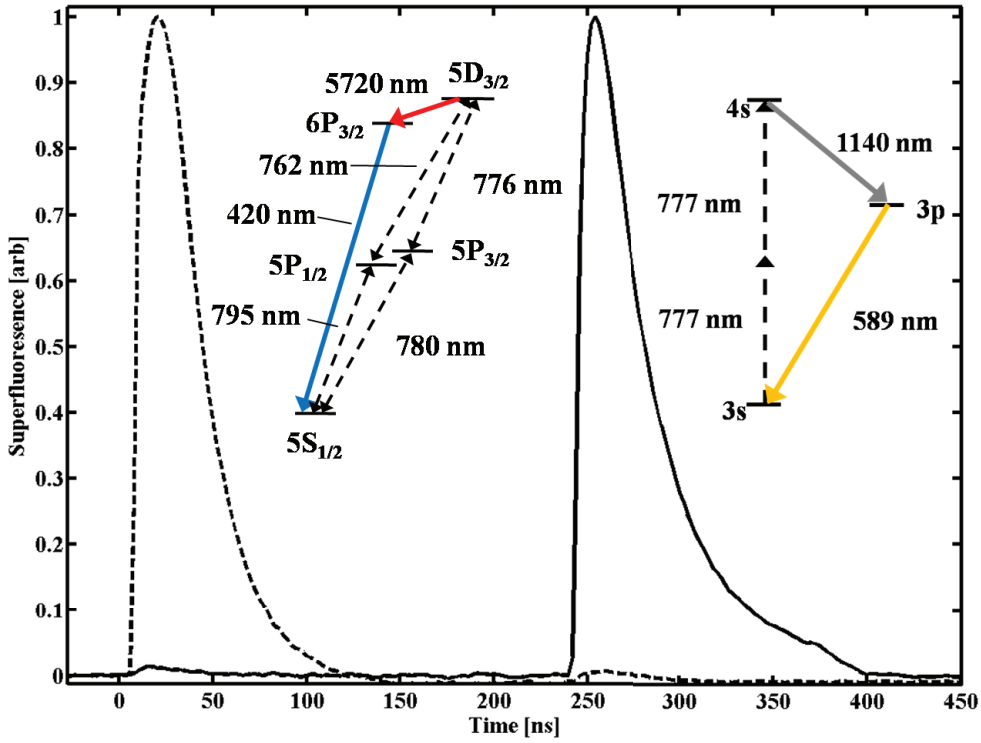

Figure 8.2: Normalized control results for selectivity between Rb and Na stimulated emission. The solid curve represents a pulse designed to maximize Na/Rb and the dashed curve represents a pulse designed to maximize Rb/Na. The signal starting at $\sim$ 0 ns represents Rb and that at $\sim$ 250 ns, Na. The insets show the atomic level structure, where the blue line is the lasing we measure in Rb and the orange line is the lasing we measure in Na. The pulse energies were approximately 170 μJ for Na and 45 μJ for Rb.

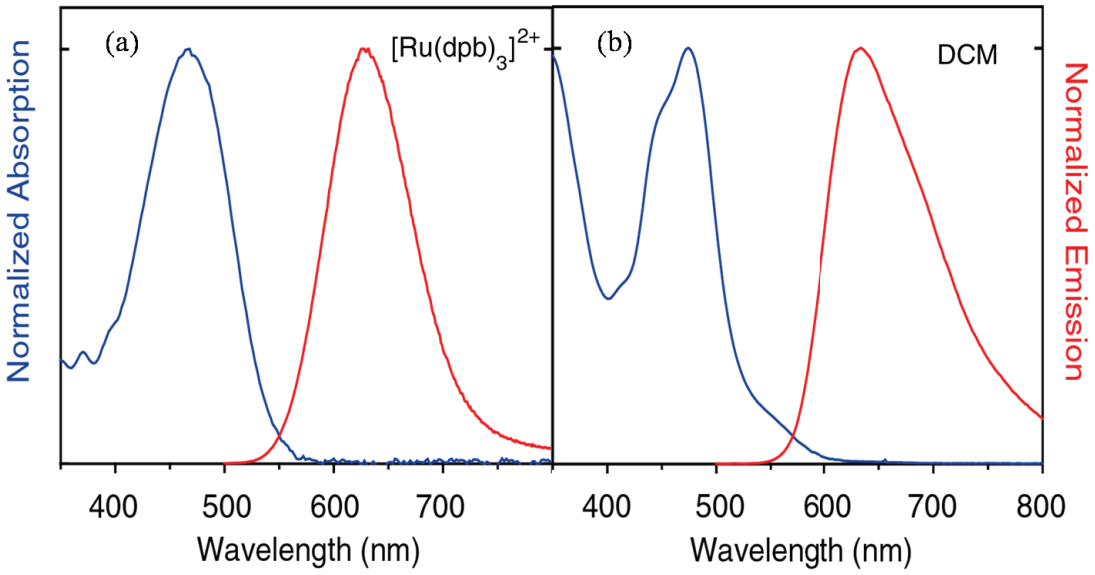

Figure 8.3: Single-photon absorption and emission spectra for $[Ru(dpb)_3]^{2+}$ (panel (a)) and DCM (panel (b)). The blue curve represents absorption and the red curve represents emission. Data courtesy of Niels Damrauer.

8.4 Discussion

Shaping the drive pulse in our experiments allows for the production of a strong forward emission from one sample while almost completely suppressing emission from the other. In terms of selectivity between two samples, we feel it is useful to describe the result in terms of a control factor which accounts for selectivity in both directions and gives a measure of the maximum discrimination possible. In both the atomic and molecular cases, the control factor we consider (the product of the stimulated emission yield ratios for the two control experiments - i.e., $\max(Na/Rb)$ x $\max(Rb/Na)$, or $\max(\text{DCM}/[Ru(dpb)_3]^{2+})$ x $\max([Ru(dpb)_3]^{2+}/\text{DCM})$) is greater than 10^4, even though the control factor for the same molecules when optimizing spontaneous emission ratios is $\sim$ 2 [96]. The control ratio in either direction in both experiments was about 100:1 (limited largely by signal to noise), yielding a control factor of about 10^4. If we were to simply quote the control ratio possible in either direction, then this could mask a lack of control in the other direction and it would not convey the discrimination possible with two different pulse shapes.

The control we observe in Na vs Rb exploits the different electronic structure of the two atoms. Based on these results alone, one might ask whether an intermediate resonance, such as the $5p$ state in Rb, is required to exert signif-

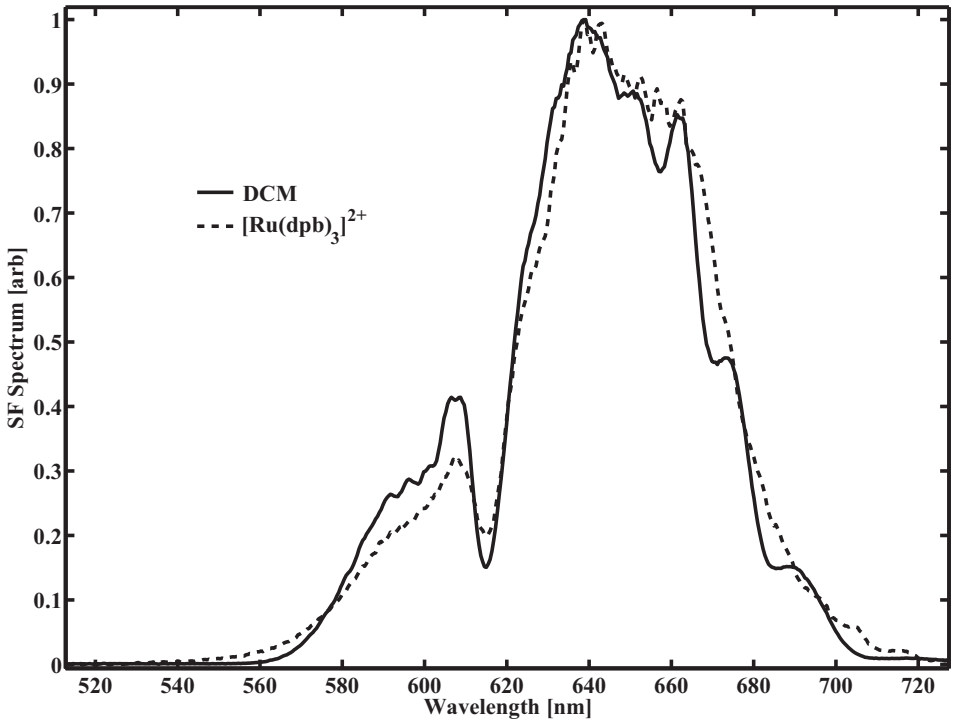

Figure 8.4: Normalized superfluorescence spectra from the two-photon absorbing dyes for an unshaped pulse. The solid curve represents emission from DCM and the dashed curve represents emission from $[Ru(dpb)_3]^{2+}$.

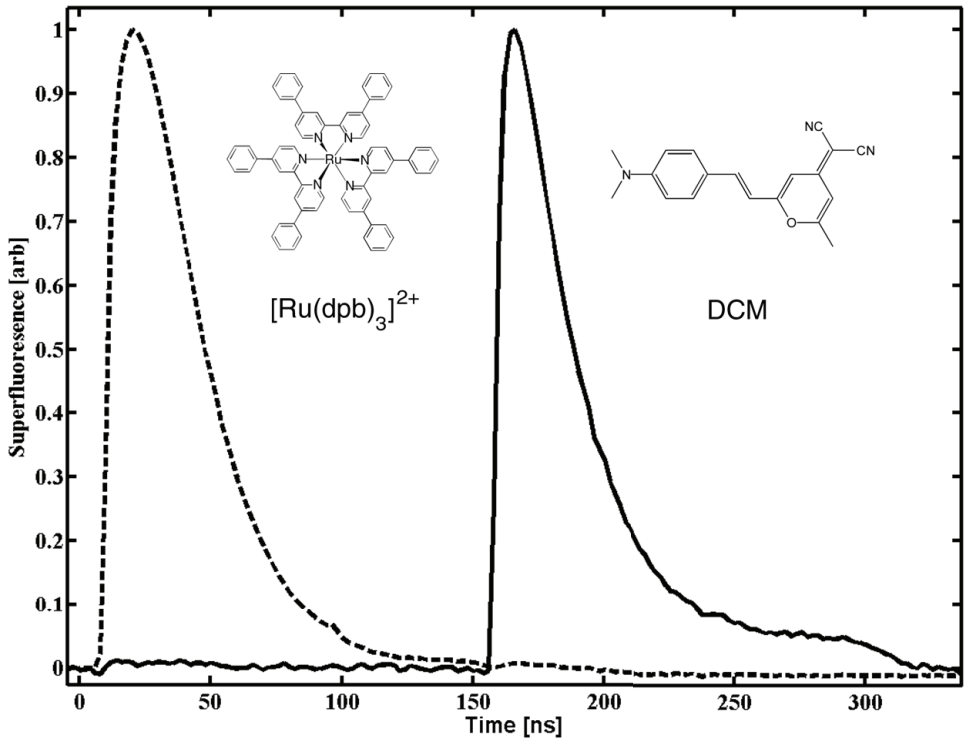

Figure 8.5: Normalized control results for selectivity between DCM and $[Ru(dpb)_3]^{2+}$.The solid curve represents a pulse designed to maximize DCM/$[Ru(dpb)_3]^{2+}$ and the dashed curve represents a pulse designed to maximize $[Ru(dpb)_3]^{2+}$/DCM. The signal starting at $\sim$ 0 ns represents $[Ru(dpb)_3]^{2+}$ and that at $\sim$ 150 ns, DCM. The insets show the two chemical structures of the molecules.

icant control in competition with another non-resonant two-photon absorbing systems. The experiment with the dyes suggests that this is not the case, since the two absorption spectra are very similar between 400 nm and 800 nm (with no absorption at all near 780 nm), and we expect near resonant enhancements to play a more important role than states that are far from resonance.

One might also ask whether the control we observe in the dye molecules is a result of selective seeding of the stimulated emission via nonlinear interactions between the pump pulse and the solvent molecules [100, 101]. Our measurements of the stimulated emission spectra suggest that this is not the case, as the two measured spectra for the forward emission (shown in Fig. 8.4 for and unshaped pulse) overlap quite closely , making it very difficult to selectively seed one emission while suppressing the other.

In order to demonstrate how the dramatic selectivity is based on control over single atom/molecule dynamics enhanced by stimulated emission, we measured both the spontaneous and stimulated emission from the atomic ensembles as a function of pulse shape for a simple pulse shape parameterization, with a spectral phase given by:

$$\Phi(\omega) = \frac{\pi}{2} sin(\beta\omega + \delta). \tag{8.1}$$

This periodic spectral phase was chosen because it effectively discriminates between the two samples and has a simple interpretation for the case of sodium, where the two-photon absorption is not resonantly enhanced. In this case, any antisymmetric spectral phase leads to constructive interference between competing pathways to the final state, where as a symmetric spectral phase leads to destructive interference and a suppression of interference [104]. The excitation of Rb is affected by the intermediate resonances, which makes the pulse shape dependence of the excitation more complicated [12]. (We note here that the spectrum of our laser was not centered at 777 nm, the center of the two-photon resonance in Na, and therefore $\delta = 0$ does not imply the spectral phase is antisymmetric around the two-photon resonance).

Figure 8.6 shows fluorescence and superfluorescence for both Rb and Na as a function of energy and δ. Panels (a) and (b) show superfluorescence and fluorescence, respectively, from Rb; panels (c) and (d) show the superfluorescence and fluorescence, respectively, from Na. We note that the superfluorescence as a function of energy and δ for each atom follows the fluorescence closely - i.e., the superfluorescence yield is driven by the single atom-field dynamics. In addition to demonstrating that the SF yield follows the single atom excitation, this pulse shape parameterization demonstrates how a modest single-atom discrimination can lead to a dramatic discrimination in the SF yields. Fig. 8.7

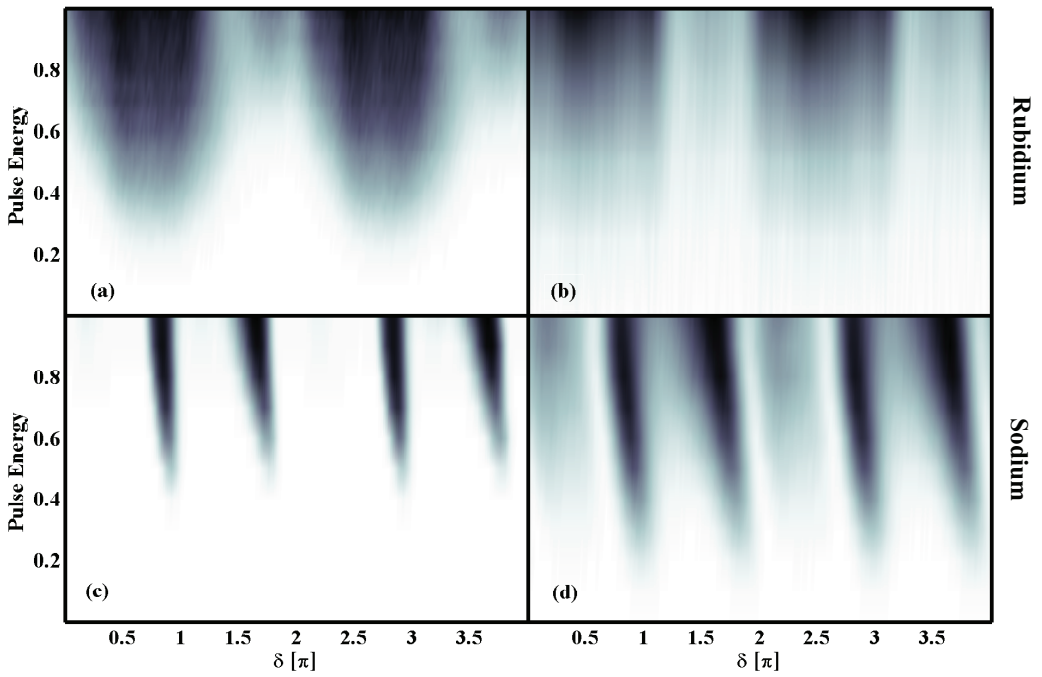

Figure 8.6: Measurements of the fluorescence and superfluorescence for both Rb and Na as a function of energy and the phase-offset parameter δ. Panels (a) and (b) show Rb superfluorescence and fluorescence, respectively, where the maximum pulse energy is approximately 45 μJ. Panels (c) and (d) show Na superfluorescence and fluorescence, respectively, where the maximum pulse energy is approximately 170 μJ.

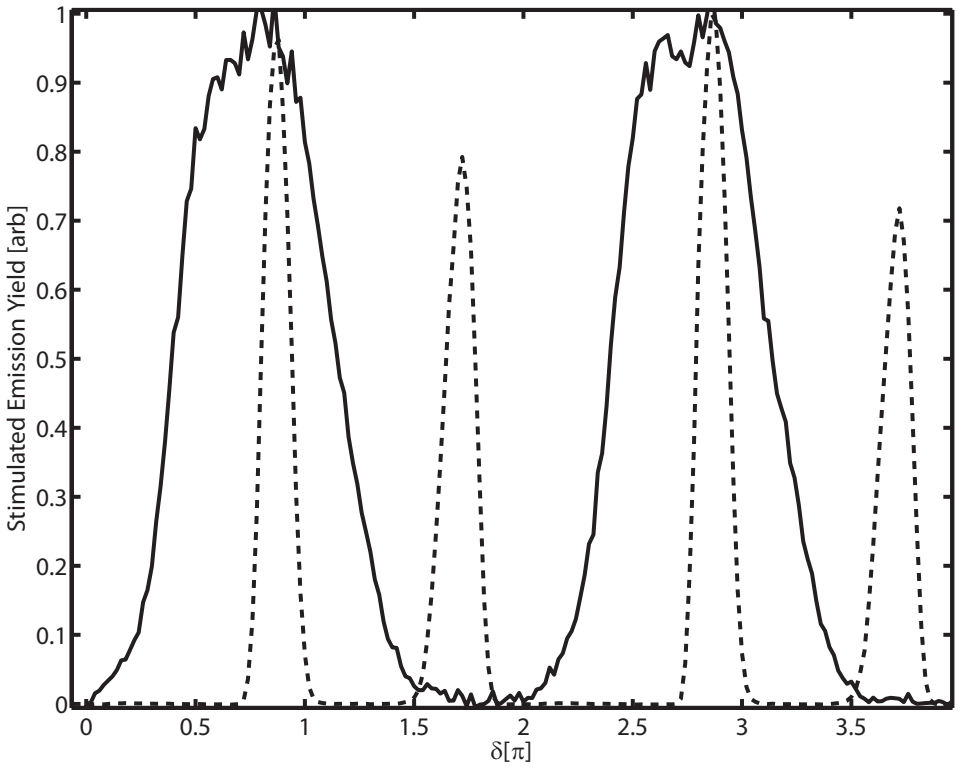

Figure 8.7: Normalized lineouts of Fig. 8.6. The solid curve represents superfluorescence for Rb and the dashed curve for Na. The yields are normalized and represent different energies.

shows the Rb and Na SF yield as a function of δ at a fixed energy (not the same energy for the two different atoms). The dashed curve represents Na SF and the solid curve Rb SF. Controlling δ yields a substantial contrast between the superfluorescence for one atom vs another.

We measured the optimal pulses for a few of the GA results in atomic Rb and Na, shown in Fig. 8.8. Although it is difficult to interpret the dynamics for the optimal pulses because of volume averaging related to spatial intensity variation [64, 105], we note a few features. Panels (a) and (b) show measured Wigner distributions [71] for a pulse designed to maximize Na/Rb SF yield and a pulse designed to maximize Rb/Na SF yield, respectively. Panels (c) and (d) represent the pulse intensity and phase in time of (a) and (b). Trying to suppress the Rb SF and keep the Na SF yielded a pulse with a double structure, whereas trying to suppress the Na SF and keep the Rb SF yielded a pulse with just a single peak. Both pulses are of order one hundred femtoseconds, exhibit a smoothly varying phase, and have a relatively simple temporal structure,

indicating that the discrimination is quite sensitive to the drive laser pulse shape.

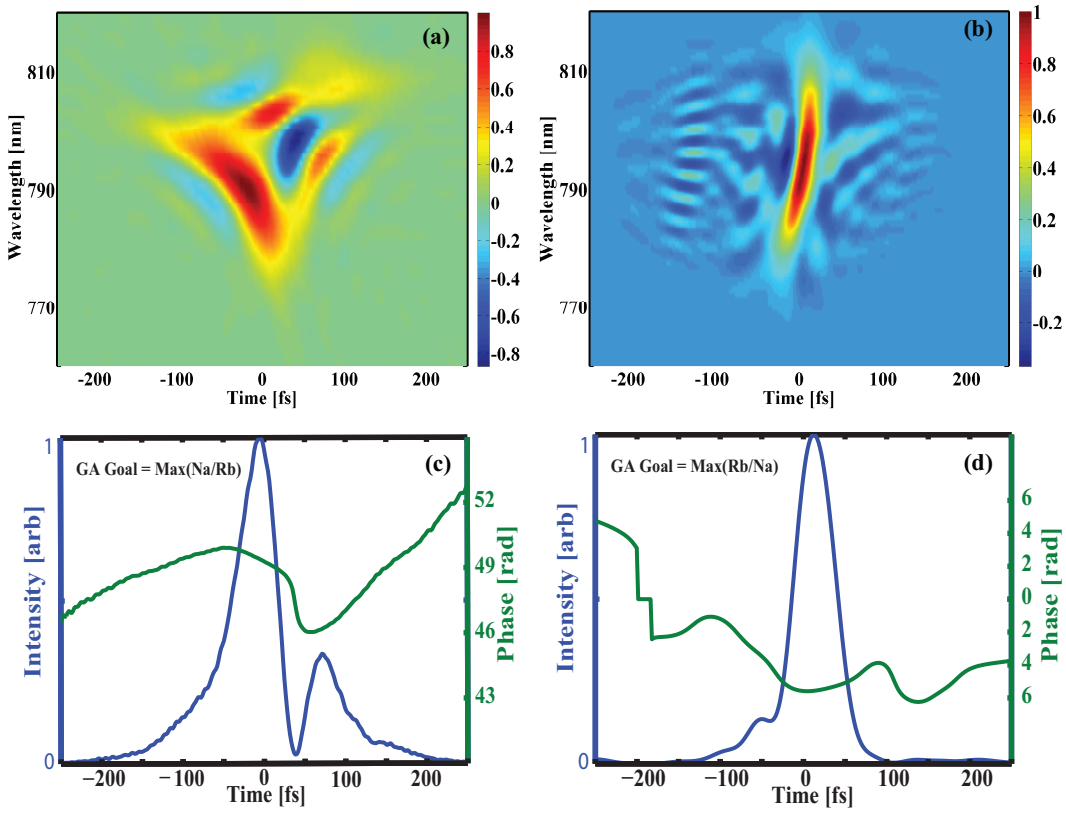

Figure 8.8: Optimal Pulses. Panels (a) and (b) show measured Wigner distributions for a pulse designed to maximize Na/Rb SF yield (corresponding to the solid curve in Fig. 8.2) and a pulse designed to maximize Rb/Na SF yield (corresponding to the dashed curve in Fig. 8.2), respectively. Panels (c) and (d) represent the temporal intensity and phase associated with (a) and (b), respectively.

Chapter 9

Conclusions

In this thesis, we explored strong field control of multilevel systems using shaped ultrafast pulses and have shown that numerous control possibilities exist in the strong field limit. In chapter 5 we demonstrated multiphoton population inversion of a three-level atomic system using a single shaped laser pulse. The optimal pulse shape was discovered inside a learning control loop, further illustrating that optimization algorithms can be a useful tool for designing optimal pulses. The optimal pulses yielded an order of magnitude gain over the population transfer for an unshaped laser pulse, and we measured the population inversion using a combination of fluorescence and superfluorescence. The physical mechanism underlying the inversion was identified by performing parameterized pulse shape scans based on the optimal pulses and numerical integration of the Shrödinger equation. The pulse shape dependence of the final state population illustrates the benefits of sequential vs STIRAP like population transfer for a fixed pulse energy. In the case of multiphoton population transfer with a single ultrafast laser pulse, there are no decoherence mechanisms on the timescales of the atom-field interaction and thus no disadvantage to populating intermediate states. Population transfer under this scheme is simple (only one laser beam), flexible (the pulse shape can be changed easily) and an effective (can be used to produce a population inversion) route to population transfer when multiphoton transitions are involved. Furhermore, we showed that scaling of the adiabaticity criterion for STIRAP with multiphoton coupling is unfavorable and requires orders of magnitude higher pulse energies than sequential population transfer. Thus, we propose that sequential population transfer through intermediate states can be more effective than STIRAP based schemes when using shaped ultrafast laser pulses for population transfer with multiphoton coupling.

Extending chapter 5 to allow for another atomic level, chapter 6 examined a simple atomic interferometer using a single shaped ultrafast laser pulse to

create and control two pathways between initial and final states. There, we performed and interpreted measurements in both the weak and strong field limits, where the two limits show similar interference, although the character of the interference changes between each case. In the weak field limit where only resonant frequencies are present, the measured interference stems from the two resonant excitation pathways. With the full spectrum present, the measured interference changes largely to between resonant and non-resonant excitation pathways in a given arm of the interferometer. Further, as the field strength increases (depleting substantial ground state population) the measured interference derives from the coherent sum of population transferred by the long pulse with that of the short main pulse and is dictated by the relative phase between the short and long pulses.

Utilizing some of the strong field dynamics understood in chapters 5 and 6, we went on in chapter 7 to show that an atom can be rendered the modulator of an ultrafast pulse. The pump-probe scheme represented an ultrafast analogue of electromagnetically induced transparency (EIT), with probe and coupling pulses generated from a single ultrafast laser pulse in a pulse shaper. Our interpretation of the experimental results yielded a simple time-domain picture of the dynamics leading to transparency and gain in the sample without a population inversion.

Using the same systems as in chapters 5 and 6, chapter 8 explored stimulated emission near threshold in theses systems and demonstrated that an appropriately shaped strong drive pulse can turn modest coherent control yields from spontaneous emission into essentially perfect discrimination between systems via stimulated emission. We achieved this by selective two-photon driven superfluorescence in atomic Rubidium and Sodium and selective two-photon driven stimulated emission in solvated laser dyes with similar single-photon absorption spectra. The shape of an ultrafast drive laser (discovered in a learning control loop) controled which atom/molecule the emission was from. In both cases the control factor was greater than 10^4.

Appendix A

Mathematical Derivations

A.1 Pulse Propagation through a Medium

The results of chapter 7 depend on a quantitative understanding of how the pulse is reshaped in propagating through an atomic medium (Rubidium gas in this case). Therefore, it is crucial to develop a model of how the atomic medium and the pulse interact with one another in a self-consistent picture. That is, we seek to model how the pulse changes the atomic coherence of the Rubidium atoms and in turn how the atomic coherence changes the pulse as it propagates through the atomic gas.

Formally, the probe field that couples the $5s_{1/2} \rightarrow 5p_{3/2}$ ($|1\rangle \rightarrow |2\rangle$) transition can be written as,

$$\mathbf{E_p}(t) = \frac{1}{2}\varepsilon_p(t)e^{-i\omega_p t}\hat{\varepsilon}_p + c.c. \tag{A.1}$$

and the equation for the coupling pulse that connects the $5p_{3/2}$ - 5d ($|2\rangle \rightarrow |3\rangle$) transition written as,

$$\mathbf{E_c}(t) = \frac{1}{2}\varepsilon_c(t)e^{-i\omega_c t}\hat{\varepsilon}_c + c.c. \tag{A.2}$$

The wavelengths for these two transitions are $\lambda_p = 780$ nm and $\lambda_c = 776$ nm. Our system consists of 3 levels coupled by a single photon, which allows us to write the Hamiltonian in an interaction picture as [58],

$$\hat{\mathbf{H}}_\mathbf{I}(t) = -\frac{\hbar}{2}\begin{pmatrix} -2\Delta_P & \Omega_p & 0 \\ \Omega_p & 0 & \Omega_c \\ 0 & \Omega_c & -2\Delta_c \end{pmatrix}. \tag{A.3}$$

where $\Omega_p = \frac{\varepsilon_p(t)\mu_{12}}{h}$ and $\Omega_c = \frac{\varepsilon_c(t)\mu_{23}}{h}$, and Δ_P and Δ_c are the detunings

between the probe and coupling transitions, respectively. In our case, the coupling pulse and the probe pulse are both resonant with the $|2\rangle \rightarrow |3\rangle$ and $|2\rangle \rightarrow |1\rangle$ transitions, respectively. Then $\hat{\mathbf{H}}_{\mathbf{I}}(t)$ reduces to,

$$\hat{\mathbf{H}}_{\mathbf{I}}(t) = -\frac{\hbar}{2}\begin{pmatrix} 0 & \Omega_p & 0 \\ \Omega_p & 0 & \Omega_c \\ 0 & \Omega_c & 0 \end{pmatrix}. \tag{A.4}$$

For the ensemble of atoms in our cell, we use the von Neumann Equation to derive time evolution of the density matrix,

$$i\hbar\dot{\rho}(t) = [\hat{H}, \rho] \tag{A.5}$$

where,

$$\rho = \begin{pmatrix} \rho_{11} & \rho_{12} & \rho_{13} \\ \rho_{21} & \rho_{22} & \rho_{23} \\ \rho_{31} & \rho_{32} & \rho_{33}. \end{pmatrix} \tag{A.6}$$

Carrying out the necessary matrix multiplication we can write the equations of motion governing the states as,

$$\dot{\rho}_{11} = -\frac{i}{2}(\Omega_p\rho_{12} - \Omega_p^*\rho_{12}) \tag{A.7}$$

$$\dot{\rho}_{12} = -\frac{i}{2}(\Omega_p\rho_{22} - \rho_{11}\Omega_p - \rho_{13}\Omega_c^*) \tag{A.8}$$

$$\dot{\rho}_{13} = -\frac{i}{2}(\Omega_p\rho_{23} - \rho_{12}\Omega_c) \tag{A.9}$$

$$\dot{\rho}_{21} = -\frac{i}{2}(\Omega_p^*\rho_{11} + \Omega_c\rho_{31} - \rho_{22}\Omega_p^*) \tag{A.10}$$

$$\dot{\rho}_{22} = -\frac{i}{2}(\Omega_p^*\rho_{12} + \Omega_c\rho_{32} - \rho_{21}\Omega_p - \rho_{23}\Omega_c^*) \tag{A.11}$$

$$\dot{\rho}_{23} = -\frac{i}{2}(\Omega_p^*\rho_{13} + \Omega_c\rho_{33} - \rho_{22}\Omega_c) \tag{A.12}$$

$$\dot{\rho}_{31} = -\frac{i}{2}(\Omega_c^*\rho_{21} - \rho_{32}\Omega_p^*) \tag{A.13}$$

$$\dot{\rho}_{32} = -\frac{i}{2}(\Omega_c^*\rho_{22} - \rho_{31}\Omega_p - \rho_{33}\Omega_c^*) \tag{A.14}$$

$$\dot{\rho}_{33} = -\frac{i}{2}(\Omega_c^*\rho_{23} - \rho_{32}\Omega_c) \tag{A.15}$$

$$\tag{A.16}$$

Now let's consider propagation of the coupling and probe pulses. Starting with Maxwell's equations, we can write the propagation of an electric field as

$$\left(\nabla^2 - \frac{1}{c^2}\frac{\partial^2}{\partial t^2}\right)\mathbf{E}(r,t) = \mu_0 \frac{\partial^2}{\partial t^2}\mathbf{P}(r,t), \tag{A.17}$$

where μ_0 is the permeability of free space, $\mathbf{E}$ is the electric field and $\mathbf{P}$ is the polarization of the medium through which the electric field propagates. The left-hand side can be factored from a difference of squares to read,

$$\left(\nabla + \frac{1}{c}\frac{\partial}{\partial t}\right)\left(\nabla - \frac{1}{c}\frac{\partial}{\partial t}\right)\mathbf{E}(r,t). \tag{A.18}$$

Let us note a few properties of the fields. First, we can neglect both transverse coordinates because we spatially filter the beams before coupling into the spectrometer. This allows us to neglect the transverse coordinates x and y, while keeping the z coordinate. Also, the pulse envelope does not change significantly during an optical cycle, so it's envelope is slowly varying. Likewise, the field along the propagation axis is slowly changing. Formally this implies,

$$\frac{\partial \varepsilon(z,t)}{\partial t} << \omega\varepsilon(z,t) \tag{A.19}$$

$$\frac{\partial \varepsilon(z,t)}{\partial z} << k\varepsilon(z,t) \tag{A.20}$$

$$\frac{\partial P(z,t)}{\partial t} << \omega P(z,t) \tag{A.21}$$

$$\frac{\partial P(z,t)}{\partial z} << kP(z,t), \tag{A.22}$$

$$\tag{A.23}$$

where ω and k represent the frequency and wave vector of the pulse. Noting that,

$$\frac{\partial \varepsilon(z,t)}{\partial t} = \frac{1}{2}\frac{\partial \varepsilon(z,t)}{\partial z}e^{-i\omega t - \imath kz} + \frac{1}{2}\varepsilon(z,t)e^{-i\omega t - \imath kz}(-i\omega) \tag{A.24}$$

$$\frac{\partial \varepsilon(z,t)}{\partial z} = \frac{1}{2}\frac{\partial \varepsilon(z,t)}{\partial z}e^{-i\omega t - \imath kz} + \frac{1}{2}\varepsilon(z,t)e^{-i\omega t - \imath kz}(-ik) \tag{A.25}$$

$$\tag{A.26}$$

we can apply the first part of the factored operator to get,

$$\left(\nabla^2 - \frac{1}{c^2}\frac{\partial^2}{\partial t^2}\right)\mathbf{E}(r,t) \rightarrow \left(\frac{\partial}{\partial z} + \frac{1}{c}\frac{\partial}{\partial t}\right)(-2\imath k\mathbf{E}(r,t)). \tag{A.27}$$

Now consider the right-hand side of the propagation equation. The polarization follows the same slowly-varying envelope approximations that the field does. This allows us rewrite the RHS as,

$$(-\imath\omega)\frac{\partial P}{\partial t}\mu_0 \tag{A.28}$$

which yields a reduced 1-D Maxwell propagation equation,

$$\left(\frac{\partial}{\partial z}+\frac{1}{c}\frac{\partial}{\partial t}\right)\mathbf{E}(z,t)) = \frac{1}{2\epsilon_0 c}\frac{\partial \mathbf{P}(\mathbf{z},\mathbf{t})}{\partial t}. \tag{A.29}$$

Now let us deal with the quantum mechanical interpretation of the polarization. From [106], the electronic polarization of a medium with a single atomic species is,

$$\mathbf{P}_T = N < \mathbf{p} >, \tag{A.30}$$

where $< \mathbf{p} >$ is the dipole moment of the atom in the medium, in our case Rb, and N is the density of the medium. Thus, we write the electric polarization as,

$$\mathbf{P}_T = N < \Psi|\hat{\mu}|\Psi > \tag{A.31}$$

$$P_p(t) = N < \Psi_p(t)|\hat{\mu}|\Psi_p(t) > e^{\imath\omega_p t} \tag{A.32}$$

$$P_c(t) = N < \Psi_c(t)|\hat{\mu}|\Psi_c(t) > e^{\imath\omega_c t} \tag{A.33}$$

As previously mentioned, our system consists of 3 levels coupled by a single photon, so let us make the following labels: 5s $\rightarrow |1>$, 5p $\rightarrow |2>$, 5d $\rightarrow |3>$. Then, the wavefunctions can be written as,

$$|\Psi_p(t)>= a_1(t)e^{-i\omega_1 t}|1> + a_2(t)e^{-i\omega_2 t}|2> \tag{A.34}$$

$$|\Psi_c(t)>= a_2(t)e^{-i\omega_2 t}|2> + a_3(t)e^{-i\omega_3 t}|3>, \tag{A.35}$$

which allows us to compute the time-dependent polarization due to the probe and coupling pulses as,

$$P_p(t) = N\left(a_1^*(t)a_2(t)e^{-i\omega_{21}t}\mu_{12} + c.c.\right)e^{-i\omega_p t} \tag{A.36}$$

$$P_c(t) = N\left(a_2^*(t)a_3(t)e^{-i\omega_{32}t}\mu_{23} + c.c.\right)e^{-i\omega_p t}. \tag{A.37}$$

Note that in $P_p(t)$ and $P_c(t)$, the complex conjugate terms have factors that go like $\exp(i\omega_{21}t)$ and $\exp(i\omega_{32}t)$. When multiplied by $\exp(i\omega_p t)$ and $\exp(i\omega_c t)$, respectively, we get terms that evolve like $\exp(i(\omega_{21}+\omega_p)t$ and $\exp(i(\omega_{32}+\omega_c)t$. Since ω_p and ω_c are on resonance, $\omega_{21}+\omega_p = 2\omega_p$ and $\omega_{32}+\omega_c = 2\omega_c$.

These terms oscillate at twice the laser frequency and can therefore be dropped (Rotating Wave Approximation). Thus, $P_p(t)$ and $P_c(t)$ take on the simple form,

$$P_p(t) = N\left(a_1^*(t)a_2(t)\mu_{12}\right) \tag{A.38}$$

$$P_c(t) = N\left(a_2^*(t)a_3(t)\mu_{23}\right). \tag{A.39}$$

Lastly, we will take our reduced 1-D Maxwell propagation equation and perform a transformation to a frame local to the pulses. Thus, make the following change of variables: $z = \zeta$ and $t' = t - z/c$. Then, $E = E(z,t)$, $t = t(t',\zeta)$, and $z = z(t',\zeta)$. Therefore,

$$\frac{\partial \varepsilon}{\partial \zeta} = \frac{\partial \varepsilon}{\partial t}\frac{\partial t}{\partial \zeta} + \frac{\partial \varepsilon}{\partial z}\frac{\partial z}{\partial \zeta} \tag{A.40}$$

so that,

$$\frac{\partial}{\partial \zeta} = \frac{\partial}{\partial t}\frac{1}{c} + \frac{\partial}{\partial z}. \tag{A.41}$$

In a local frame, the propagation equation reduces to,

$$\frac{\partial}{\partial z}\mathbf{E}(z,t) = \frac{1}{2\epsilon_0 c}\frac{\partial \mathbf{P}(\mathbf{z},\mathbf{t})}{\partial t} \tag{A.42}$$

and,

$$\frac{\partial}{\partial z}\mathbf{E}_p(z,t) = \frac{i\omega_p N\mu_{12}}{2\epsilon_0 c}\rho_{21}(z,t) \tag{A.43}$$

$$\frac{\partial}{\partial z}\mathbf{E}_c(z,t) = \frac{i\omega_c N\mu_{23}}{2\epsilon_0 c}\rho_{32}(z,t). \tag{A.44}$$

Note, we made use of the fact that the local-frame variables are arbitrary, and can just as well be replaced with z and t. These equations, along with the time evolution of the density matrix, govern the probe and coupling fields as they propagate through the Rubidium vapor. They can be integrated via Euler's method as follows,

$$\Delta E = \Delta z\frac{\partial E}{\partial z}. \tag{A.45}$$

Here, the partial derivative of the field uses the coherences obtained at the previous z position. Solving (A.43) and (A.45) iteratively yields the probe and coupling fields after propagating through the Rubidium vapor.

A.2 Wigner Distribution of a Chirped Pulse

Here, we derive the Wigner distribution [107] of a chirped laser pulse. The Wigner distribution of an electric field can be written as [51]

$$w(t,\omega) = \frac{1}{\pi}\int_{-\infty}^{\infty} d\omega' E^*(\omega + \frac{\omega'}{2})E(\omega + \frac{\omega'}{2})e^{-i\omega' t}, \tag{A.46}$$

where $E(\omega)$ is the electric field in the frequency domain and has the interpretation of a quasi-probability distribution. This representation of the electric field illustrates how the instantaneous frequency of the pulse varies in time. We are interested in the Wigner distribution of a chirped pulse, where a chirped pulse corresponds to the addition of a quadratic spectral phase. Therefore, the electric field of a chirped pulse at any given frequency within the pulse bandwidth is given as

$$E(\omega) = e^{-\alpha\omega^2}e^{-i\beta\omega^2}, \tag{A.47}$$

where $\alpha = 1/\Delta\omega$, $\Delta\omega$ is the frequency bandwidth, and β is the frequency domain chirp rate. Note, we have removed the carrier frequency of the pulse for convenience. Therefore, the Wigner function becomes,

$$w(t,\omega) = \frac{1}{\pi}\int_{-\infty}^{\infty} d\omega' e^{-\alpha(\omega+\omega'/2)^2+i\beta(\omega+\omega'/2)^2} \times e^{-\alpha(\omega+\omega'/2)^2-i\beta(\omega-\omega'/2)]^2}e^{-i\omega' t}. \tag{A.48}$$

Expanding and summing the squares in the arguments of the exponentials and including the factor exp(iω't), we can express the total argument of the exponentials as

$$arg = -2\alpha\omega^2 - \frac{\alpha}{2}[\omega'^2 - i\frac{2}{\alpha}(\beta\omega - t)\omega']. \tag{A.49}$$

By completing the square for the term in brackets, we can re-express total argument of the exponentials, after grouping terms, as

$$arg = -[2\alpha\omega^2 + \frac{1}{2\alpha}(\beta\omega - t)^2] - \frac{\alpha}{2}[\omega' - \frac{1}{\alpha}(\beta\omega - t)]^2. \tag{A.50}$$

Then, the Wigner function becomes

$$w(t,\omega) = \frac{1}{\pi}\int_{-\infty}^{\infty} d\omega' e^{-\frac{\alpha}{2}(\omega'-\frac{1}{\alpha}(\beta\omega-t))^2} \times e^{-[2\alpha\omega^2+\frac{1}{2\alpha}(\beta\omega-t)^2]}. \tag{A.51}$$

Using the identity

$$\int_{-\infty}^{\infty} dx e^{-\alpha x^2} = \sqrt{\frac{\pi}{\alpha}}, \tag{A.52}$$

we can write the Wigner distribution as

$$w(t,\omega) = \sqrt{\frac{2}{\pi\alpha}} e^{-[2\alpha\omega+\frac{1}{2\alpha}(\beta\omega-t)^2]} \tag{A.53}$$

A.3 Rotation of the Hamiltonian by Unitary Transformation

Often it is desirable to transform the Hamiltonian to a form that removes the diagonal elements and places them, in a appropriate way, in the off-diagonal entries, and vice versa. This can be achieved by a unitary transformation. Consider a time-dependent Hamiltonian $H(t)$ and a unitary transformation matrix $U(t)$, where

$$U(t)^{-1} = U^{\dagger}. \tag{A.54}$$

Then, defining $\Psi' = U^{-1}\Psi$, the Time-Dependent Schrodinger Equation (TDSE) can be written as,

$$i\hbar\frac{\partial U(t)\Psi'}{\partial t} = i\hbar\left(U(t)\frac{\partial\Psi'}{\partial t} + \frac{\partial U(t)}{\partial t}\Psi'\right) = H(t)U(t)\Psi'. \tag{A.55}$$

Rearranging terms and multiplying both sides by $U(t)^{-1}$, the TDSE is recast as

$$i\hbar\frac{\partial\Psi'}{\partial t} = U(t)^{-1}H(t)U(t) - i\hbar U(t)^{-1}\dot{U(t)}\Psi'. \tag{A.56}$$

Therefore, the transformed Hamiltonian is given as

$$H(t)' = U(t)^{-1}H(t)U(t) - i\hbar U(t)^{-1}\dot{U(t)}. \tag{A.57}$$

Let's apply this to a simple 2×2 Hamiltonian with time-dependent entries

$$H(t) = \begin{pmatrix} H_{11}(t) & H_{12}(t) \\ H_{21}(t) & H_{22}(t) \end{pmatrix}. \tag{A.58}$$

where we require $[H'(t)]_{ii} = 0$ in (A.57) for i = 1,2. We make the ansatz that U(t) has the form,

$$U(t) = \begin{pmatrix} e^{i\delta_1(t)} & 0 \\ 0 & e^{i\delta_2(t)} \end{pmatrix}. \tag{A.59}$$

Then, carrying out the multiplication in (A.57), we find that H'(t) becomes,

$$H'(t) = \begin{pmatrix} H_{11}(t) + \delta_1(t) & H_{12}(t)e^{i(\delta_2(t)-\delta_1(t))} \\ H_{21}(t)e^{-i(\delta_2(t)-\delta_1(t))} & H_{22}(t) + \delta_2(t) \end{pmatrix}. \tag{A.60}$$

Therefore, if we require that $H'_{ii}(t) = 0$, then $H_{ii}(t) = -\dot{\delta}(t)_i$. Given that $\dot{U}_{ii}(t) = i\dot{\delta}_i(t)U_{ii}(t)$ for i = 1,2, then

$$U_{ii}(t) = e^{-i\int_{-\infty}^{t} dt' H_{ii}(t')} \tag{A.61}$$

with the initial condition that $H(t \to -\infty)_{ii} \to 0$. Thus, U(t) takes on the form,

$$U(t) = \begin{pmatrix} e^{-i\int_{-\infty}^{t} dt' H_{11}(t')} & 0 \\ 0 & e^{-i\int_{-\infty}^{t} dt' H_{22}(t')} \end{pmatrix}. \tag{A.62}$$

It is straight forward to extend this treatment to the 3×3 and 4×4 Hamiltonians used in this thesis.

Appendix B

Codes Used for Numerical Simulation

All of the numerical calculations presented in this thesis were performed using MATLAB 7.1. Source code for several of the simulations are given blow.

B.1 Simulation of Space-time Coupling in a Pulse Shaper

```
tic
%Global Constants ------------------------------------
% All lengths are in mm unless otherwise specified. All
   times are fs, all freq fs^-1
c = 3.0*10^8;          % speed of light (m/s)
a = 1/(671);           % groove spacing (mm)
lambda = 780e-9;       % central wavelength (m)
f0=c/lambda/1e15;      %central frequency (fs^-1)
theta_i = asin(lambda/(2*(a/1000)));  % incident angle
   for littrow condition
theta_d = -theta_i;  % diffracted angle for littrow,
   both in radians

p = 1;                 % diffraction order
beta = (2*pi*p)/(a*cos(theta_d)*(2*pi*f0)); % in (fs/mm)
    1st grating
beta_prime =(2*pi*p)/(a*cos(theta_i)*(2*pi*f0)); %
   second grating
```

```
k0 = (2*pi/780e-6); %central wave vector (rad/mm)
n = 1.5;            %index of the lens
d = 0;              %lens thickness (mm)
fl = 750;           %focal length (mm)
z = fl;             %propagation distance

% Input field ------------------------------
delta_X = 0.01;              %step size in x (mm)
delta_T = 8.0;               %step size in t (fs)
fwhm_x = 1.9; gamma = 1.9; fwhm_t = 30.5;
tau = (fwhm_t/2)*sqrt(2/log(2));%for field amplitude (fs
    )
sigma = (fwhm_x/2)*sqrt(2/log(2));%for field amplitude (
   mm)

N_X = 30.0;                  %spatial extent of x (mm)
N_T = 400*30*sqrt(2)/2;      %temporal extent of t (fs)

% Field after first grating ----------------

[X,T] = meshgrid(-N_X:delta_X:N_X, -N_T:delta_T:N_T); [m
    ,n] =
size(T);

scale  = 0.0052;
%x = [-624:655]*scale;
Ex = load('V:\2006 12 18 A\mode measurements\mode out of
amp\ExAverageMode7');

E = repmat(Ex,m,1); clear x; clear Ex;

xx = X(1,:); %for use as a plotting axis
E_grating1 = E.*(exp(-((T-beta*X)/tau).^2));
E_grating1FT =ifftshift(fft2(E_grating1));

clear X clear T clear E_grating1 clear E

%Propagation from grating 1 to lens 1-----------
fact = 2*pi; % needed to have units of radians
[xi,f]=
```

```
meshgrid([-1/(2*delta_X):1/2/N_X:1/(2*delta_X)],[-1/(2*
    delta_T):1/2/N_T:1/(2*delta_T)]);
clear f E_prop1 =
ifft2((E_grating1FT).*exp((i*k0*z)-((i/2/k0)*(z)*(fact
    ^2*(xi).^2))));
clear xi clear E_grating1FT

toc
% Action of lens 1 ------------------------------
[X,T] = meshgrid(-N_X:delta_X:N_X, -N_T:delta_T:N_T);
    clear T
E_lens1 =((E_prop1)).*exp(i*k0*n*d - ((i*k0)/2/fl).*(X
    .^2)); % field just after lens 1
clear E_prop1; clear X

%Propagation to the mask from lens 1 ---------------
[xi,f]=
meshgrid([-1/(2*delta_X):1/2/N_X:1/(2*delta_X)],[-1/(2*
    delta_T):1/2/N_T:1/(2*delta_T)]);
clear f
E_prop2 = ifft2((fft2(E_lens1)).*exp((i*k0*z)-((i/2/k0)
    *(z)*(fact^2*(xi).^2))));%field after propagating to
    the mask
clear xi; clear E_lens1;

% Action of the mask ------------------
[X,T] = meshgrid(-N_X:delta_X:N_X, -N_T:delta_T:N_T);
    clear T f =
1.5;
cyclespermm = (1.3*f)/(8.5*4.2); %number of cycles per
    mm
E_mask = (E_prop2).*exp(i*(pi/2)*sin(2*pi*cyclespermm*X)
    );%field amplitude after mask
clear E_prop2 clear X

% Propagation after the mask to lens 2
    ------------------------
[xi,f]=meshgrid([-1/(2*delta_X):1/2/N_X:1/(2*delta_X)
    ],[-1/(2*delta_T):1/2/N_T:1/(2*delta_T)]);
clear f E_prop3 =
```

```
ifft2((fft2((E_mask))).*exp((i*k0*z)-((i/2/k0)*(z)*(fact
    ^2*(xi).^2))));
clear E_mask; clear xi

% Action of second lens ------------------------------
[X,T] = meshgrid(-N_X:delta_X:N_X, -N_T:delta_T:N_T);
    clear T
E_lens2 = ((E_prop3)).*exp(i*k0*n*d - ((i*k0)/2/fl)*(X
    .^2)); % field just after lens 1
clear E_prop3 clear X

% Propagation to second grating from second lens -------
meshgrid([-1/(2*delta_X):1/2/N_X:1/(2*delta_X)],[-1/(2*
    delta_T):1/2/N_T:1/(2*delta_T)]);
clear f E_prop4 =
ifft2((fft2((E_lens2))).*exp((i*k0*z)-((i/2/k0)*(z)*(
    fact^2*(xi).^2))));
clear E_lens2; clear xi;

% Second Grating
[n,m] = size(E_prop4); [X,T] = meshgrid(-N_X:delta_X:N_X
    ,
-N_T:delta_T:N_T); clear T;
for ii=1:m % loop over X
       t_shift = floor(beta_prime*X(1,ii)/delta_T); %How
          much to shift by
       E_grating2(:,ii) = circshift(E_prop4(:,ii),[
          t_shift,0]);
end clear t_shift clear E_prop4 clear X

% Mode from Pulse Shaper through a lens ----------------
fl_pinhole = 1000;
[X,T] = meshgrid(-N_X:delta_X:N_X, -N_T:delta_T:N_T);
clear T
E_lens =(E_grating2).*exp(i*k0*n*d - ((i*k0)/2/
    fl_pinhole).*(X.^2)); % field just after lens 1

clear E_grating2;
clear X
```

```
%Propagation to pinhole from lens ----------------------
[xi,f]= meshgrid([-1/(2*delta_X):1/2/N_X:1/(2*delta_X)
    ],[-1/(2*delta_T):1/2/N_T:1/(2*delta_T)]);
clear f
E_atpinhole = ifft2((fft2(E_lens)).*exp((i*k0*z)-((i/2/
    k0)*(z)*(fact^2*(xi).^2))));%field after propagating
    to the mask
clear xi;
clear E_lens;

%Field after pinhole ------------------------------
[n,m] = size(E_atpinhole);
E_pinhole = [zeros(n,round(m/2)-6) ones(n,11) zeros(n,
    round(m/2)-6)].*E_atpinhole;
clear E_atpinhole

toc

figure
plot(xx,sum((abs(E_grating2).^2),1)/max(sum((abs(
    E_grating2).^2),1)));
hold on
plot(x,((abs(E_input)).^2),'r');
hold on
plot(x,(abs(E_input)).^2/max((abs(E_input)).^2),'r');
hold on
plot(x,pulse_before_mask/max(pulse_before_mask),'k')
xlabel('x(mm)')
ylabel('Time Integrated Pulse')
```

B.2 Simulation of 7p Population for a Single Chirped Pulse

```
%Population calculation for a pulse with a given
    spectral phase
%uses sodium_eq, arrayfilter2
%Scans quadratic spectral phase

debug=0;
```

```
SavePop=0; % if SavePop=1 saves population in time,
    intesity profile and phase
% in separate directories for each value of DeltaI and
    flip position

global omega0Rad Io DeltaI; global trk g2 phi; C=3e8;

omega0Values=778:2:780;
DeltaT= 0.05; %FWHM of transform limited pulse in
    picoseconds (field)
tau_p=DeltaT/(2*sqrt(log(2))); % transform limited 1/e
    of the Field
pulse_area=2*pi; alpha=tau_p^2/4;
omega0Values = 778:1:778; % this is actually wavelenght

tic for nn=1:length(omega0Values)

omega0nm=omega0Values(nn)
omega0Rad = 2*pi*3e8/(omega0nm*1e-9); %central frequency
     in rad*THz

%=========================================================

% Create directory for each lambda
mkdir(num2str(omega0nm)); cd(num2str(omega0nm));

%=========================================================

% Set parameter for the grid
num_steps1=100; %100 steps normally
exp_max=-0.002;%0.01 from calibration data in (ps/rad)
    ^2, but can be changed as you please
exp_min=0.002;% -0.01 from calibration data in (ps/rad)
    ^2

DeltaIValues=1:1:3.01; % Values for the peak intensity
max_chirp_rate=1*exp_max/alpha; min_chirp_rate=1*exp_min
    /alpha;
Freq_chirp_rate=(min_chirp_rate:((max_chirp_rate-
    min_chirp_rate)/num_steps1):max_chirp_rate); % Values
```

```
    for the center of the phase in the pulse
%freqPhase=1:10; % For phases that take a frequency,
   oscillations during the pulse

shapped=meshgrid(Freq_chirp_rate, DeltaIValues);
shapped7p=meshgrid(Freq_chirp_rate, DeltaIValues);

t_values=-10*DeltaT:DeltaT/100:10*DeltaT; %extends to 10
    times pulse duration; sampled 1/100th of pulse
   duration

Field_envelope=exp(-t_values.^2/tau_p^2);
Int_TL=sum(Field_envelope)*DeltaT/100; phi_t=t_values*0;

chi2Io=1.0234E-02; Io=sqrt(pi*log(2))/(chi2Io*DeltaT*1e
   -12);
Iotl=Io;

%=========================================================

% Loop for shapped pulse
% Begins cycle for different phase parameters

for kk=1:length(DeltaIValues)
      DeltaI=DeltaIValues(kk)
   for mm=1:length(Freq_chirp_rate)
      %Phase_w=phaseDepth*pi*cos((omegasRad-omega0Rad)/(
         FWHMomega*FWHMtoe/2)-FWHMomega*FWHMtoe*2*pi);
beta=alpha*Freq_chirp_rate(mm); % setting these equal
   gives the maximum temporal chirp rate
b=beta/(4*(alpha^2+beta^2));

chirp_rate=b;
tau=sqrt(4*(alpha^2+beta^2)/abs(alpha)); %pulse duration
    is adjusted by the chirp rate

t_values=-10*tau:tau/100:10*tau;
Field_envelope=exp(-t_values.^2/tau^2);
phi_t=chirp_rate*t_values.^2;
```

```
if debug==1
    figure(101)
    plotyy(t_values, Field_envelope,t_values, phi_t);
    axis([-1 1 0 1]);
    if chirp_rate==0
        DeltaI
        sum(Int_TL)/sum(Field_envelope)/(tau/100);
    end
end Io=Iotl*sum(Int_TL)/sum(Field_envelope)/(tau/100);
   Ios=Io;

% RK fourth order begins here
tinit=min(t_values); tfinal=max(t_values);
dtrk = (tfinal - tinit)/500/2; %/2
trk = tinit:dtrk:tfinal; stemp = zeros(3,1); srk =
zeros(3,round(length(trk)/2)); stemp(1)=1;

g2 = interp1(t_values, Field_envelope, trk,'spline');
   phi =
interp1(t_values, phi_t, trk,'spline'); srk(:,1)=stemp;

for n = 2:length(trk)-2
   k1 = dtrk*sodium_eq7pDSStest(n, stemp);
   k2 = dtrk*sodium_eq7pDSStest(n + 1, stemp + k1/2);
   k3 = dtrk*sodium_eq7pDSStest(n + 1, stemp + k2/2);
   k4 = dtrk*sodium_eq7pDSStest(n+2, stemp + k3);
   srk(:,round((n+2)/2)) = stemp + k1/6 + k2/3 + k3/3 +
      k4/6;
   stemp = srk(:,round((n+2)/2));
end

if debug==1
%     if chirp_rate==0
        figure(102)
        plot(abs(srk').^2)
        title(['Chirp =' num2str(chirp_rate) '  pop4s ='
            num2str(abs(srk(2,length(srk))).^2)])
%    end
end srk=srk';
%trk2=tinit:dtrk*2:tfinal;
```

```
shapped(kk,mm)=abs(srk(length(srk),2)).^2;
shapped7p(kk,mm)=abs(srk(length(srk),3)).^2; toc

%=========================================================================

% Saves a lot of data
if SavePop==1
    trkhalf = tinit:2*dtrk:tfinal;
    %chirp_rate=omega0Rad+Freq_chirp_rate/omegaSteps*
       FWHMomega;
    %jumpPosnm=2*pi*3e8./chirp_rate;
    popDir=['dI' num2str(DeltaI) '_beta' Freq_chirp_rate
       *alpha];
    mkdir(popDir);
    cd(popDir);
    dlmwrite('pop.dat',abs(srk).^2,'\t');
    dlmwrite('Iprof.dat', [trk; g2],'\t');
    dlmwrite('phase.dat', [trk; phi],'\t')
    dlmwrite('t.dat', trkhalf,'\t')
    fid=fopen('parameters.dat','wt');
    fprintf(fid,'Pulse duration(FWHM ps) %g \n  TL Io %g
       \n  Shapped Io %g',DeltaT, Iotl, Ios);
    fclose(fid);

    cd ..
end
%clear g2 phi srk stemp t_values Field_envelope phi_t
end end

dlmwrite('betavalues.dat',Freq_chirp_rate, '\t');
dlmwrite('Ivalues.dat',DeltaIValues, '\t'); dlmwrite('4s
   .dat',
shapped, '\t'); dlmwrite('7p.dat', shapped7p, '\t');
% dlmwrite('unshapped.dat', [unshapped; unshapped7p], '\
   t');

figure surf(Freq_chirp_rate*alpha,DeltaIValues,shapped)
   view(0,90)
shading interp
%caxis([0 1]);
```

```
title('4s final population with linear sweep in
    frequency');
ylabel('I (units of Io)'); xlabel('Quadratic Phase (Rad)
    '); colorbar
print -dpng 4s.png

figure surf(Freq_chirp_rate*alpha,DeltaIValues,shapped7p
    ) view(0,90)
shading interp
%caxis([0 1]);
title('7p final population with linear sweep in
    frequency');
ylabel('I (units of Io)'); xlabel('Quadratic (Rad)');
    colorbar print
-dpng 7p.png

cd ..
end

function sp = sodium_eq7pDSStest(n,s)
%All units are in THz and ps
%time is now the index, g2 is intensity profile, phi is
    phase, both are arrays

global omega0Rad Io DeltaI; global trk g2 phi;
%tau=1/(2*sqrt(log(2)));

deltcoeff=0;
delta_7p=(omega0Rad-2.41278E+15)/1e12-trk(n)*deltcoeff
    /2;
chi2Io=1.0234E-02; chi0=chi2Io*Io/1e12;

% 18.3 and 32.3 are the values for the stark shift at 50
    fs, Io=2.883e15, it depends lineraly on intensity
% therefore this expression is correct
wgs=-32.3*Io/2.883e15; wes=18.3*Io/2.883e15; diffstark=
    wes-wgs;
w7psIo=0.000973832;
```

```
delta=(2*omega0Rad - 4.8519e+015)/1e12-trk(n)*deltcoeff;
    chi7p =
1.32707E-30/(2*1.05e-34)*sqrt(2*Io/(3e8*8.85e-12))/1e12;
stark7p=w7psIo*Io/1e12;

valg2= g2(n); valphi=-phi(n); t=trk(n);
sp = -i*[wgs*valg2*s(1)*DeltaI + exp(-i*valphi +
i*delta*t)*chi0*valg2*s(2)*DeltaI,
   exp(i*valphi - i*delta*t)*chi0*valg2*s(1)*DeltaI +
      wes*valg2*s(2)*DeltaI + chi7p*sqrt(valg2)*exp(-i*
      valphi*0.5+ i*delta_7p*t)*s(3)*sqrt(DeltaI),
   chi7p*sqrt(valg2)*exp(i*valphi*0.5- i*delta_7p*t)*s
      (2)*sqrt(DeltaI)+valg2*stark7p*DeltaI*s(3)];
```

B.3 Two Pulse Propagation through a Three-level Atomic Medium

```
%Propagation code for Rb EIT experiment. Written by S.
   Clow 09/08
%Propagates the laser field

%uses density_matrix_eqRb.m, Rbdensity.m

%Set the global valiables here
global  Delta_p Delta_c chi_p chi_c; global trk Ept Ect
   E_p E_c;

lambda_12   = 780; % 5s_1/2 - 5p_3/2 (nm)
lambda_23   = 776; % 5p_3/2 - 5d_3/2 (nm)
lambda_p    = 780.2; % probe field wavelength (nm)
lambda_c    = 776.0; % coupling field wavelength (nm)
eps0        = 8.854e-12; % C^2/N*m^2
hbar        = 1.0546e-034; %h/2pi
h_planck    = 6.63e-34; %J*s
C           = 3e8; %m/s
omega_12    = C/(lambda_12*1e-9) % Hz
omega_23    = C/(lambda_23*1e-9) % Hz
omega_p     = C/(lambda_p*1e-9); % Hz
omega_c     = C/(lambda_c*1e-9); % Hz
```

```
Delta_p      = 2*pi*(omega_p - omega_12)/1e12; % TRad/s
Delta_c      = 2*pi*(omega_c - omega_23)/1e12; % TRad/s
mu_23        = 1.500e-29; % Noordam 5p_3/2 - 5d_3/2 (C*m)
mu_12        = 4.976e-29; % coulomb meter 5s_1/2 - 5p_3/2
    (C*m) From Noordam

FWHM_c       = 3.5; % coupling pulse duration (ps)
FWHM_p       = 1.25; % probe pulse duration (ps)
tau_p        = sqrt(2) * (FWHM_p/(2*sqrt(log(2)))); % (ps
   )
tau_c        = sqrt(2) * (FWHM_c/(2*sqrt(log(2)))); % (ps
   )
E_pi_p       = hbar*sqrt(pi)/(mu_12*tau_p*1e-12); % Field
    stength for a pi pulse on 5s_1/2 - 5p_3/2 transition
    GIVEN mu_12 (V/m)
E_pi_c       = hbar*sqrt(pi)/(mu_23*tau_c*1e-12); % Field
    stength for a pi pulse on 5p_3/2 - 5d_3/2 transition
    GIVEN mu_23 (V/m)

delays       = 3.9:0.1:3.9

for dd = 1:length(delays) global trk Ept Ect E_p E_c;

probe_delay = delays(dd); % probe delay (ps)
```

```
%Create directory for each delay
 mkdir([num2str(delays(dd)),' ps probe delay']);
 cd([num2str(delays(dd)),' ps probe delay']);
```

```
Ec_strength = [4.7]; % relative to a pi pulse on the 5
   p_3/2 - 5d_3/2 transition
Ec_strength = 3.8:0.1:3.8;

for ii = 1:length(Ec_strength) global trk Ept Ect E_p
   E_c;
```

```
E_c         = E_pi_c; %130 set by the pulse shaper in
   the experiment
E_p         = E_pi_p;
E_c         = Ec_strength(ii)*1e7; %V/m Measured
E_p         = E_c/(130); %Set by the pulse shaper

chi_p       = E_p*mu_12/h_planck/1e12; %peak probe pulse
    Rabi frequency (THz)
chi_c       = E_c*mu_23/h_planck/1e12; %peak coupling
   pulse Rabi frequency (THz)

Ztotal      = 0.01; % Total field propagation length (m)
dz          = 60e-6; % Propagation step (m)
zvalues     = 0:dz:dz; %Z values in m
zvalues     = 0:dz:Ztotal; %Z values in m

T           = 130:50:130; %C

[rho,P]     = Rbdensity(T); % Returns density of vapor
   pressure in liquid phase in atoms/m^3
N = rho;

Init5s      = 1.00; Init5p      = 0.00; Init5d      =
   0.00;

 Set values for RK

tinit       = -40; % initial time (ps)
tfinal      = 40;  % final time (ps)
intdt       = 0.040; % Time integration step (ps)
intdt       = 0.040; % Time integration step (ps)
dtrk        = intdt;

trk         = tinit:dtrk:tfinal; %time axis for RK
   integration
trk_reduced = trk(2:length(trk)-1);
trkhalf     = tinit:dtrk*2:tfinal;
freq        = [-1/2/dtrk:1/2/tfinal:1/2/dtrk];
```

```
%Since we use Runge Kutta 4th order we need to
   interpolate to
%eliminate to get the right number of samples
%(RK 4th order samples twice more points)

for TT = 1:length(T)

T(TT) tic

Ec_envelope = exp(-(trk).^2/(tau_c)^2); % Initial
   couling field envelope (ps)
Ep_envelope = exp(-(trk + probe_delay).^2/(tau_p)^2); %
   Inital probe field envelope (ps)

Epztemp=zeros(length(zvalues)-1,round(length(trk))); %
   define an array for the fields in t and z
Ecztemp=zeros(length(zvalues)-1,round(length(trk)));

Epzt = vertcat(E_p*Ep_envelope, Epztemp); %merge with
   the initial fields
Eczt = vertcat(0*E_c*Ec_envelope, Ecztemp);
```

```
%Create directory for coupling strength
 mkdir([num2str(Ec_strength(ii)),' Coupling']);
 cd([num2str(Ec_strength(ii)),' Coupling']);
```

```
 Set initial conditions for the amplitudes

qtemp      = zeros(3,3);% make a temporary
qtemp(1,1) = Init5s; % initial 5s population
qtemp(2,2) = Init5p; % initial 5p population
qtemp(3,3) = Init5d; % initial 5d population

q(:,:,1) = qtemp;    % Zeros everywhere else

 Start 4th order Runge Kutta integration
```

```
tic
eta_c = i*mu_23*omega_c*N(TT)/(2*C*eps0); %prefactor to
   density matrix element in prop eqns.
eta_p = i*mu_12*omega_p*N(TT)/(2*C*eps0);

for zz=2:length(zvalues)

        % Propagate field to z+dz
        % Propagation equations

            Epzt(zz,:) = Epzt(zz-1,:) + dz*eta_p*
               transpose(squeeze(q(2,1,:))).*exp(i*
               Delta_p*trk);
            Eczt(zz,:) = Eczt(zz-1,:) + dz*eta_c*
               transpose(squeeze(q(3,2,:))).*exp(i*
               Delta_c*trk);

           %Calculate the Spectrum of the Probe
            Epzomega(zz,:) = fftshift(fft(fftshift(Epzt(
               zz,:))));

            Ept = Epzt(zz,:); %used in the RK integration
            Ect = Eczt(zz,:);

        for n = 2:length(trk)-2
            k1 = dtrk*density_matrix_eqRb(n, qtemp);
            k2 = dtrk*density_matrix_eqRb(n + 1, qtemp +
                k1/2);
            k3 = dtrk*density_matrix_eqRb(n + 1, qtemp +
                k2/2);
            k4 = dtrk*density_matrix_eqRb(n+2, qtemp +
               k3);
            q(:,:,n) = qtemp + k1/6 + k2/3 + k3/3 + k4
               /6;
            qtemp = q(:,:,n);
        end
        q(:,:,n+1)     = q(:,:,n);
        q(:,:,n+2)     = q(:,:,n+1);

        fullq11(zz,:) = transpose(squeeze(q(1,1,:)));
```

```
        fullq12(zz,:) = transpose(squeeze(q(1,2,:)));
        fullq13(zz,:) = transpose(squeeze(q(1,3,:)));
        fullq21(zz,:) = transpose(squeeze(q(2,1,:)));
        fullq22(zz,:) = transpose(squeeze(q(2,2,:)));
        fullq23(zz,:) = transpose(squeeze(q(2,3,:)));
        fullq31(zz,:) = transpose(squeeze(q(3,1,:)));
        fullq32(zz,:) = transpose(squeeze(q(3,2,:)));
        fullq33(zz,:) = transpose(squeeze(q(3,3,:)));

        %Reset the density matrix elements for "new"
           atoms encountered

        qtemp      = zeros(3,3);% make a temporary
        qtemp(1,1) = Init5s; % initial 5s population
        qtemp(2,2) = Init5p; % initial 5p population
        qtemp(3,3) = Init5d; % initial 5d population

        %Calculate the energy in the pulse as a function
            of position in the
        %cell
        Energy(zz) = sum(eps0*C*abs(Epzt(zz,:)).^2*intdt
           *1e-12);
        diffI(zz)  = sum(eps0*C*abs(Epzt(zz,:)).^2*intdt
           *1e-12) - sum(0.5*eps0*C*abs(Epzt(zz-1,:))
           .^2*intdt*1e-12);
        Eatoms(zz) = hbar*omega_12*N*dz*fullq22(zz,
           length(trk));
        %
        %Let us know where we're at
        zz/length(zvalues)
end toc

 dlmwrite('frequency.dat',freq, '\t');
 dlmwrite('time.dat',trk, '\t');
 dlmwrite('z.dat',zvalues, '\t');
 dlmwrite('Epzt.dat', Epzt, '\t');
 dlmwrite('Eczt.dat', Eczt, '\t');
 dlmwrite('Epzomega.dat', Epzomega, '\t');

convfunc = exp(-(freq/0.1).^2); convolved1 =
```

```
conv(convfunc,abs(Epzomega(size(Epzomega,1),:)).^2);
    convolved1 =
convolved1/max(convolved1); convolved2 =
conv(convfunc,abs(Epzomega(2,:)).^2); convolved2 =
convolved2/max(convolved2); kron_delt  =
[zeros(1,round(length(freq)/2)-1) 1
zeros(1,round(length(freq)/2)-1)]; conv_freq = conv(freq
    ,kron_delt);
conv_amp1 = max(abs(Epzomega(size(Epzomega,1),:)).^2);
    conv_amp2 =
max(abs(Epzomega(2,:)).^2);

lambda  = load('U:\papers\group papers\EIT\Data\lambda')
    ; triplet =
load('U:\papers\group papers\EIT\Data\triplet structure
    probe');
probe_long = load('U:\papers\group papers\EIT\Data\probe
     at long
delay'); nu       = 3.0e8./(lambda*1e-9); nu       = (nu -
3.8447e14)/1e12; lambda2 = 3.0e8./(conv_freq*1e12
    +3.8447e14)/1e-9;

figure hold on setaxes
plot(lambda2,max(triplet)*convolved1/max(convolved1),'
    LineWidth',3,'Color','b');
plot(lambda,triplet,'LineWidth',3,'Color','r');
plot(lambda,probe_long,'LineWidth',3,'Color','r') title
    (['Calculated
and Measured Probe Spectrum, ' ,num2str(ii)]); ylabel('
    Probe
Spectrum'); xlabel('Frequency (THz)'); box on setaxes
    axis([778.75
781.85 0 1.8]) print('-dpng', [['Output Probe Spectrum'
,num2str(ii)] '.png']) close

figure Ep_plot =
real(Epzt(size(Epzomega,1),:)/max(Epzt(size(Epzomega,1)
    ,:)));
Ec_plot =
```

```
real(Eczt(size(Epzomega,1),:)/max(Eczt(size(Epzomega,1)
    ,:))); AFP
= cumsum(dtrk*mu_23*Eczt(size(Epzomega,1),:)/h_planck/1
    e12); hold on
setaxes
[AX,H1,H2] = plotyy(trk,Ep_plot,trk,AFP); %,'LineWidth
    ',3,'Color','r');
set(AX(1),'XLim',[-10,10]), set(H1,'LineWidth',3),
set(H1,'Color','r') set(AX(2),'XLim',[-10,10]),
set(H2,'LineWidth',3), set(H2,'Color','k')
set(get(AX(2),'Ylabel'),'String','Atom-field Phase [\pi
    ]')
plot(trk,Ec_plot,'LineWidth',3,'Color','b'); title(['
    Coupling and
Probe Pulses, ',num2str(ii)]); ylabel('Real(E_p,E_c)');
xlabel('Time (ps)'); box on max_Ep =
max(real(Epzt(size(Epzomega,1),:)/max(Epzt(size(Epzomega
    ,1),:))))
min_Ep =
min(real(Epzt(size(Epzomega,1),:)/max(Epzt(size(Epzomega
    ,1),:))))
axis([-10 10 min_Ep max_Ep]) setaxes format_yy_figure
    print('-dpng',
[['Coupling and Probe Pulses with Atom-field Phase',
    num2str(ii)]
'.png']) close

figure setaxes surf(trk,zvalues,(abs(Epzt)).^2), shading
    interp,
view(0,90) title(['Epzt, ',num2str(ii)]); ylabel('Z (m)
    ');
xlabel('Time (ps)'); colorbar setaxes box on grid off
    axis([-10 10
min(zvalues) max(zvalues)]) fname1 = ['Epzt ', num2str(
    E_p)]
print('-dpng', [fname1 '.png']) close

figure setaxes surf(trk,zvalues,(abs(Eczt)).^2), shading
    interp,
```

```
view(0,90) title(['Eczt, ' ,num2str(ii)]); ylabel('Z (m)
    ');
xlabel('Time (ps)'); colorbar setaxes box on grid off
    axis([-10 10
min(zvalues) max(zvalues)]) fname2 = ['Eczt ', num2str(
    ii)]
print('-dpng', [fname2 '.png']) close

figure setaxes
plot(zvalues(2:length(zvalues)),Energy(2:length(Energy))
    ,'LineWidth',3,'Color','k');
title(['Pulse Energy v. Z Position, ' ,num2str(ii)]);
ylabel('Energy'); xlabel('Z Position (m)'); box on
    setaxes
print('-dpng', [['Pulse Energy v. Z Position ' ,num2str(
    ii)]
'.png']) close

figure setaxes hold on
plot(trk,abs(Epzt(size(Epzt,1),:))/max(abs(Epzt(size(
    Epzt,1),:))),'LineWidth',3,'Color','b')
plot(trk,abs(Eczt(size(Eczt,1),:))/max(abs(Eczt(size(
    Eczt,1),:))),'LineWidth',3,'Color','r')
title(['Pump and Probe at Output, ' ,num2str(ii)]);
    xlabel('time
(ps)'); box on setaxes print('-dpng', [['Pump and Probe
    at Output '
,num2str(ii)] '.png']) close

figure setaxes surf(freq,zvalues,abs(Epzomega).^2),
    shading interp,
view(0,90) title(['Epzomega, ',num2str(ii)]); ylabel('Z
    (m)');
xlabel('Frequency (THz)'); colorbar setaxes box on grid
    off axis([-1
1 min(zvalues) max(zvalues)]) fname3 = ['Epzomega ',
    num2str(ii)]
print('-dpng', [fname3 '.png']) close

 clear Epzt Eczt Ept Ect Epzomega
```

```
 clear qtemp fullq11 fullq12 fullq13 fullq21 fullq22
    fullq23 fullq31 fullq32 fullq33
 clear q eta_c eta_p k1 k2 k3 k4
 clear E_c E_p chi_c chi_p

end
cd ..
end
cd ..
end
cd ..

function qp = density_matrix_eqRb(n,q)
% Equations for forward light propagation. Solves for
   each z position in
% time.
%All units are in THz and ps
%time is now the index, g2 is intensity profile, phi is
   phase, both are arrays
% q(1) = Q11, q(2)=Q22, q(3)=Q21, , conj(q(3))=Q12, q(4)
   =Q33,q(5)=Q31, Q(6)=Q32

global trk Ept Ect chi_p chi_c Delta_p Delta_c;

h_planck = 6.63e-34; %J*s
hbar = 1.05457168e-34; % in J*s/rad

mu_23 = 1.500e-29; % Noordam 5p_3/2 - 5d_3/2 (C*m)
mu_12 = 4.976e-29; % coulomb meter 5s_1/2 - 5p_3/2 (C*m)
    From Noordam

valE_p = Ept(n); % probe field value at time n
valE_c = Ect(n); % coupling field value at time n

Omega_p = mu_12*valE_p/hbar/1e12; % TRad/s (integration
   steps are in ps)
Omega_c = mu_23*valE_c/hbar/1e12;

gamma11 = 0;
```

```
gamma22 = 2*pi*(1/25.7e-9/1e12); %radiative lifetime of
    25.7ns
gamma12 = 2*pi*0.01 + 2*pi*0.01 + gamma11/2 + gamma22/2;
     % Collisions
gamma23 = gamma12; gamma13 = 0; gamma31 = 0;
gamma33 = 2*pi*(1/240e-9/1e12); %radiative lifetime of
    240ns

% Equations of motion
D = -1*[gamma11*q(1,1) gamma12*q(1,2) gamma13; gamma12*q
    (2,1)
gamma22*q(2,2) gamma23*q(2,3); gamma31 gamma23*q(2,3)
gamma33*q(3,3)]; Ham = -1/2*[-2*Delta_p Omega_p 0; conj(
    Omega_p) 0
Omega_c; 0 conj(Omega_c) 2*Delta_c]; qp = -i*(Ham*q - q*
    Ham) + D;
```

Bibliography

[1] D. Spence, P. Kean, and W. Sibbett. 60-fsec pulse generation from a self-mode-locked ti:sapphire laser. *Optics Letters*, 16:42, 1991.

[2] Melanie Asaki, Chung po Hauang, Dennis Garvey, Jianping Zhou, Henry Kapteyn, and Margaret Murnane. Generation of 11-fs pulses from a self-mode-locked ti:sapphire laser. *Optics Letters*, 18:977, 1993.

[3] Sterling Backus, Charles G. Durfee III, Margaret M. Murnane, and Henry C. Kapteyn. High power ultrafast lasers. *Review of Scientific Instruments*, 69(3):1207–1223, 1998.

[4] J. S. Melinger, D. McMorrow, C. Hillegas, and W. S. Warren. Selective excitation of vibrational overtones in an anharmonic ladder with frequency- and amplitude-modulated laser pulses. *Phys. Rev. A*, 51(4): 3366–3369, 1995.

[5] Yong-Xin Yan, Edward B. Gamble Jr., and Keith A. Nelson. Impulsive stimulated scattering: General inportance in femtosecond laser pulse interactions with matter, and spectroscopic applications. *J. Chem. Phys.*, 83(11):5391–5399, 1985.

[6] Herschel Rabitz, Regina de Vivie-Riedle, Marcus Motzkus, and Karl Kompa. Whither the future of controlling quantum phenomena? *Science*, 288:824–828, 2000.

[7] D. Goswami. *Physics Reports*, 374:385, 2003.

[8] D. Abrashkevich, M. Shapiro, and P. Brumer. *J. Chem. Phys.*, 116:5584, 2002.

[9] D.J. Tannor and S.A. Rice. *J. Chem. Phys.*, 83:5013, 1985.

[10] Ferenc Krausz and Misha Ivanov. Attosecond physics. *Rev. Mod. Phys.*, 81:163–234, 2009.

[11] Doron Meshulach and Yaron Silberberg. Coherent quantum control of two-photon transitions by a femtosecond laser pulse. *Nature*, 396:239–242, 1998.

[12] Nirit Dudovich, Barak Dayan, Sarah M. Gallagher-Faeder, and Yaron Silberberg. Transform-limited pulses are not optimal for resonant multiphoton transitions. *Phys. Rev. Lett.*, 86(1):000047, 2001.

[13] A. Gandman, L. Chuntonov, Leonid Rybak, and Zohar Amitay. Coherent phase control of resonance-mediated (2+1) three-photon absorption. *Phys. Rev. A*, 75:031401, 2007.

[14] Matthew C. Stowe, Avi Pe'er, and Jun Ye. Control of four-level quantum coherence via discrete spectral shaping of an optical frequency comb. *Phys. Rev. Lett.*, 100:203001, 2008.

[15] B. Broers, H.B. van Linden van den Heuvell, and L.D. Noordam. Efficient population transfer in a three-level ladder system by frequency-swept ultrashort laser pulses. *Phys. Rev. Lett.*, 69(14):2062, 1992.

[16] S. Chelkowski, A.D. Bandrauk, and P.B. Corkum. Efficient molecular dissociation by a chirped ultrashort infrared laser pulse. *Phys. Rev. Lett.*, 65(19):2355, 1990.

[17] E.A. Shapiro, V. Milner, C. Menzel-Jones, and M. Shapiro. Piecewise adiabatic passage with a series of femtosecond pulses. *Phys. Rev. Lett.*, 99:033002, 2007.

[18] S. Zhdanovich, E.A. Shapiro, J.W. Hepburn, M. Shapiro, and V. Milner. Complete transfer of populations from a single state to a preselected superposition of states using piecewise adiabatic passage: Experiment. *Phys. Rev. A*, 80:063405, 2009.

[19] E.A. Shapiro, V. Milner, and M. Shapiro. Complete transfer of populations from a single state to a preselected superposition of states using piecewise adiabatic passage: Theory. *Phys. Rev. A*, 79:023422, 2009.

[20] B.T. Torosov, G.S. Vasilev, and N.V. Vitanov. Symmetries and asymmetries in coherent atomic excitation by chirped laser pulses. *Opt. Comm.*, 283:1338–1345, 2010.

[21] A.A Rangelov, N.N. Vitanov, and B.W. Shore. Rapid adiabatic passage without level crossing. *Opt. Comm.*, 283:1346–1350, 2010.

[22] K. Bergmann, H. Theuer, and B.W. Shore. Coherent population transfer among quantum states of atoms and molecules. *Rev. Mod. Phys.*, 70(3): 1003, 1998.

[23] N. Dudovich, T. Polack, A. Pe'er, and Y. Silberberg. *Phys. Rev. Lett.*, 94:083002, 2005.

[24] A.A. Rangelov, N.V. Vitanov, L.P. Yatsenko, B.W. Shore, T. Halfmann, and K. Bergmann. Stark-shift-chirped rapid-adiabatic-passage technique among three states. *Phys. Rev. A*, 72:053403, 2005.

[25] George N. Gibson. Adiabatic passage on high-order multiphoton transitions. *Phys. Rev. A.*, 72:041404(R), 2005.

[26] G. Gibson. Multiphoton pi pulses. *Phys. Rev. Lett.*, 89(26):263001, 2002.

[27] Carlos Alberto Trallero. *Strong Field Coherent Control*. PhD thesis, Stony Brook University, Stony Brook, NY, May 2007.

[28] M. G. Moore and A. Vardi. *Phys. Rev. Lett.*, 88:160402, 2002.

[29] B. Borca, J. Dunn, V. Kokoouiline, and C. Greene. Atom-molecule laser fed by stimulated three-body recombination. *Physical Review Letters*, 91:070404, 2003.

[30] C. Trallero-Herrero, Michael Spanner, and T. C. Weinacht. Understanding strong field coherent control: Measuring single atom versus collective dynamics. *Phys. Rev. A*, 74:051403, 2006.

[31] L. Xiao-Li, H. Liu, H. Wang, W. Zhao, and S. Shi. Control of the superfluorescence for compact optical parametric chirped pulse amplification. *Journal of Modern Optics*, 12:587, 2008.

[32] R. Bonifacio and L.A. Lugiato. Cooperative radiation processes in 2-level systems - superfluorescence. *Physical Review A*, 11:1507, 1975.

[33] R. Bonifacio and L.A. Lugiato. Cooperative radiation processes in 2-level systems - superfluorescence 2. *Physical Review A*, 12:587, 1975.

[34] J. H. Brownell, X. Lu, and S.R. Hartmann. Yoked superfluorescence. *Phys. Rev. Lett.*, 75:3265, 1995.

[35] A. I. Lvovsky, S. R. Hartmann, and F. Moshary. Superfluorescence-stimulated photon echoes. *Phys. Rev. Lett.*, 89:263602, 2002.

[36] Wei Min, Sijia Lu, Shasha Chong, Rahul Roy, Gary R. Holtom, and Sunney Xie. Imaging chromophores with undetectable fluorescence by stimulated emission microscopy. *Nature*, 46:1105–1109, 2009.

[37] Doron Meshulach and Yaron Silberberg. Coherent quantum control of multiphoton transitions by shaped ultrashort optical pulses. *Phys. Rev. A*, 60(2):1287–1292, 1999.

[38] C. Trallero-Herrero, J.L. Cohen, and T. C. Weinacht. Strong-field atomic phase matching. *Phys. Rev. Lett.*, 96:063603, 2006.

[39] Stephen D. Clow, Carlos Trallero-Herrero, Thomas Bergeman, and Thomas Weinacht. Strong-field coherent control of atomic population transfer. *Phys. Rev Lett.*, 100:233603, 2008.

[40] R. Trebino and D.J. Kane. Using phase retrieval to measure the intensity and phase of ultrashort pulses: frequency-resolved optical gating. *J. Opt. Soc. Am. A*, 10:1101, 1993.

[41] J. X. Tull, M. A. Dugan, and W. S. Warren. High resolution, ultrafast laser pulse shaping and its applications. *Adv. Magn. Opt. Res.*, 20:1–50, 1997.

[42] R.S. Judson and H. Rabitz. *Phys. Rev. Lett.*, 68:1500, 1992.

[43] David Michael Cardoza. *Understanding and Applying Learning Control to Molecular Fragmentation*. PhD thesis, Stony Brook University, Stony Brook, NY, June 2006.

[44] Daniel A. Steck. *Rubidium 87 D Line Data*. PhD thesis, Los Alamos, NM 87545, May 2001. http://steck.us/alkalidata.

[45] Daniel A. Steck. Sodium d line data. Theoretical Division (T-8), MS B285, Los Alamos National Laboratory, Los Alamos, NM 87545, May 2000. http://steck.us/alkalidata.

[46] M. F. H. Schuurmans and D. Polder. Superfluorescence and amplified spontaneous emission: A unified theory. *Phys. Lett. A*, 72:306, 1979.

[47] Benjamin Sussman, Rune Lausten, and Albert Stolow. Focusing of light following a 4-f pulse shaper: Considerations for quantum control. *Phys. Rev. A*, 77:043416, 2008.

[48] Takasumi Tanabe, Fumihiko Kannari, Frank Korte, Jurgen Koch, and Broris Chichkov. Influence of spatiotemporal coupling induced by an ultrashort laser pulse shaper on a focused beam profile. *Applied Optics*, 44:1092, 2005.

[49] F. Frei, A. Galler, and T. Feurer. Space-time coupling in femtosecond pulse shaping and its effect on coherent control. *J. Chem. Phys.*, 130: 034302, 2009.

[50] A. M. Weiner. Femtosecond optical pulse shaping and processing. *Prog. Quant. Electr.*, 19:161–237, 1995.

[51] J. Paye and A. Migus. Space-time wigner functions and their application to the analysis of a pulse shaper. *J. Opt. Soc. Am. B*, 12(8):1480, 1995.

[52] M.A. Dugan, J.X. Tull, and W.S. Warren. High-resolution acousto-optic shaping of unamplified and amplified femtosecond laser pulses. *J. Opt. Soc. Am. B*, 14(9):2348, 1997.

[53] M. Wefers and K.A. Nelson. Analysis of programmable ultrashort waveform generation using liquid-crystal spatial light modulators. *J. Opt. Soc. Am. B*, 12(7):1343, 1995.

[54] M. Wefers and K.A. Nelson. Space-time profiles of shaped ultrafast optical waveforms. *IEEE J. Quant. Elect.*, 32(1):161, 1996.

[55] M. Kempe, U. Stamm, B. Wilhelmi, and W. Rudolph. Spatial and temporal transformation of femtosecond laser pulses by lenses and lens systems. *J. Opt. Soc. Am. B*, 9(7):1158, 1992.

[56] S. Akturk, M. Kimmel, P. O'Shea, and R. Trebino. Extremely simple device for measuring 20-fs pulses. *Opt. Lett.*, 29:1025, 2004.

[57] Yu. Ralchenko, F. C. Jou, D. E. Kelleher, A. E. Kramida, A. Musgrove, J. Reader, W. L. Wiese, and K. Olsen. Nist atomic spectra database (version 3.1.0). In *NIST Atomic Spectra Database, NIST Standard Reference Database Number 78*. National Institute of Standards and Technology, Gaithersburg MD, 20899, 2006. http://physics.nist.gov/PhysRefData/ASD/.

[58] David Tannor. *Introduction to Quantum Mechanics: A Time-Dependent Perspective*. University Science Books, Herndon, VA, 2005.

[59] C. Trallero-Herrero, D. Cardoza, J. L. Cohen, and T. C. Weinacht. *Phys. Rev. A.*, 71:013423, 2005.

[60] C. Trallero-Herrero, D. Cardoza, T. C. Weinacht, and J. L. Cohen. Coherent control of strong field multiphoton absorption in the presence of dynamic stark shifts. *Phys. Rev. A*, 71:013423, 2005.

[61] C. Trallero-Herrero, J. L. Cohen, and T. C. Weinacht. *Phys. Rev. Lett.*, 96:063603, 2006.

[62] A. Präkelt, M. Wollenhaupt, C Sarpe-Tudoran, and T. Baumert. Phase control of a two-photon transition with shaped femtosecond laser-pulse sequence. *Phys. Rev. A*, 70:063407, 2004.

[63] R. R. Jones. *Phys. Rev. Lett.*, 74(7):1091, 1995.

[64] C. Trallero-Herrero and T. C. Weinacht. Transition from weak- to strong-field coherent control. *Phys. Rev. A*, 75:063401, 2007.

[65] Vladimir S Lebedev and Ilya I Fabrikant. Semiclassical calculation of the l-mixing and n,l-changin collisions of rydberg atoms with rare-gas atoms. *J. Phys. B*, 30:2649, 1997.

[66] T.F. Gallagher, S.A. Edelstein, and R.M. Hill. Collisional angular-momentum mixing of rydberg states of na by he, ne, and ar. *Phys. Rev. A*, 15(5):1945, 1977.

[67] W.E. Cooke and T.F. Gallagher. Calculation of autoionization rates for high-angular-momentum rydberg states. *Phys. Rev. A*, 19(6):2151, 1979.

[68] F. Masnou-Seeuws, J. Boulmer, T. Maurin, A.L. Roche, and P. Valiron. Theoretical predictions and experimental observation of $(n+1) \rightarrow nl(l \geq 2)$ in excited sodium-rare-gas collisions. *J. Phys. B*, 15:2989, 1982.

[69] Constantine Theodosiou. Lifetimes of alkali-metal-atom rydberg states. *Phys. Rev. A*, 30(6):2881, 1984.

[70] T. Scholz, M. Schiffer, J. Welzel, D. Cysarz, and W. Lange. Spatial effects of radiation trapping in an optically thick atomic vapor excited by a laser beam. *Phys. Rev. A*, 53(4):2169, 1996.

[71] J. Paye. The chronocyclic representation of ultrashort light pulses. *IEEE J. of Quant. Electron.*, 28(10):2262–2273, 1992.

[72] Antoine Monmayrant, Beatrice Chatel, and Bertrand Girard. Quantum state measurement using coherent transients. *Phys. Rev. Lett.*, 96: 103002, 2006.

[73] David J. Tannor. *Introduction to Quantum Mechanics: A Time-dependent Perspective*. University Science Books, Sausalito, California, 2007.

[74] Yaron Silberberg. Quantum coherent control for nonlinear spectroscopy and microscopy. *Annual Review of Physical Chemistry*, 2009.

[75] M. Krug, T. Bayer, M. Wollenhaupt, C. Sarpe-Tudoran, T. Baumert, S.S. Ivanov, and N.N. Vitanov. Coherent strong-field control of multiple states by a single chirped femtosecond laser pulse. *New Journal of Physics*, 11:105051, 2009.

[76] Giovanna Morigi, Sonja Franke-Arnold, and Gian-Luca Oppo. Phase-dependent interaction in a four-level atomic configuration. *Phys. Rev. A*, 66:053409, 2002.

[77] Sarah Kajari-Schroder, Giovanna Morigi, Sonja Franke-Arnold, and Gian-Luca Oppo. Phase-dependent light propagation in atomic vapors. *Phys. Rev. A*, 75:013816, 2007.

[78] Daniel Felinto and Carlos E. E. Lopez. Theory for direct frequency-comb spectroscopy. *Phys. Rev. A*, 80:013419, 2009.

[79] Uvo C. Holscher, Stephen D. Clow, and Thomas Weinacht. Ultrafast atomic phase modulation. *Phys. Rev A (R)*, 80:011812, 2009.

[80] K.-J. Boller, A. Imamoglu, and S. E. Harris. Observation of electromagnetically induced transparency. *Phys. Rev. Lett.*, 66(20):2593–2596, 1991.

[81] J. E. Field, K. H. Hahn, and S. E. Harris. Observation of electromagnetically induced transparency in collisionally broadened lead vapor. *Phys. Rev. Lett.*, 67(22):3062–, 1991.

[82] S. H. Autler and C. H. Townes. Stark effect in rapidly varying fields. *Phys. Rev.*, 100(2):703–, 1955.

[83] Lene Vestergaard Hau, S. E. Harris, Zachary Dutton, and Cyrus H. Behroozi. Light speed reduction to 17 metres per second in an ultracold atomic. *Nature*, 397(6720):594–598, 1999.

[84] S. E. Harris, J. E. Field, and A. Imamoglu. Nonlinear optical process using electromagnetically induced transparency. *Phys. Rev. Lett.*, 64 (10):1107 – 1110, 1990.

[85] K. Hakuta, L. Marmet, and B. P. Stoicheff. Electric-field-induced second-harmonic generation with reduced absorption in atomic hydrogen. *Phys. Rev. Lett.*, 66(5):596–, 1991.

[86] Zhi-Heng Loh, Chris H. Greene, and Stephen R. Leone. Femtosecond induced transparency and absorption in the extreme ultraviolet by coherent coupling of the he 2s2p (1po) and 2p2 (1se) double excitation states with 800nm light. *Chemical Physics*, 350(1-3):7–13, 2008.

[87] Christian Buth, Robin Santra, and Linda Young. Electromagnetically induced transparency for x rays. *Phys. Rev. Lett.*, 98(25):253001–4, 2007.

[88] C. Buth and R. Santra. *Phys. Rev. A*, 78:043409, 2008.

[89] Rick Trebino, Kenneth W. DeLong, David N. Fittinghoff, John N. Sweetser, Marco A. Krumbugel, Bruce A. Richman, and Daniel J. Kane. Measuring ultrashort laser pulses in the time–frequency domain using frequency–resolved optical gating. *Rev. Sci. Instrum.*, 68(9):3277–3295, 1997.

[90] C. Trallero-Herrero, Michael Spanner, and T. C. Weinacht. Understanding strong field coherent control: Measuring single atom versus collective dynamics. *Phys. Rev. A*, 74:051403, 2006.

[91] B. Broers, H.B. van Linden van den Heuvell, and L.D. Noordam. Efficient population transfer in a three-level ladder system by frequency-swept ultrashort laser pulses. *Phys. Rev. Lett.*, 69(14):2062, 1992.

[92] C. Trallero-Herrero, J.L. Cohen, and T. C. Weinacht. Strong-field atomic phase matching. *Phys. Rev. Lett.*, 96:063603, 2006.

[93] M. Kiffner and T. N. Dey. *Phys. Rev. A*, 79:023829, 2009.

[94] Chien Liu, Zachary Dutton, Cyrus H. Behroozi, and Lene Vestergaard Hau. Observation of coherent optical information storage in an atomic medium using halted light pulses. *Nature*, 409:490, 2001.

[95] Roberto Buffa, Stefano Cavalieri, and Marco V. Tognetti. Coherent control of temporal pulse shaping by electromagnetically induced transparency. *Phys. Rev. A*, 69:033815, 2004.

[96] T. Brixner, N. H. Damrauer, P. Niklaus, and G. Gerber. Photoselective adaptive femtosecond quantum control in the liquid phase. *Nature*, 414 (6859):57–60, 2001.

[97] T. C. Weinacht, R. A. Bartels, S. Backus, B. Pearson, P. H. Bucksbaum, JM. Geremia, H. Rabitz, H. C. Kapteyn, and M. M. Murnane. *Chem. Phys. Lett.*, 344:333, 2001.

[98] Nirit Dudovich, Dan Oron, and Yaron Silberberg. Single-pulse coherently controlled nonlinear raman spectroscopy and microscopy. *Nature*, 418:512–514, 2002.

[99] Bernhard von Vacano and Marcus Motzkus. Molecular discrimination of a mixture with single-beam raman control. *J. Chem. Phys.*, 127:144514, 2007.

[100] Michael Spanner and Paul Brumer. *Phys. Rev. A*, 73:023809, 2006.

[101] Michael Spanner and Paul Brumer. *Phys. Rev. A*, 73:023810, 2006.

[102] Kunihito Hoki and Paul Brumer. Mechanisms in adaptive feedback control: Photoisomerization in a liquid. *Phys. Rev. Lett.*, 95:168305, 2005.

[103] R. Weigand, M. Wittmann, and J.M. Guerra. Generation of femtosecond pulses by two-photon pumping supercontinuum-seeded collinear traveling wave amplification in a dye solution. *Appl. Phys. B*, 73:201–203, 2001.

[104] D. Meshulach and Y. Silberberg. *Nature*, 396:239, 1998.

[105] Carlos Trallero-Herrero, Stephen D. Clow, Thomas Bergeman, and Thomas Weinacht. Strong-field coherent control of atomic population transfer. *J. Phys. B: At. Mol. Opt. Phys.*, 41:074014, 2008.

[106] J. D. Jackson. *Classical Electrodynamics*. John Wiley & Sons, Inc., New York, 1998.

[107] R. F. O'Connell and E. P. Wigner. Some properties of a non-negative quantum-mechanical distribution function. *Phys. Lett.*, 85A(3):121–126, 1981.